

EXCITON HARVESTING SYSTEMS OF NANOCRYSTALS

A THESIS

SUBMITTED TO THE DEPARTMENT OF PHYSICS
AND THE GRADUATE SCHOOL OF ENGINEERING AND SCIENCE
OF BILKENT UNIVERSITY
IN PARTIAL FULFILMENT OF THE REQUIREMENTS
FOR THE DEGREE OF
DOCTOR OF PHILOSOPHY

By

Evren Mutlugün

December 2011

I certify that I have read this thesis and that in my opinion it is fully adequate, in scope and in quality, as a thesis for the degree of Doctor of Philosophy.

Assoc. Prof. Dr. Hilmi Volkan Demir (Supervisor)

I certify that I have read this thesis and that in my opinion it is fully adequate, in scope and in quality, as a thesis for the degree of Doctor of Philosophy.

Prof. Dr. Bilal Tanatar

I certify that I have read this thesis and that in my opinion it is fully adequate, in scope and in quality, as a thesis for the degree of Doctor of Philosophy.

Assoc. Prof. Dr. Ceyhun Bulutay

I certify that I have read this thesis and that in my opinion it is fully adequate, in scope and in quality, as a thesis for the degree of Doctor of Philosophy.

Prof. Dr. Ayhan Altıntaş

I certify that I have read this thesis and that in my opinion it is fully adequate, in scope and in quality, as a thesis for the degree of Doctor of Philosophy.

Prof. Dr. Raşit Turan

Approved for the Graduate School of Engineering and Science:

Prof. Dr. Levent Onural

Director of Graduate School of Engineering and Science

ABSTRACT

EXCITON HARVESTING SYSTEMS OF
NANOCRYSTALS

Evren Mutlugün
Ph.D. in Physics

Supervisor: Assoc. Prof. Dr. Hilmi Volkan Demir
December 2011

Semiconductor nanocrystals, also known as colloidal quantum dots, have gained substantial scientific interest for innovative light harvesting applications including those in biolabeling. Organic dyes and fluorescent proteins are widely used in biotargeting and live cell imaging, but their intrinsic optical properties, such as narrow excitation windows, limit their potential for advanced applications, e.g., spectral multiplexing. Compared to these organic fluorophores, favorable properties of the quantum dots including high photoluminescence quantum yields together with tunable emission peaks and narrow spectral emission widths, high extinction coefficients, and broad absorption bands enable us to discover and innovate light harvesting composites. In such systems, however, the scientific challenge is to achieve high levels of energy transfer from one species to the other, with additional features of versatility and tunability.

To address these problems, as a conceptual advancement, this thesis proposes and demonstrates a new class of versatile light harvesting systems of semiconductor nanocrystals mediated by excitonic interactions based on Förster-type nonradiative energy transfer. In this thesis, we synthesized near-unity efficiency colloidal quantum dots with as-synthesized photoluminescence quantum yields of >95%. As proof-of-concept demonstrations, we studied and achieved highly efficient exciton harvesting systems of quantum dots bound to fluorescent proteins, where the excitons are zipped from the dots to the proteins in the composite. This led to many folds of light harvesting (tunable up to 15

times) in the case of the green fluorescent protein. Using organic dye molecules electrostatically interacting with quantum dots, we showed high levels of exciton migration from the dots to the molecules (up to 94%). Furthermore, we demonstrated stand-alone, flexible membranes of nanocrystals in unprecedentedly large areas ($> 50 \text{ cm} \times 50 \text{ cm}$), which paves the way for high-end, large-scale applications. In the thesis, we also developed exciton-exciton coupling models to support the experimental results. This thesis opens up new possibilities for exciton-harvesting in biolabeling and optoelectronics.

Keywords: Semiconductor nanocrystals, nonradiative energy transfer, excitons, light harvesting.

ÖZET

NANOKRİSTALLİ EKSİTON HASATI SİSTEMLERİ

Evren Mutlugün
Fizik Bölümü Doktora
Tez Yöneticisi: Doç. Dr. Hilmi Volkan Demir
Aralık 2011

Kolloidal kuantum noktacıkları olarak da bilinen yarı iletken nanokristaller, biyo-etiketlemenin de içerisinde olduğu yenilikçi ışık hasatı sistemleri için oldukça büyük bilimsel ilgi kazanmıştır. Organik boyalar ve floresan proteinler, biyo-hedef ve canlı hücre görüntüleme için sıklıkla kullanılsa da, sahip oldukları esas optik özellikleri, dar uyarım penceresi gibi, onların ileri uygulamalar için kullanımlarını, örn. spektral çoklama, sınırlamaktadır. Organik ışıyıcılarla karşılaştırıldığında kuantum noktacıklarının sahip olduğu yüksek fotolüminesans verimliliği, ayarlanabilir ışınım dalga boyları, dar ışınım tayfları, yüksek soğurma katsayıları ve geniş soğurma tayfları gibi üstün özellikleri yenilikçi ışık hasatı kompozitlerini keşfetmemizi sağlamaktadır. Bu sistemlerde ise bilimsel zorluk, bir türden diğerine, ayarlanabilir ve farklı şekillerde uygulanabilir özellikleriyle yüksek verimli enerji transferi elde etmektir.

Bu tez, bu sorunları karşılamak için kavramsal bir ilerleme olarak, Förster tipi ışınımsal olmayan enerji transferi temelli eksitonik etkileşime dayanan, yeni sınıf farklı şekillerde uygulanabilir yarı iletken nanokristalli ışık hasatı sistemlerini önerip göstermektedir. Bu tezde biz, sentezlendiği hali ile fotolüminesans kuantum verimlilikleri %95'ten daha yüksek kolloidal kuantum noktacıklarını verimlilikleri tama yakın şekilde sentezledik. Kavramsal ispat olarak, kompozit yapı içerisinde eksitonların kuantum noktacıklardan flöresan proteinlere gönderildiği, yüksek verimlilikte eksiton hasatı elde ettiğimiz proteinlere bağlı noktacıkları sistemlerini çalışıp elde ettik. Bu çalışmalar yeşil flöresan protein için çok yüksek kat (15 kata kadar ayarlanabilir) ışık hasatını sağlamıştır. Organik boya moleküllerini kuantum noktacıkları ile elektrostatik olarak etkileştirerek, noktacıklardan moleküllere yüksek verimlilikle (%94'e kadar) eksiton transferini gerçekleştirdik. Bununla birlikte üst düzey büyük

alanlı uygulamalara yol açan, daha önce hiç benzeri görülmemiş, büyük alanlı (50 cm × 50 cm'den büyük), tek başına ayakta durabilen, esnek nanokristal membranlarını gösterdik. Bu tezde ayrıca deneysel sonuçlarımızı desteklemesi için eksiton-eksiton çiftlemesi esasına dayanan modelleme yaptık. Bu tez biyoeiktleme ve optoelektronikte eksiton hasatı için yeni olasılıklar açmaktadır.

Anahtar kelimeler: Yarı iletken nanokristaller, ışınımsal olmayan enerji transferi, eksitonlar, ışık hasatı.

Acknowledgements

It has been a long time since people started contributing this PhD thesis in different aspects. It is not easy to possibly include all of them on this page, but I will try my best...

First I would like to acknowledge my advisor Assoc. Prof. Hilmi Volkan Demir. He had been more than a Ph.D. advisor to me. I had the opportunity to share almost 7 years of professional experience with him. Not only learning from him about scientific content, but I had the chance of getting more than one could get from his advisor. Apart from all, he taught me to be professional in a scientific environment. I will never forget his kind attitude, friendship, guidance, encouragement, and his optimistic way of handling things. I am thankful to him to provide me and my colleagues with a truly scientific environment by all means.

Also my special thanks go to Prof. Bilal Tanatar, Assoc. Prof. Ceyhun Bulutay, Prof. Raşit Turan, and Prof. Ayhan Altıntaş for being on my jury and for their kind support and help throughout my Ph.D. at Bilkent.

Now comes my friends. Without your friendship and support, this thesis would not have been possible. Whatever I write here for your friendship and personality, that would not really be enough. I learned a lot from you and I am really proud to have such a selection of very nice people to be my best friends. I would like to acknowledge my closest friends Sedat Nizamoğlu, Rohat Melik, Tuncay Özel, Özge Özel, and Emre Sarı, my officemates at the Advanced Research Lab. I cannot forget the happy times we had there. I would also very much like to acknowledge Talha Erdem, Burak Güzeltürk, İbrahim Murat Soğancı, Can Uran, Cüneyt Eroğlu, Yusuf Keleştemur, Kıvanç Güngör, Ahmet Fatih Cihan, Shahab Akhavan, Yasemin Coşkun, Sayım Gökyar, Veli Tayfun

Kılıç, Aydan Yeltik, Ozan Yerli, and Togay Amirahmadov for their wonderful friendship and collaboration.

Also very importantly, among the management and technical team and the post doctoral researchers of the group: Dr. Nihan Kosku Perkgoz, Ozgun Akyuz, and Emre Unal; and Dr. Urartu Özgür Şafak Şeker, Dr. Ludwig Pedro Hernandez Martinez, and Dr. Vijay Kumar Sharma. I am really very thankful to you all for great friendship and support to help me carry out my Ph.D. work.

To the present and former members of the Devices and Sensors Demir Group: I am thankful to you all!

Also, I am thankful to Prof. Salim Çıracı, faculty members, graduate students and the technical support staff at UNAM for their kind attitude, support and help to carry out my experimental Ph.D. work. Also, I would like to acknowledge Physics Department and Advanced Research Lab faculty, graduate students, and staff for their support and friendship.

I am thankful to Assoc. Prof. Mehmet Şahin, and Dr. Murat Taş for their support and friendship. I would like to further acknowledge our collaborators in Germany. I am thankful to Prof. Alexander Eychmuller, Dr. Nikolai Gaponik, Dr. Stephen Hickey, Dr. Vladimir Lesnyak, Dr. Subhendu Panda, Dr. Zoran Popovic and the entire group there.

Besides, I would like to acknowledge TÜBİTAK BİDEB 2211 PhD. Scholarship.

My special thanks is for my family. I am sure they are the ones whom deserve the most of my acknowledgement. I am thankful for their support in all means. My family and my family-in-law, I love you all. My wife Sumeyye. I would not have been able to get to this stage without you being in my life. You have been

more than everything for me. And my son, Yusuf Kerem. You were the one to show me how fruitful the life is. I love you so much. I dedicate this thesis to my wife and my son.

Table of Contents

1. INTRODUCTION	1
2. SEMICONDUCTOR NANOCRYSTALS	9
2.1 BACKGROUND INFORMATION	9
2.2 SYNTHESIS OF II-VI QDs	15
2.2.1 <i>Synthesis of core QDs</i>	15
2.2.1.1 Aqueous CdTe QD synthesis.....	15
2.2.1.2 Organic CdSe QD synthesis	18
2.2.2 <i>Synthesis of core/shell QDs</i>	20
2.2.2.1 CdSe/CdS core/shell QDs	21
2.3 SYNTHESIS OF III-V QD SYNTHESIS	24
2.3.1 <i>InP/ZnS QD synthesis</i>	24
3. NONRADIATIVE ENERGY TRANSFER	28
3.1 EXCITATION AND DE-EXCITATION PATHS	28
3.2 FÖRSTER TYPE NONRADIATIVE ENERGY TRANSFER MECHANISM.....	29
4. EXPERIMENTAL METHODS	33
4.1 PHOTOLUMINESCENCE SPECTROSCOPY AND PHOTOLUMINESCENCE EXCITATION SPECTROSCOPY	33
4.2 ABSORPTION SPECTROSCOPY	34
4.3 QUANTUM EFFICIENCY MEASUREMENT	34
4.4 TIME RESOLVED PHOTOLUMINESCENCE SPECTROSCOPY	36
4.5 TRANSMISSION ELECTRON MICROSCOPY	37
4.6 OTHERS	37
5. EXCITON HARVESTING OF NANOCRYSTAL QUANTUM DOTS FOR GREEN FLUORESCENT PROTEINS	40
5.1 INTRODUCTION	40
5.2 RESULTS AND DISCUSSION	41
5.3 SUMMARY	60
6. EXCITONIC ENERGY TRANSFER FROM CHARGED QUANTUM DOTS TO ORGANIC DYE MOLECULES	61
6.1 INTRODUCTION	61
6.2 RESULTS AND DISCUSSION.....	63
6.3 SUMMARY	70
7. EXCITONIC ENERGY TRANSFER FROM WATER SOLUBLE QUANTUM DOTS TO ORGANIC DYE MOLECULES	71
7.1 INTRODUCTION	71
7.2 RESULTS AND DISCUSSION.....	74
7.3 SUMMARY	90
8. EXCITONIC INTERACTIONS IN VERY LARGE-AREA FREE-STANDING MEMBRANES OF COLLOIDAL InP/ZnS QUANTUM DOTS	91
8.1 INTRODUCTION	91
8.2 RESULTS AND DISCUSSION.....	94
8.3 SUMMARY	116

9. CONCLUSIONS.....	117
APPENDIX.....	144
Derivation of FRET based dipole-dipole interaction.....	144

List of Figures

Figure 2.1.1 E-k diagram for bulk semiconductor crystal and semiconductor nanocrystal.	10
Figure 2.1.2 Synthesis set-up in fumehood together (with an inset of the synthesis reaction flask (top right) at the Demir Lab.	12
Figure 2.1.3 Glove box (nitrogen filled), used for storage and preparation of the chemicals used in the synthesis at the Demir Lab.	13
Figure 2.1.4 Absorption spectra of different sized CdTe QDs at room temperature.	14
Figure 2.1.5 Normalized photoluminescence spectra of different sized CdTe QDs at room temperature.	14
Figure 2.2.1.1.1 Absorption spectra of aqueous CdTe QDs at room temperature with the alequots taken during the growth of these QDs.	16
Figure 2.2.1.1.2 Normalized photoluminescence (PL) spectra of the as-synthesized aqueous CdTe QDs at room temperature.	17
Figure 2.2.1.1.3 Quantum yields of different sized CdTe QDs at room temperature.	17
Figure 2.2.1.2.1 Photoluminescence and absorption of organic CdSe QDs at room temperature (Reproduced with permission after [77].)	19
Figure 2.2.1.2.2 TEM image of organic CdSe QDs. The scale bar is 5 nm.	20
Figure 2.2.2.1.1 High resolution TEM image of the CdSe/CdS QDs. The scale bar is 5 nm.	22
Figure 2.2.2.1.2 Emission and absorption spectra of the core CdSe and core/shell CdSe/CdS QDs at room temperature with an increasing number of shell monolayers (ML). The quantum efficiency values are given on each individual graph.	23
Figure 2.2.2.1.3 Picture of our highly efficient CdSe/CdS QDs under UV light.	23

Figure 2.3.1.1 Absorption profile of one pot synthesis of InP/ZnS core/shell QDs at room temperature along with a picture of the dots under UV-illumination.	25
Figure 2.3.1.2 Emission profile of one pot synthesis of InP/ZnS core /shell QDs at room temperature.....	25
Figure 2.3.1.3 Absorption spectra of two step synthesis of InP/ZnS core/shell QDs at room temperature, along with a picture of the dots under UV illumination.	27
Figure 2.3.1.4 Emission spectra of two step synthesis of InP/ZnS core/shell QDs at room temperature.....	27
Figure 3.1.1 Diagram showing the possible excitation and de-excitation paths within quantum dot pairs.	29
Figure 3.2.1 Fluo Time 200 Time Resolved Spectroscopy set-up at the Demir Lab.	31
Figure 3.2.2 Dependence of the FRET efficiency on r/R_0	32
Figure 4.3.1 Emission and absorption spectra of the Rhodamine 6G used for the quantum efficiency measurements and the QDs. Black arrow represents the intersection point of the absorption spectra for both species, which is used as the excitation wavelength.	35
Figure 5.2.1 Donor ZnCdSe QDs emission and acceptor GFP absorption spectra at room temperature.....	41
Figure 5.2.2 High resolution TEM image of the ZnCdSe QDs.....	42
Figure 5.2.3 Adsorption isotherms of GFP on QD modified surface of QCM sensor.....	44
Figure 5.2.4 Single Langmuir adsorption model fit to the adsorption data of his-tagged GFP on surface bound QD. The red line represents the fit as the black dots denote the data points.....	45
Figure 5.2.5 Mass change monitored in TGA and the derivative of mass change as a function of temperature for the nanocomposite.	46
Figure 5.2.6 Comparison of the temperature derivative mass change data for QD and QD-GFP composite material. The shift in QD peaks and emergence of	

new peaks suggest the formation of new composite material.....	47
Figure 5.2.7 PLE intensity ratio of the bare QDs at its emission wavelength of 422 nm compared to the bare GFP at its emission wavelength of 508 nm at room temperature. The insets show the individual PLE intensities of the GFP and the QD alone.....	48
Figure 5.2.8 Change in photoluminescence of the donor-acceptor QD-GFP system with changing A/D concentration ratio (excitation at 315 nm) at room temperature	49
Figure 5.2.9 Control experiments for the photoluminescence of acceptor GFP only with the same acceptor concentration, corresponding to the A/D concentration ratio (excitation at 315 nm) at room temperature	49
Figure 5.2.10 Enhancement of the GFP photoluminescence using QDs when excited with 315 nm monochromatic light at room temperature	50
Figure 5.2.11 Time resolved photoluminescence decays of the donor changing with A/D at room temperature	51
Figure 5.2.12 Donor lifetimes, extracted from time resolved photoluminescence decays, and theoretically predicted, as a function of A/D at room temperature	52
Figure 5.2.13 Time resolved photoluminescence decays of the acceptor changing with A/D at room temperature	53
Figure 5.2.14 Acceptor lifetimes, extracted from time resolved photoluminescence decays, as a function of A/D at room temperature	53
Figure 5.2.15 Theoretical and experimental FRET efficiencies extracted from lifetime measurements at room temperature	54
Figure 5.2.16 Schematic representation for the energy transfer from QD to GFP (no drawn to scale). Picture shows a QD surrounded by a GFP molecule. “d” represents the average separation distance between the QD and the GFP over which energy transfer takes place. Inset: Dimensions for the GFP molecule	56

Figure 5.2.17 Room temperature photoluminescence decays of the GFP only, GFP after FRET, and GFP after FRET with controlled enzyme (activated) addition.....	58
Figure 5.2.18 Lifetime modifications of the GFP only, GFP after FRET, and GFP after FRET with enzyme (activated) addition.....	58
Figure 5.2.19 Lifetime modifications of the GFP only, GFP after FRET, and GFP after FRET with enzyme (unactivated) addition.....	59
Figure 5.2.20 Room temperature photoluminescence decays of the GFP only, GFP after FRET, and GFP after FRET with enzyme (unactivated) addition.	59
Figure 6.2.1 Room-temperature time-resolved photoluminescence (TRPL) of amine-functionalized CdSe/ZnS nanocrystal donors (AF/NC-Ds) together with RhB acceptors (RhB-As) (a) at the donor emission wavelength (at 541 nm) and (b) TRPL of non-functionalized CdSe/ZnS nanocrystal donors (NF/NC-Ds) together with RhB acceptors (RhB-As) at 541 nm. Room-temperature steady-state photoluminescence (SSPL) of (c) AF/NC-Ds + RhB-As and (d) NF/NC-Ds + RhB-As. All of the TRPL and SSPL measurements are presented as parameterized with respect to the varied concentration ratios of A/D. (e) FRET efficiency levels (extracted from TRPL) and (f) enhancement factor of acceptor emission with respect to the case of acceptors alone (with no donors), both as a function of A/D ratios.	66
Figure 7.2.2 Room temperature absorbance spectra of the two differently sized aqueous CdTe nanocrystal QDs (emitting at 552 and 525 nm) together with that of the Rhodamine B dye molecules. (b) Normalized room temperature photoluminescence spectra of our aqueous CdTe QDs (donors) selectively chosen to emit at the peak wavelengths of 525 and 552 nm, along with the emission and absorption spectra of the Rhodamine B molecules (acceptors). The donors emitting at 552 nm provide a better spectral match to the electronic structure of these acceptors.....	75
Figure 7.2.3 SSPL spectra taken at room temperature by adding controlled amounts of dye acceptors into the aqueous donor solution using CdTe QDs emitting at the peak wavelength of (a) 552 nm and (b) 525 nm. The legends show the corresponding A/D concentration ratios (A/D=1.8–152.8). (Note that these PL intensity levels are measured using the same arbitrary units and that they are presented using the scales as indicated on their plots, for clear visibility.).....	78
Figure 7.2.4 TRPL measurements of donor molecules taken at room temperature by adding controlled amounts of dye acceptors into the aqueous donor	

solution, using CdTe QDs emitting at the peak wavelength of (a) 552 nm and (b) 525 nm, all shown together with their corresponding numerical fits, and along with a comparative analysis of the donor photoluminescence decay lifetimes both for 552 and 525 nm emitting dots as a function of A/D concentration ratio (c). In the last plot, the red (black) dotted baseline represents the lifetime of only donors of 552 nm (525 nm) emitting dots, without any acceptors in the mixture..... 80

Figure 7.2.5 TRPL measurements of acceptor molecules at room temperature while varying the A/D concentration ratio, shown along with their numerical fits using (a) 552 nm and (b) 525 nm emitting QDs and comparative analysis of the acceptor photoluminescence decay lifetimes for emission (c) at 581 nm (acceptor peak with a weak donor tail) and (d) at 605 nm (strong acceptor tail with no donor tail) as a function of A/D concentration ratios. In both plots (c) and (d), the dashed baseline represents the lifetime of only acceptors without any donors..... 83

Figure 7.2.6 Comparison of (a) FRET efficiencies and (b) enhancement of the acceptor emission at room temperature, using 552 nm and 525 nm emitting CdTe QD donors, as a function of the A/D concentration ratio..... 89

Figure 8.2.1. Chemical structure of the myristic acid (left) and PMMA (right). 94

Figure 8.2.2 Contact-angle measurement of the free standing InP/ZnS film showing the hydrophobic property with contact angles of $\sim 89^\circ$ (for left and right). 95

Figure 8.2.3 Photograph of the 50 cm \times 50 cm PMMA-InP/ZnS QD membrane under room light (left) and UV illumination (right). 95

Figure 8.2.4 XPS spectra of InP/ZnS QD only, PMMA only, and the composite membrane for elemental carbon analysis..... 97

Figure 8.2.5 XPS spectra of the InP/ZnS QD-PMMA membrane..... 99

Figure 8.2.6 Stress-strain measurement of a 35 μm thick InP/ZnS QD-PMMA film..... 100

Figure 8.2.7 Normalized room temperature photoluminescence (solid line) and absorption (dashed line) spectra of the donor and acceptor InP/ZnS QDs. Transmission electron microscopy (TEM) image of the donor/acceptor QDs (inset). 101

Figure 8.2.8 Time resolved photoluminescence (TRPL) spectra of the donor QD without the acceptor (top) and the donor QD with the acceptor (bottom), measured at the donor emission wavelength of 490 nm, as a function of

decreasing sample temperature (inset). The exponential fits of the observed decays for the donor (with and without acceptor) are also given.....	102
Figure 8.2.9 Temperature dependent photoluminescence intensity of the donor (top) and acceptor (bottom) QDs, extracted from the time-resolved photoluminescence measurement. The photoluminescence intensity is extracted from the set-up using the same time interval for the photon counts.....	104
Figure 8.2.10 Theoretical (red circles) and experimental (black squares) FRET efficiencies as a function of temperature.	105
Figure 8.2.11 Donor energy transfer rate calculated using the experimentally measured lifetime values as a function of temperature.	105
Figure 8.2.12 (A) TRPL spectra of the acceptor without the donor (at 590 nm); (inset) the acceptor lifetimes (with and without the donor). (B) TRPL of the acceptor with the donor (at 590 nm). (C) TRPL of the acceptor (without the donor) (at 640 nm, far from the donor emission tail), (inset) the acceptor lifetimes (with and without the donor). (D) TRPL of the acceptor (with the donor) (at 640 nm). All curves and data are given parametrized with respect to or as a function of the temperature and the lifetimes are fit with triple exponentials.....	107
Figure 8.2.13 (a) Donor-Acceptor (D-A) schematic for a single donor (D) and acceptor (A). (b) Energy diagram for the D-A pair energy transfer process. Blue dashed lines represent the absorption process of the QD (donor/acceptor). Blue solid lines show fast relaxation process. Red dashed lines illustrate light emission process (relaxation from the lowest excited state to the ground state). Black solid lines represent the energy transfer from the donor to the acceptor. Horizontal black dashed line shows the Coulomb interaction between the donor and acceptor.	112
Figure 8.2.14 Steady-state room temperature photoluminescence spectra of the donor only, acceptor only and hybrid film. Steady-state room temperature photoluminescence spectra of the donor only, acceptor only and hybrid film of the same when the hybrid emission is fit to the donor and acceptor emissions as Gaussian curves (inset).....	114
Figure 8.2.15 Emission spectra of the color-conversion white LED (WLED) when the blue LED chip is hybridized with our bilayer InP/ZnS QDs. ...	115

List of Tables

Table 6.2.1 List of quantum yields, Förster radii, average decay lifetimes and their χ^2 error limits at the donor emission wavelength, and FRET efficiencies, all for different concentration ratios of A/D when using amine- and non-functionalized CdSe/ZnS nanocrystal donors.	67
Table 7.2.1 TRPL measurement analysis of the 525 nm emitting donors at 525 nm varying the A/D concentration ratio.	84
Table 7.2.2 TRPL measurement analysis of the 525 nm emitting donors at 581 nm varying the A/D concentration ratio.	84
Table 7.2.3 TRPL measurement analysis of the 525 nm emitting donors at 605 nm varying the A/D concentration ratio.	85
Table 7.2.4. TRPL measurement analysis of the 552 nm emitting donors at 552 nm varying the A/D concentration ratio.	85
Table 7.2.5 TRPL measurement analysis of the 552 nm emitting donors at 581 nm varying the A/D concentration ratio	86
Table 7.2.6 TRPL measurement analysis of the 552 nm emitting donors at 605 nm varying the A/D concentration ratio.	86
Table 7.2.7. TRPL measurement analysis of the 581 nm emitting acceptors at 581 and 605 nm varying the A/D concentration ratio.	87
Table 8.2.1 Experimental and theoretical changes in the lifetime of the acceptor alone and in the hybrid film with the donor.....	108
Table 8.2.2 Experimental and theoretical changes in the lifetime of the donor alone and in the hybrid film with the acceptor, along with the FRET efficiencies.	109

To my wife and son...

Chapter 1

Introduction

Efficient light harvesting for biolabeling has been one of the scientific challenges to date. The detection of molecules, tissue imaging, and cell tracking require better imaging, higher resolving power, and more efficient use of the incident light to overcome the existing limitations. The fluorophore organic dyes and fluorescent proteins are among the early examples of the fluorescent tags used widely in bio-related research for the detection of targeted cells and biolabeling [1,2,3].

The wide-scale use of the organic dyes and fluorescent proteins have opened many possibilities. Control of the chemical structure and modifications of the functional groups make these fluorophores good candidates for superior biolabeling and tagging systems because of their biocompatibility [4,5]. However, these fluorophores exhibit a characteristic optical absorption and emission spectra which cannot be tailored easily. The organic dyes and fluorescent proteins possess narrow absorption windows and they cannot be excited beyond their characteristic spectral excitation ranges. Also, their absorption and emission spectra overlap significantly. As a result, the absorption suppresses the emission, limiting their performances and the possible use for high-end applications [6,7,8].

Starting in 80s, there was a breakthrough in the science of colloidal particles with the invention of nanocrystal quantum dots (QDs) [9], the tiny bulbs which are superior to the existing fluorophores, since they have size dependent emission characteristics, an order of magnitude higher extinction coefficients

and brightness, and broader excitation windows, as compared to the other members of the fluorophores [10,11]. With the introduction of this new member to the fluorophores family, the QDs have gained substantial interest in the last few decades for many prospective applications, i.e., from solar cells and light emitting diodes [12,13], to in-vivo bio-imaging and photodynamic therapy applications [14,15]. Beginning with 90s, the method of hot injecting precursors during colloidal QD synthesis [16,17] allowed for highly monodisperse and high quantum yield particles. Owing to their outstanding optical characteristics, the nanocrystal QDs have been considered as an alternative to overcome the dominant use of organic dyes and fluorescent proteins.

From the applications point of view, because of their size tunable superior properties, semiconductor nanocrystals have been used in optoelectronics and biorelated applications. Solar cells, detectors, and light emitting diodes are among the well known examples for the use of the QDs in optoelectronics. In solar cells, QDs have opened the new path for the 3rd generation solar cells. QDs offer the potential to overcome the thermodynamic limiting efficiency of the solar cells with multi-exciton generation [18].

In their work Huynh et. al. demonstrated the solar cells composed of CdSe nanorods in P3HT polymer blends with external quantum efficiencies of 59% [19]. In their work, Luther et al., demonstrated the solar cells using PbSe QDs with overall efficiency of 2.1% under AM 1.5G solar radiation, reaching external quantum efficiency levels of 55-65% in the visible [20]. Recently, the Sargent Group have demonstrated colloidal QD solar cells using PbS nanocrystals together with TiO₂ nanoparticles doped by Zr, with 5.6% efficiency, improving the charge separation [21]. In QD sensitized solar cells, QDs come into play as the sensitizers instead of the dyes used in dye sensitized solar cells. They are expected to boost the Si solar cells at reduced costs. Lee et al. demonstrated the use of CdSe QDs with efficiencies larger than 1% when used with TiO₂ [22]. Using the wider gap ZnS overcoating CdSe cores, Toyoda

et al. demonstrated efficiency levels of >2% [23]. Recently, Zhang et al. studied the structural properties of the photoelectrode and reported the highest QD sensitized solar cell efficiency of 4.79% [24].

The first reports demonstrating LEDs made from colloidal QDs had relatively poor efficiencies [25,26]. In 2002, electroluminescence has been shown in monolayers of the core/shell QDs sandwiched between the electron and hole transport layers by Coe et al. [27]. This study is one of the first reports to open the way for the QD-LED research later followed by other reports aiming for higher performance [28,29]. Different than these previous reports that present such QD-LEDs, our group have demonstrated tunable photometric performance of white color-conversion LEDs, (WLED) based on the quantum dots used as luminophores [30]. Recently, research efforts using QDs within the display applications have emerged owing to the advances in the mature synthesis of these QDs together with their successful LED demonstrations [31,32].

In bioapplications, the use of QDs have evolved during the past few last years due to the need for a better imaging contrast, enabling long live cell imaging, stability and multicolor labeling. Due to the intrinsic drawbacks of using organic fluorophores, semiconductor nanocrystals have been an alternative in biorelated targeting, sensing, and imaging applications. As compared with the organic fluorophores, semiconductor nanocrystal QDs offer size dependent emission characteristics, narrow and symmetric emission spectra preventing crosstalk in multicolor labeling, higher quantum yield and broad absorption spectra, providing increased imaging frequency in multicolor labeling and one order of magnitude higher photostability, making them a good candidate for long term live cell imaging.

One of the major steps for the QDs to be used in biorelated applications is their biocompatibility. Since water is the natural media for the living things, the solubility of QDs is a crucial step for using them as an active component in

living organisms. The ligands attached to the QDs determine the solubility of the QDs in various media. Therefore, unless synthesized in water, the QDs need to be dissolved in water before being utilized in bioapplications. The solubility in water is achieved by ligand exchange [33]. By using the ligand exchange, the QDs are able to be dissolved in water but it comes at the cost of decreased quantum yields, which has been a major issue to address in the ligand chemistry for inorganic quantum dots. One of the other crucial factors is the functionalization of the QDs to provide the biocompatibility. Surface capping methods and functionalizations using different biofunctional mechanisms have been employed specific to various applications [34,35].

Due to the fact that the QDs have order an of magnitude higher lifetime than the organic dyes, they have been employed to reduce the naturally occurring autofluorescence of the cells, which is comparable with the lifetime of the organic dyes. This enables the enhancement of the image contrast by the use of the QDs [36]. The QDs broad absorption spectra makes multicolor labeling possible for in vivo applications, where different biomarkers are tagged by using different QDs [37,38]. Imaging by the use of the QDs have found a wide area of interest in the imaging of the cancer cells. For example, a polypeptide-quantum dot hybrid assembly have been utilized for the detection of cancer cells recently [39]. In another study, the detection of human prostate cancer using QDs encapsulated in a triblock polymer has been demonstrated by Nie Group [40].

Immunoglobulin G and streptavidin linked quantum dots have been used for labeling the breast cancer in the work of Wu et al. [41]. Besides, QDs have been employed as selective species to probe the targeted cells [42]. They have been utilized for live tracking the biomolecular transportation by Dahan et al. Not only for the biolabeling and cell imaging, QDs have been employed but also as drug delivery agents [43].

One of the key problems in the application of QDs in living cells is their possible toxicity. The toxicity of the QDs depends on many factors. The physical properties of the QDs as well as their surface functionalization play an important role for the mechanisms governing the toxicity. One of the major problems in the toxicity is the generation of the reactive oxygen species during the excitation of the QDs. Ipe et al. showed that the formation of the reactive oxygen species has been reduced by overcoating QDs with a shell material [44].

Apart from the systems of QD-bioconjugate complexes, the QDs have also been used together with organic dyes and fluorophores. This is because of the narrow emission bandwidth of the QDs, well separated from their absorption spectra. The nonradiative energy transfer mechanism employing both the QDs and the fluorophores has served as a nanoruler for the purpose of probing the changes in the conformational structure of the molecule. Using the energy transfer mechanism between the QDs and fluorophores, it is possible to track the molecular distance, which has been one of the major overarching goals of the QD-fluorophore systems [45]. Thus far, FRET has also been used as a powerful tool for the determination of the biomolecular activity and the determination of the intermolecular species within the molecules, as well as the conformational changes. The dipole-dipole interaction among the longer excitation lifetime donor and the shorter lifetime acceptor species facilitate the FRET mechanism, which has been further detailed in the coming chapters. Till date FRET has been used in various quantum dot-organic dye and fluorescent pairs for various goals, except for light harvesting, which is the topic of this thesis. Some of the previous examples will be outlined in here.

Medintz et al., discuss the design of biosensors for the detection of the maltose based on the FRET mechanism utilizing QDs [46]. In another study, the same group have employed the QDs as acceptor molecules together with the dye labeled proteins and reported that they have not observed FRET between these

pairs implying that the exciton lifetimes play a critical role in the FRET based systems [47].

Monitoring the hybridization of the QD-dye pairs by the FRET mechanism and labeling the functionalized DNA sequence have been studied by the Banin Group [48]. Within our group, the enzymatic control of the FRET among the bilayers of QD-peptide complexes have been demonstrated [49]. Samia et al. discussed the photodynamic therapy using the QDs triggering the photodynamic therapy agent facilitated by FRET [15]. The use of CdTe QDs for the detection of cancer markers with the FRET based biosensing mechanism has been demonstrated in the work of Liu et al. [50]. Another example application has been reported by the Nocera Group, demonstrating the energy transfer from CdSe/ZnS QDs to pH sensitive dye molecules as to be employed as a pH sensor [51]. The Mattoussi Group have employed the QDs together with dye molecules to study the FRET based multiplexing, namely using single excitation source to excite different molecules simultaneously [52]. The work of Bagalkot et al. is a good example of the FRET mediated cancer imaging and drug delivery systems [53]. QDs have been employed further as both donor and acceptor species in cascaded energy transfer studies for detection of bioactivity in the work of the Rogach Group [54]. Our group has also studied FRET among the bilayers of CdTe QDs for tuning the color chromacity [55]. In addition to all above, other examples of the QDs-organic dye FRET studies reported in the previous literature have been explained in relevance to the presented thesis work in the related chapters.

In the scope of this thesis work, different than the previous works of our group and the others, we propose and demonstrate a versatile, tunable class of light harvesting composites containing the QD-organic dye and QD-fluorescent protein complexes mediated by the nonradiative energy transfer to overcome the limitations of the organic dye molecules and fluorescent proteins. Here, the nonradiative energy transfer between the QD-organic dye pairs and QD-fluorescent proteins has been studied in detail. The light harvesting resulting

from the energy transfer, together with a detailed study of the time resolved kinetics, has been implemented for the first time. In addition, the large-area membranes of flexible, stand-alone QD-polymer composites have also been demonstrated. Following the Introduction in Chapter 1, the organization of the rest of this thesis is given as follows:

Chapter 2 presents the background information of the nanocrystals, their optical properties and the synthesis studies of different sized CdSe, CdSe/CdS, CdTe, and InP/ZnS QDs.

Chapter 3 is devoted to the discussion of the de-excitation paths of quantum dots including the energy diagram, and introduction of the Förster-type nonradiative energy transfer, along with the theoretical derivation showing the r^{-6} dependence of the energy transfer given in the Appendix.

Chapter 4 explains the experimental methods used in the context of the thesis.

Chapter 5 presents the demonstration of enhancement in the emission of the green fluorescent proteins attached to the QDs. The theoretical model of the resulting nonradiative energy transfer is also explained in the context of this chapter.

Chapter 6 demonstrates the use of positively charged CdSe/ZnS core/shell QDs for the energy transfer to organic dye molecules, emphasizing the charge effect to mediate the interaction among the particles with the highest reported FRET efficiency levels.

Chapter 7 describes the light harvesting of dye molecules mediated by FRET in solution by using different sized water based CdTe QDs.

Chapter 8 presents the energy transfer among different sized Cd-free QDs as well as the study of the temperature dependent emission kinetics. The demonstration of the large-area membranes of the QD-polymer composites and their use for white light generation with a performance level beyond the state-of-the-art is also included in this chapter.

Chapter 9 concludes this dissertation, summarizing the achievements of this thesis work along with a future outlook.

Chapter 2

Semiconductor Nanocrystals

2.1 Background information

Semiconductor nanocrystals, also known as the colloidal quantum dots (QDs), are particles consisting of 100-1000 atoms in the form of a crystal structure. The band gap engineering, made possible by choosing the right size of the nanocrystals, make them a great candidate for a wide range of possible applications. The three-dimensional quantum confinement results in the pronounced characteristics on these optical properties. Unlike the continuum energy states in bulk semiconductors, when the size of the crystal decreases, as in the case of nanocrystals, the energy levels start to get discrete. The phenomenon of strong quantum confinement arises, when the particle size is typically close to the exciton Bohr radius of the material. Depending on the size of the nanocrystal, greater or smaller than the exciton Bohr radius, the confinement of the nanocrystals is regarded as weak, intermediate or strong [56].

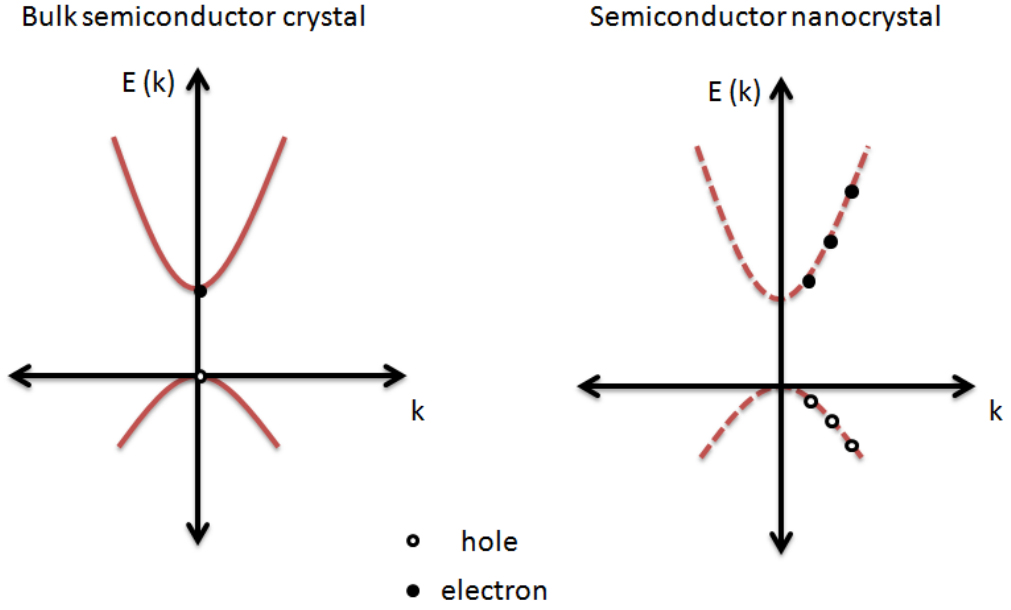


Figure 2.1.1 E-k diagram for bulk semiconductor crystal and semiconductor nanocrystal.

In a typical way, the incident photon with an energy greater than the band gap energy of the nanocrystals is absorbed. Subsequently, a bound electron and hole pair with Coulombic interaction, called exciton, is created. In order to fit their wavefunction in the finite size crystal, quantum confinement arises. In bulk semiconductors, since the size of the exciton is much smaller than the crystal size, and the charge carriers are free to move, i.e., not confined. The E-k diagram for bulk semiconductor crystal and semiconductor nanocrystals is given in Fig. 2.1.1. The band gap of a QD is given for the first excited electron state as,

$$E_{gap_{QD}} = E_{gap_{BULK}} + \frac{\hbar^2 \pi^2}{2m_e r^2} + \frac{\hbar^2 \pi^2}{2m_h r^2} - \frac{1.8e^2}{4\pi\epsilon\epsilon_0 r} + \text{terms (smaller)} \quad 2.1.1$$

where m_e and m_h are the effective masses of the electron and the hole, respectively, ϵ_0 is the permittivity of free space, ϵ is the relative permittivity, e is the electron charge, and r is the QD radius [57]. The second and third terms

in Eqn. 2.1.1 correspond to the energy of the first excited state, whereas the fourth term is due to the Coulombic interaction of the electron-hole pairs, and shadowed by the first terms in Eqn. 2.1.1, for the low-dimensional systems.

Using the quantum confinement, it is possible to engineer the emission and absorption characteristics of the QDs. Smaller sized dots have blue shifted emission and absorption profile as compared to the larger sized QDs, due to their effectively larger band gap, as clearly observed from Eqn. 2.1.1. The chemical composition and the stoichiometric ratio between the elements also determine the emission wavelength of the resulting nanocrystal synthesized. Designing the nanomaterial of interest is possible, thanks to the ongoing research efforts on the synthesis of the colloidal QDs.

Till date, many different kinds of quantum dots have been studied for their synthesis and applications. The particles of interest are mainly the II-VI, III-V and IV-VI group elements. In accordance with the range of their emission wavelengths, CdSe, CdTe, and CdS are among the mature examples of the II-VI group [58,59,60,61], together with III-V type InP based dots, emitting in the visible range [62,63], III-V ZnSe and ZnS structures govern the UV range, [64,65], whereas IV-VI group PbSe and PbS emit in the n-IR and IR emission range [66,67].

Besides core nanocrystals, there are also core/shell type QDs, which typically consist of a wider band gap material surrounding the core nanocrystal (e.g., type 1 core/shell QDs). The wider band gap shell serves as a potential barrier for the confinement of the wavefunction into the core. Few examples are CdSe/CdS, CdSe/ZnS, and InP/ZnS where the shell material is overcoated on the core to provide stability and enhanced emission [68,69,70].

One of the key factors in the QD synthesis is the ligands and the surfactants associated with the QDs. The ligands surrounding the nanocrystals provide

stability, make the QDs soluble in the appropriate environment and prevent them from agglomeration [71]. In the case of chemical interactions to make a composite structure with a QD; the ligand chemistry is an important area for bridging the QD to the desired part of the integrated species, e.g., a protein, and DNA. [72] Using the appropriate precursors for the synthesis, the ligand, and the solvent, the synthesis is carried out by controlled heating under inert atmosphere within the fumehood (see Fig. 2.1.2).

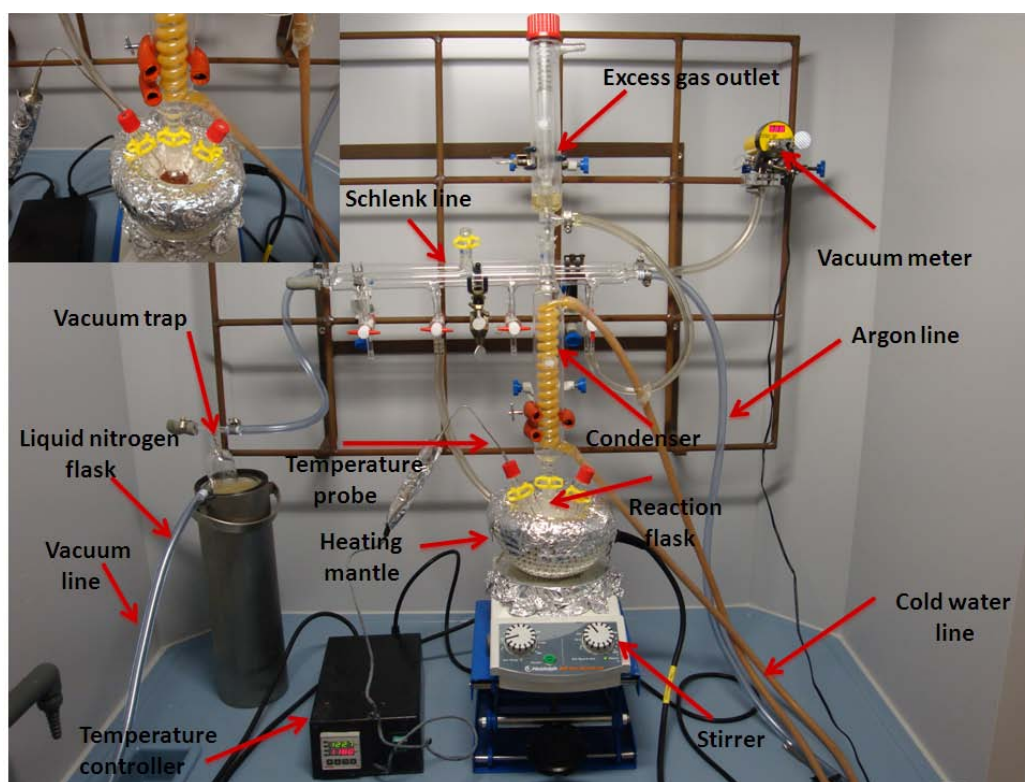


Figure 2.1.2 Synthesis set-up in fumehood together (with an inset of the synthesis reaction flask (top right) at the Demir Lab.



Figure 2.1.3 Glove box (nitrogen filled), used for storage and preparation of the chemicals used in the synthesis at the Demir Lab.

As mentioned previously, the optical properties of QDs are engineered by changing the size of the particles. The absorption features of QDs are given below (Fig. 2.1.4) for a series of different sized dots. Their optical absorption increases through the UV portion of the spectra. The peak in the absorption spectra is called the first excitonic peak, and depending on the characteristics of the QD, there may be other pronounced peaks as well, corresponding to higher photon energies.

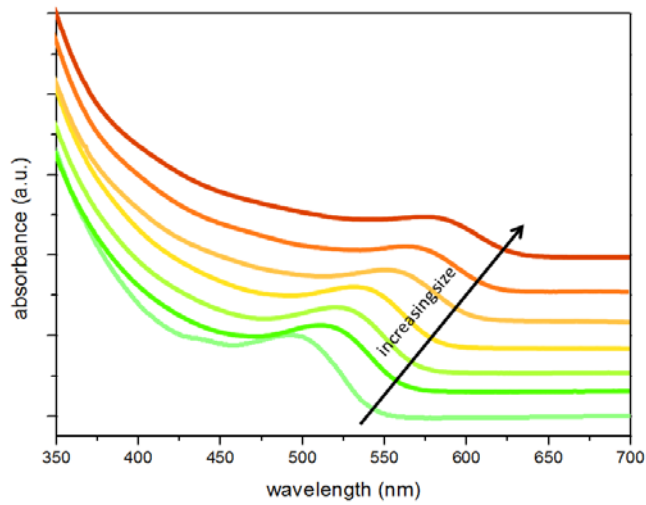


Figure 2.1.4 Absorption spectra of different sized CdTe QDs at room temperature.

The emission spectra, however, is narrow and Gaussian like (see Fig. 2.1.5), separated from the absorption peak by Stokes shift. The full width at half maximum (FWHM) value of the QD emission is typically determined by the monodispersity of the QDs in the inhomogeneous broadening regime, used as a figure of merit for their optical performance.

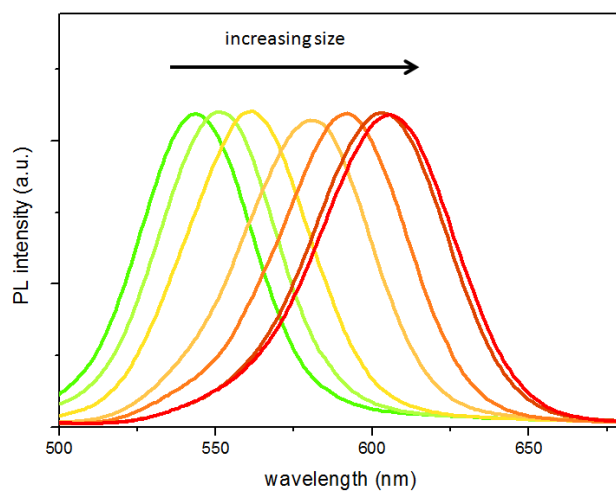


Figure 2.1.5 Normalized photoluminescence spectra of different sized CdTe QDs at room temperature.

2.2 Synthesis of II-VI QDs

The nanocrystals undergo various stages during the growth. These are the nucleation, growth, and isolation of the particles of proper size. In order to have monodisperse particles, which have a small size variation, the nucleation and the growth stages should be carried out at different temperatures, in the case of the hot injection method, or should be heated for long times at the same temperature [73]. The methods introduced here are used during the synthesis of the QDs employed in this thesis work. The materials of interest for the synthesis of the II-VI QDs are the aqueous CdTe, organic CdSe, and core/shell structured CdSe/CdS QDs.

2.2.1 Synthesis of core QDs

2.2.1.1 Aqueous CdTe QD synthesis

In the synthesis of aqueous CdTe QDs, cadmium per chlorate hexahydrate ($\text{Cd}(\text{ClO}_4)_2 \times 6\text{H}_2\text{O}$), thioglycolic acid (TGA), aluminum telluride (Al_2Te_3), sulfuric acid (H_2SO_4), and sodium chloride (NaCl) are obtained from vendors and directly used without further purification. Our synthesis procedure follows the method previously described in the literature [74,75]. In our synthesis, 4.59 g of $\text{Cd}(\text{ClO}_4)_2 \times 6\text{H}_2\text{O}$ is dissolved in 0.5 L of Milli-Q water in three-neck reaction flask. 1.33 g of TGA is added to the mixture, which turns into milky appearance. The pH of this mixture is then increased to 11.8 – 12.0 by dropwise addition of NaOH upon vigorous stirring. After this step, the reaction mixture becomes clear or slightly turbid. To prepare tellurium precursor, 0.8 g of Al_2Te_3 is transferred into a small three-neck flask in the glove box and then deaerated by passing Argon (Ar) for 50-60 min in the setup. 10 mL of deaerated 0.5 M H_2SO_4 is slowly poured into Al_2Te_3 lumps to produce H_2Te gas, which is carried

out by a slow Ar flow and bubbled through the mixture containing cadmium precursor for 40-50 min. The resulting red-black mixture is refluxed at 100 °C to obtain the desired nanocrystal size. The reaction mixture is then cooled to room temperature and filtered. The CdTe QDs are finally separated by size selective precipitation. The size selective precipitation is a post synthesis treatment and allows for separation of similar sized QDs in the same batch, thus providing better monodispersity after the synthesis. We use the CdTe QDs emitting in visible. The n-IR emitting CdTe is also possible by using mercaptopropionic acid (MPA) instead of TGA [76].

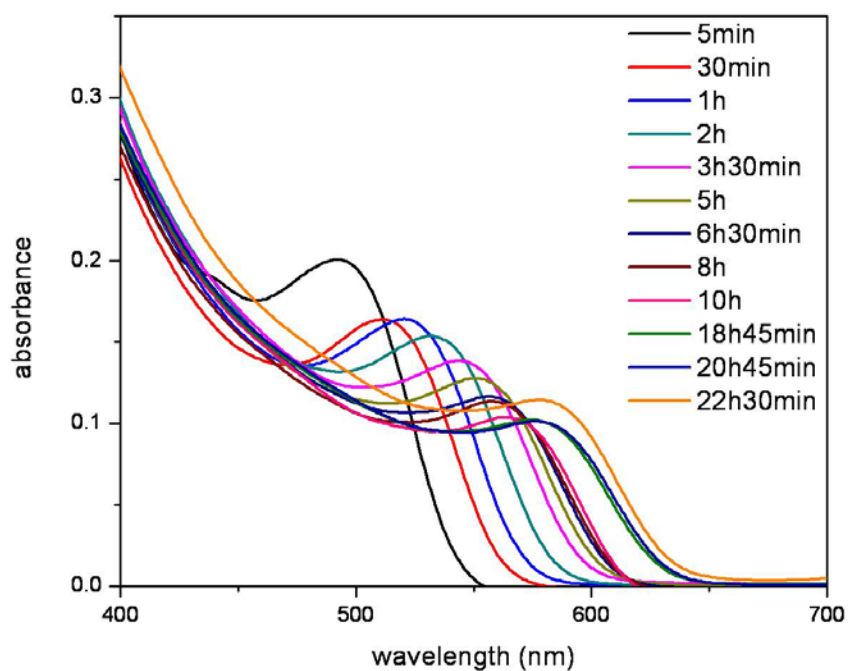


Figure 2.2.1.1.1 Absorption spectra of aqueous CdTe QDs at room temperature with the aliquots taken during the growth of these QDs.

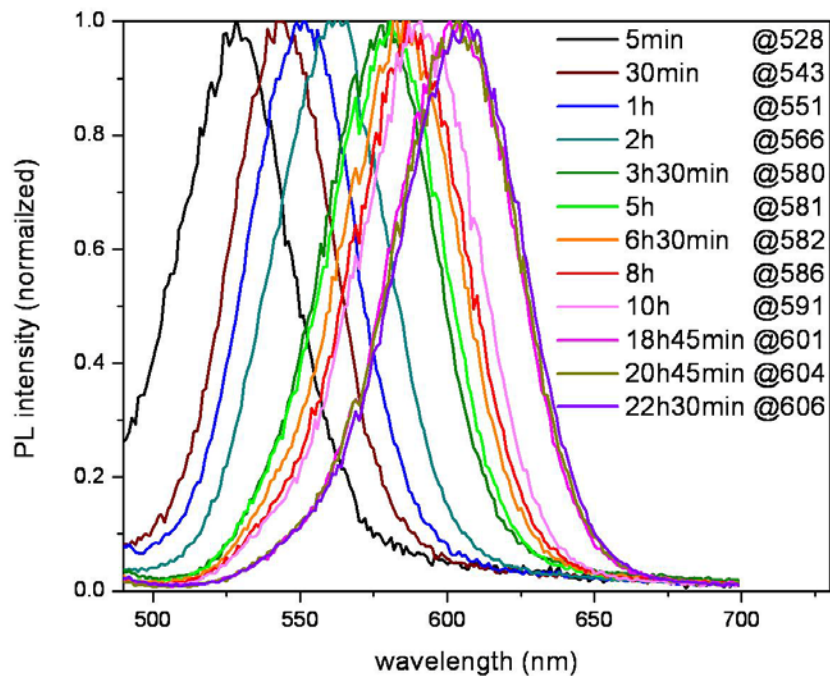


Figure 2.2.1.1.2 Normalized photoluminescence (PL) spectra of the as-synthesized aqueous CdTe QDs at room temperature.

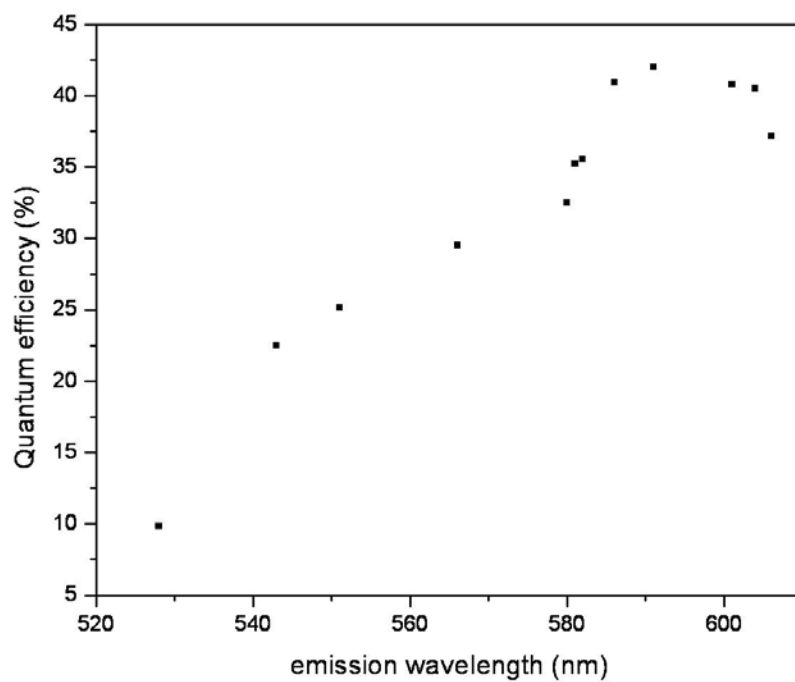


Figure 2.2.1.1.3 Quantum yields of different sized CdTe QDs at room temperature.

As shown in Fig. 2.2.1.1.1 and 2.2.1.1.2, the CdTe QDs grow in size with increasing the time associated with the synthesis. The possible emission peak wavelength achievable with the recipe followed runs around from 525 to 610 nm maximum using the thioglycolic acid as the surfactant. The trend of the quantum yield is increasing when the particles grow bigger in size up to a certain point, showing the increase in the stability of the particles (see Fig. 2.2.1.1.3). However, the quantum yield starts decreasing after long time exposure to heating due to the internal growth dynamics within the reaction flask. The resulting QDs have years long shelf life when stored in cold and dark conditions.

2.2.1.2 Organic CdSe QD synthesis

In a typical synthesis of CdSe nanocrystals, Cadmium Oxide, CdO (Acros Org.), Oleic Acid, OA (JT Baker) 1-Octadecene, ODE (Acros Org.) Selenium powder (Acros Org.), 1-Hexadecylamine, HDA (Acros Org.) and Trioctylphosphine, TOP (Sigma Aldrich) are used as pure as supplied from the companies without further purification. The cadmium stock solution is prepared by mixing 513.6 mg CdO, 6.3 mL OA and 40 mL ODE. The mixture is evacuated with raising the temperature at 100 °C and then heated to 300 °C until a transparent solution is achieved. The injection solution is prepared by adding 0.4 mL of Se solution (1 M in TOP, prepared in glove box at 200 °C) to 1.6 mL of TOP and 2 mL of ODE. The synthesis is carried out under fumehood, with a Schlenk line connected to vacuum and pure Ar line. During the synthesis 4 mL of Cd stock solution is mixed with 2 g TOPO, 2 g HDA and 8 mL of ODE in a 3-neck glass flask. The mixture is evacuated under Schlenk line with raising the temperature to 100 °C under stirring. The mixture is then heated up to 300 °C under Ar flow and the temperature for injecting 4 mL of TOP-Se-ODE mixture is set to be

280 °C. The nanocrystals are grown under 250 °C within few minutes. The resulting QDs have a quantum yield of about 35%.

The synthesized CdSe nanocrystals synthesized have been used in our experimental work [77]. The emission and absorption spectra of the CdSe is given in Fig. 2.2.1.2.1 and the high resolution TEM image is given in Fig. 2.2.1.2.2.

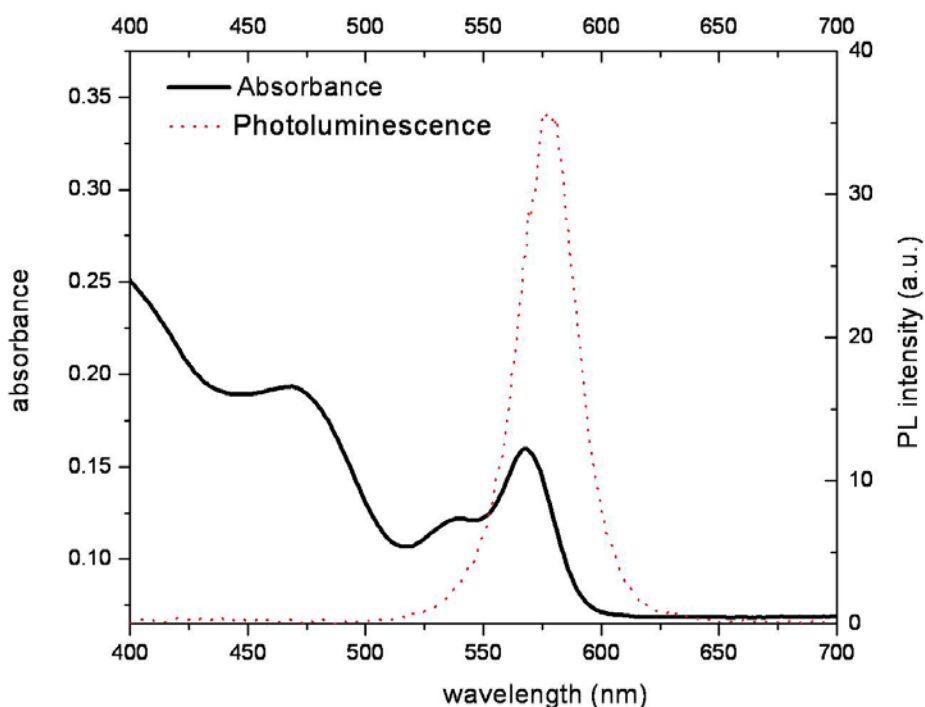


Figure 2.2.1.2.1 Photoluminescence and absorption of organic CdSe QDs at room temperature (Reproduced with permission after [77].)

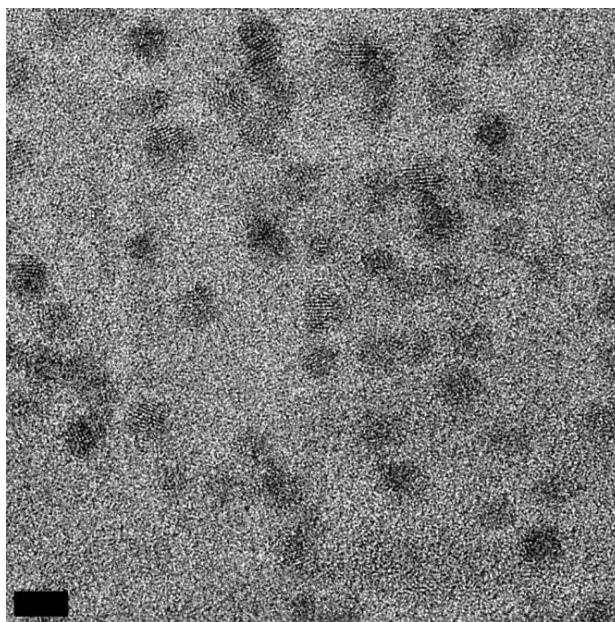


Figure 2.2.1.2.2 TEM image of organic CdSe QDs. The scale bar is 5 nm.

2.2.2 Synthesis of core/shell QDs

The synthesis of core/shell QDs is desired because of the well passivation of the core QDs, together with their resulting highly emissive profile. The core/shell QDs are regarded as type I or type II depending on the core and shell band alignment. In the type I architecture the electron and holes are confined in the core, whereas in the type II QDs, the electron is located in the core while the hole is in the shell, thus decreasing the overlap integral between their wavefunctions. The material of interest here is type I CdSe/CdS core/shell architecture. One of the important points in choosing the right material for overcoat is that there should not be a considerable lattice mismatch between the core and the shell. Otherwise, the resulting core/shell material will be suffering from the strain build-up. Starting with the core material, there are various recipes for overcoating. Unless the calculations are carried out precisely, the resulting core/shell QDs do not provide high quality optical properties. Here we follow a method of successive ion layer adsorption reaction (SILAR). In this approach, starting with the core material, first, the concentration of the core

material as well as the size of the core is calculated precisely using the absorbance value obtained from the spectrophotometer. The logic behind this method is to calculate the amount of shell material for each and every monolayer (ML) coated on the existing core. The amount of shell precursors for a single QD is calculated, and then multiplied with the total core QD amount, in order to predict a correct calculated value of shell precursor. As the number of monolayers increase, the next monolayer is coated with the appropriate amount of precursors taking into account the previous monolayer thickness increase.

2.2.2.1 CdSe/CdS core/shell QDs

The synthesis is based on the recipe followed by Bawendi Group [78]. For the synthesis of the core material, we use cadmium oxide (CdO), tetradecylphosphonic acid (TDPA) as the ligand, and octadecene (ODE) as the solvent. The mixture with pre-determined concentrations is heated up under inert atmosphere to 273 °C, followed by the injection of Selenium (Se)-Tributylphosphate (TBP) mixture. The desired core size is achieved upon continuing the synthesis after the injection of the Se precursor. Once the core material is ready, it is cleaned well from the excess ligands, using acetone-methanol extraction by centrifuging and dissolved in fresh hexane. Approximately 10 µL of the synthesized volume is used to determine the core size and the concentration.

Before the shell material is injected, we follow the preparation of Cadmium oleate. As a precursor for the synthesis, CdO dissolved in oleic acid (OA) and octadecene (ODE) is prepared under ambient atmosphere at 300 °C and kept in the glove box environment as cadmium oleate ready for the shell coating. For the overcoating, Cd-oleate and sulfur (S) dissolved in TOP is prepared in a glove box, taken in glass syringes and left aside. On the other side, CdSe, which is already prepared, is mixed with oleylamine and ODE in the system, and left

under vacuum for the evaporation of the hexane. At 180 °C, significantly below the core growth temperature, the Cd and S solutions are injected dropwise using a syringe pump and the formation of shell ML is completed. This kind of a complete and careful study results in highly efficient (near unity quantum efficiency), monodisperse nanocrystal QDs (see Fig. 2.2.2.1.1. for our high resolution TEM image), with a <30 nm emission FWHM value of a desired size. Fig. 2.2.2.1.2 shows the emission and absorption spectra of the core CdSe and CdSe/CdS core shell quantum dots synthesized. The quantum efficiency changes with the monolayers. Increasing the number of monolayers, the passivation increases. However, at the same time, induced strain also increases. At the very end, annealing increases the overall efficiency.

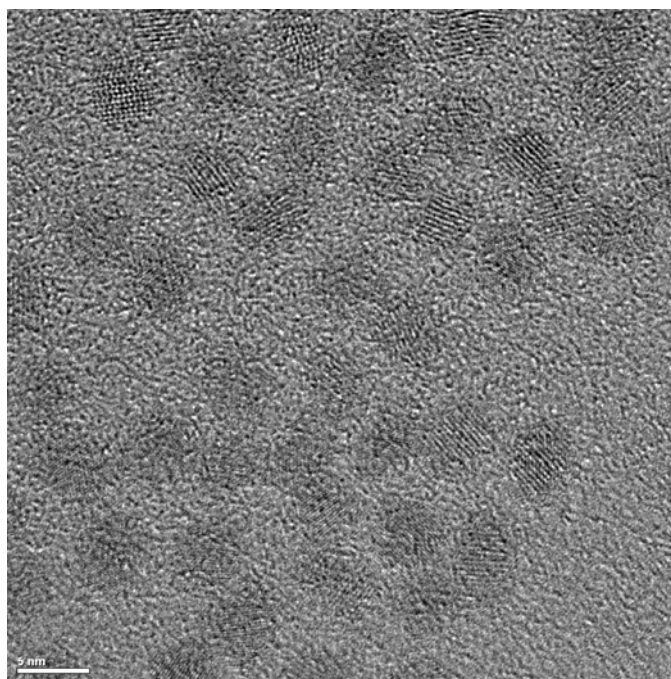


Figure 2.2.2.1.1 High resolution TEM image of the CdSe/CdS QDs. The scale bar is 5 nm.

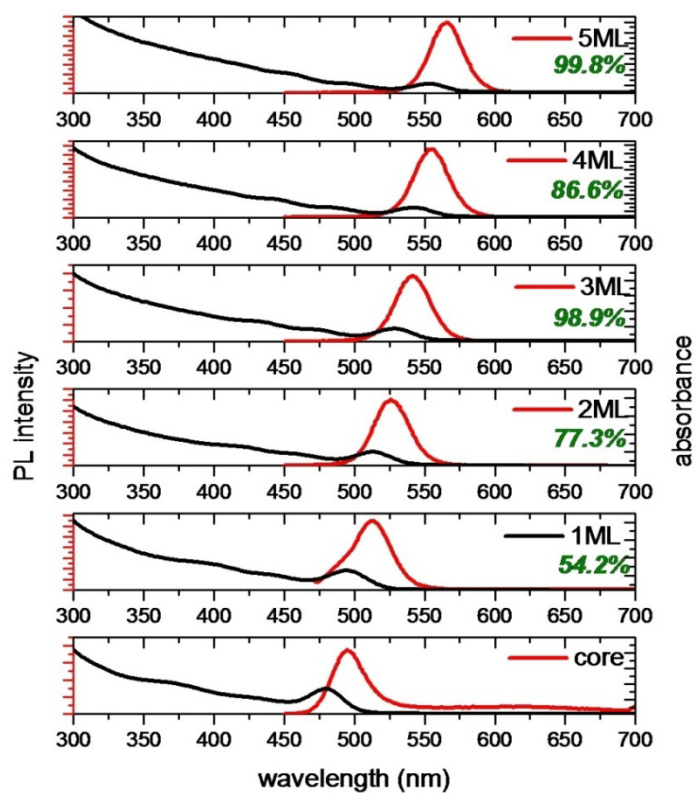


Figure 2.2.2.1.2 Emission and absorption spectra of the core CdSe and core/shell CdSe/CdS QDs at room temperature with an increasing number of shell monolayers (ML). The quantum efficiency values are given on each individual graph.

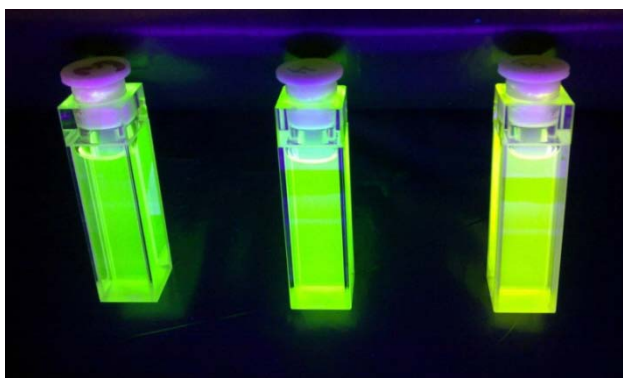


Figure 2.2.2.1.3 Picture of our highly efficient CdSe/CdS QDs under UV light.

2.3 Synthesis of III-V QD synthesis

2.3.1 InP/ZnS QD synthesis

All reactions are performed under inert Ar atmosphere on a Schlenk line or in a glove box. For the synthesis of the green emitting donor InP/ZnS QDs, we followed the recipe by Reiss and coworkers [79]. In a typical one pot synthesis, 0.1 mmol Indium Myristate (prepared by dissolving Indium Acetate in Myristic Acid, In:MA:1:4.3), 0.1 mmol Zinc Stearate, 0.1 mmol Dodecanethiol (DDT) and 0.1 mmol Tris(trimethylsilyl)Phosphine (TMS-P) are dissolved in 8 mL Octadecene, mixed in a 3-necked 25 mL flask and evacuated at room temperature. The mixture is quickly heated to 300 °C under Ar or N₂ flow, and the growth of the QDs occurs in minutes after the targeted temperature is achieved. Longer heating times result in shifting of emission peak. However, not only the heating time, but also the ratio of the chemicals used determines the optical properties of the resulting QDs. Increasing the concentration of the Myristic Acid in Indium Myristate, the emission red-shifts. Decreasing the DDT concentration blue-shifts the emission with decreasing the quantum yield. The QDs with FWHM values of 40-50 nm with a QE maximum of ~35% are achieved using this method described here. The absorption and emission profiles of the one pot synthesis of InP/ZnS QDs are given in Fig. 2.3.1.1 and Fig. 2.3.1.2.

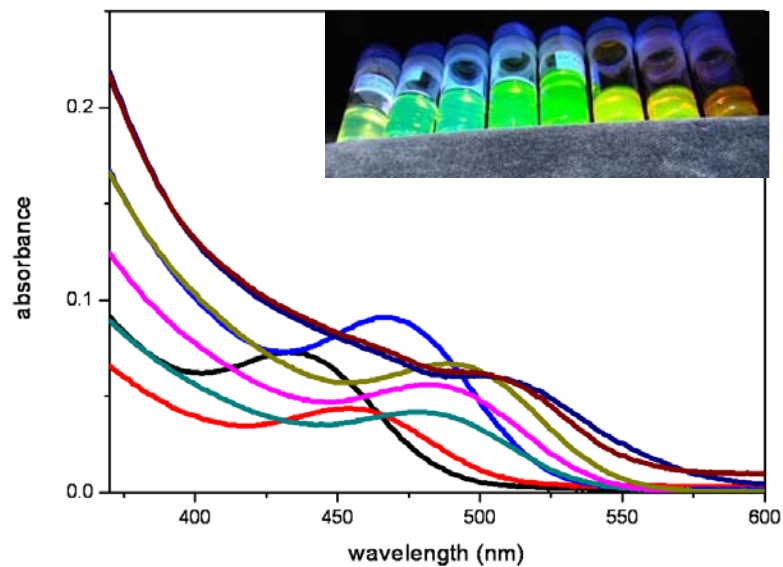


Figure 2.3.1.1 Absorption profile of one pot synthesis of InP/ZnS core/shell QDs at room temperature along with a picture of the dots under UV-illumination.

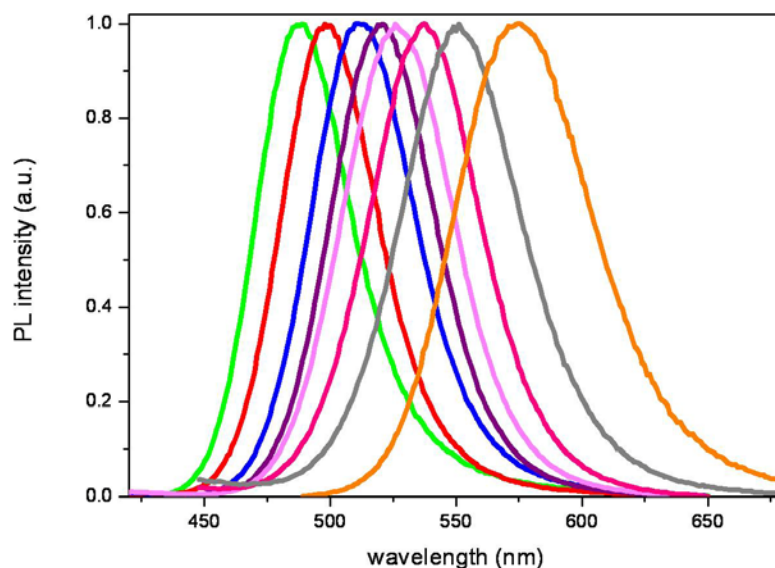


Figure 2.3.1.2 Emission profile of one pot synthesis of InP/ZnS core /shell QDs at room temperature.

In order to achieve orange/red emitting QDs, a modified version of a previous recipe [80] is used. For the core InP QDs, 0.1 mmol Indium Chloride, 0.1 mmol

Stearic Acid, 0.08 mmol Zinc Undecylenate, and 0.2 mol Hexadecylamine are dissolved in 3 mL ODE and heated to 240 °C under mixing in inert atmosphere. At that temperature the phosphor precursor (0.5 mL Tris(trimethylsilyl) Phosphite dissolved in octadecene, $c = 0.2$ mmol/mL) is injected and, after the core growth is established at 220 °C for 20 min, the mixture is cooled to room temperature. For the shell growth, 0.3 mmol Zinc Undecylenate is mixed with the prepared core QDs and evacuated well before heating. The solution is then heated up to 220 °C and 1 mL of Cyclohexyl Isothiocyanate/octadecene solution ($c = 0.15$ mmol/mL) is injected as the sulfur source followed by increasing the temperature to 240 °C and growth till the desired emission wavelength is achieved. The injection temperature of the core and shell determines the emission wavelength of the QDs synthesized. The best results achieved by injecting the core precursors at 240 °C and the shell precursors at 220 °C. Increasing the injection temperatures for the core and shell precursors red-shifts the emission. Fig. 2.3.1.4 and 2.3.1.4 shows the emission and absorption profiles of the different sized InP/ZnS QDs synthesized using two step approach.

Similar to the one pot synthesis approach, the quantum yields of the red-emitting QDs achieved by using a two step approach also results in relatively large FWHM values with smaller quantum yields compared to their II-VI counterparts. One possible explanation for such a kind of relatively low quality nanocrystals in the case of III-Vs is their surface trap states preventing the formation of high quality material [81].

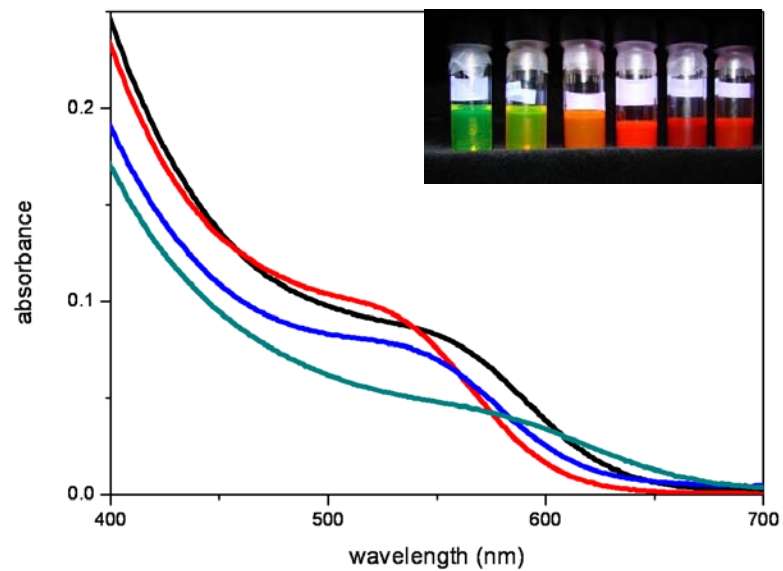


Figure 2.3.1.3 Absorption spectra of two step synthesis of InP/ZnS core/shell QDs at room temperature, along with a picture of the dots under UV illumination.

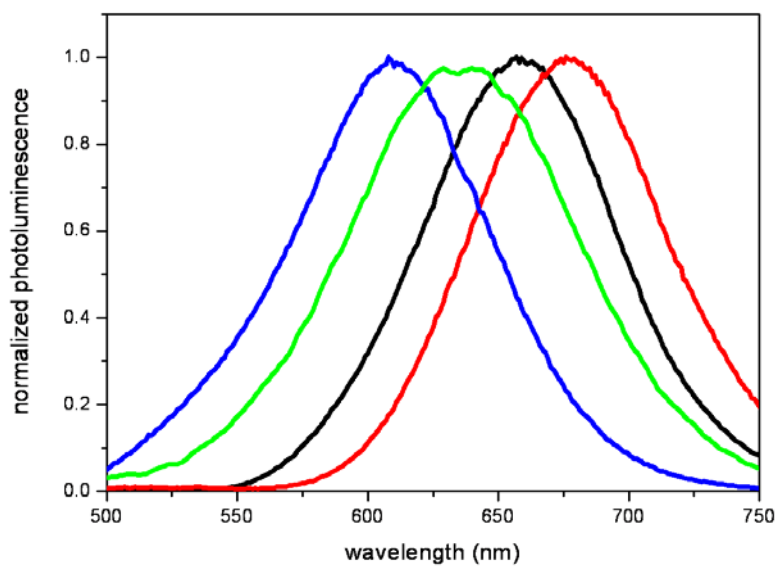


Figure 2.3.1.4 Emission spectra of two step synthesis of InP/ZnS core/shell QDs at room temperature.

Chapter 3

Nonradiative Energy Transfer

3.1 Excitation and de-excitation paths

Förster type nonradiative energy transfer can be modeled as a dipole-dipole interaction. Figure 3.1.1 illustrates the schematic representation of the donor and acceptor quantum dot species, together with their energy diagram showing the excitation and de-excitation paths as well as the energy transfer process. Here, the incident photon with energy ($\hbar\omega_{laser}$) larger than the band gap of the donor is absorbed by the donor and the acceptor (blue dashed line). The absorption of the incident photon is a relatively fast process and takes place within 10^{-15} s. The photoexcited electron at higher energetic states relaxes back to the lowest excited energy state. This relaxation occurs within 10^{-12} - 10^{-10} s [82]. The donor in the absence of the acceptor completes the process by recombination of the electron-hole pairs (red dashed lines). If this is a radiative recombination, the emission takes place in 10^{-10} - 10^{-7} s. When there is an acceptor QD in close proximity of a donor QD, there is a Coulombic interaction between the donor and the acceptor (represented by the black dashed line) due to the transient dipole moment and there is a probability of the energy transfer taking place. Satisfying the requirements of FRET, which will be explained in the following lines, there emerges a new possible energy transfer channel for the donor, in addition to the recombination channel. In the case of FRET, the excitation energy is transferred nonradiatively from the donor to the acceptor rather than yielding recombination in the donor. Due to the energy transfer, the excitation

energy is fed to the acceptor side and contributes to the subsequent photoluminescence of the acceptor. The size of the red arrow in the scheme depicts the increase in the absorption emission and the size of the green arrow shows the decrease in the donor emission as a result of the Förster type energy transfer mechanism.

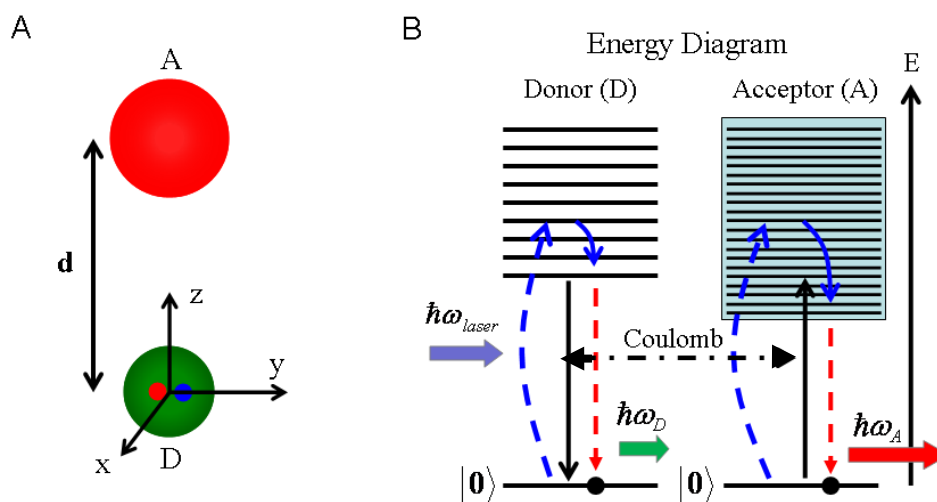


Figure 3.1.1 Diagram showing the possible excitation and de-excitation paths within quantum dot pairs.

3.2 Förster type Nonradiative Energy Transfer Mechanism

Förster resonance energy transfer (FRET) mechanism is a nonradiative-type energy transfer pathway that occurs between two close resonant molecules. It was proposed by Perrin [83] and Förster was the one after whom the mechanism was named, as Förster explained and resolved the discrepancies in the model taking into account the spectral bandwidth of the donor and acceptor (see Appendix for the derivation of the r^{-6} dependence of FRET). FRET has been used especially in biology as a spectroscopic nanoruler to determine the distance between the molecules.

FRET is the transfer of the excitation energy from the donor molecule to the acceptor molecule that is in very close proximity. In FRET mechanism, the

excited donor molecule transfers its excitation energy before the energy is radiated (in means of a photon emission). Therefore, it should not be confused with the radiative energy transfer, where the intermediate photons emitted by the donor, is absorbed by the acceptor. For the FRET to occur, the donor emission spectra should overlap with the absorption spectra of the acceptor molecule, the acceptor (not necessarily emitting) should have a high extinction coefficient, the donor should have a high quantum yield, and the donor and acceptor species should be in close proximity (typically <10 nm). Förster theory is based on dipole-dipole electromagnetic interaction under the long wavelength approximation. In cases where the molecules are <1 nm distance apart from each, if their wavefunctions start to overlap, the electron migration (not the excitation energy transfer) occurs, which was generalized by the Dexter theory. This does not happen for our core/shell nanocrystal structures where the wavefunction is fully confined.

In order to verify that the energy transfer is Förster like, not only steady state fluorescence measurement, but also time resolved spectroscopy is essential. As the donor is feeding the acceptor molecule with its excitation energy, the mechanism is clearly observed with the change in the lifetime of the donor molecule. The lifetime of the donor species decreases, whereas the acceptor lifetime increases due to the energy feeding. The commonly used method for determining the lifetime of the emitting species is based on the time correlated single photon count (TCSPC) method. In this method, the emitting sample of interest is excited by a short pulse of the excitation source (laser diode, or light emitting diode) and the photons are counted individually one after the other, at the end building up an histogram as the data is collected for sufficiently enough time period. The method is well understood and mature to be built up on a desktop equipment system (see Fig. 3.2.1).

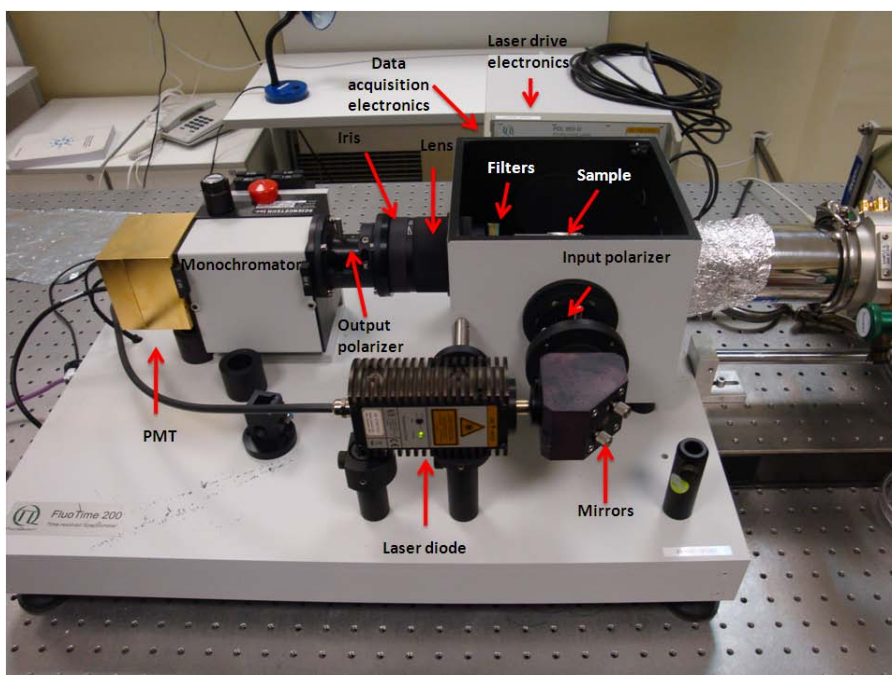


Figure 3.2.1 Fluo Time 200 Time Resolved Spectroscopy set-up at the Demir Lab.

The rate of energy transfer in FRET has an r^{-6} dependence given as

$$k_t = \frac{1}{\tau_D} \left(\frac{R_0}{r} \right)^6 \quad 3.2.1$$

where k_t is the rate of the energy transfer, and τ_D is the donor lifetime in the absence of the acceptor. Here the R_0 is given by

$$R_0 = 0.211(\kappa^2 n^{-4} Q_D J(\lambda))^{1/6} \quad 3.2.2$$

and known as the Förster radius, radius at which the transfer rate and the decay rate of the molecule is equally probable, and the FRET efficiency is 50%. κ^2 is the orientation factor; n is the refractive index of the media; Q_D is the quantum efficiency of the donor; and $J(\lambda)$ is the overlap integral given by

$$J(\lambda) = \int_0^{\infty} I_D(\lambda) \varepsilon_A(\lambda) \lambda^4 d\lambda \quad 3.2.3$$

Here, $I_D(\lambda)$ is the normalized emission spectrum of the donor, and $\varepsilon_A(\lambda)$ is the spectral extinction coefficient of the acceptor.

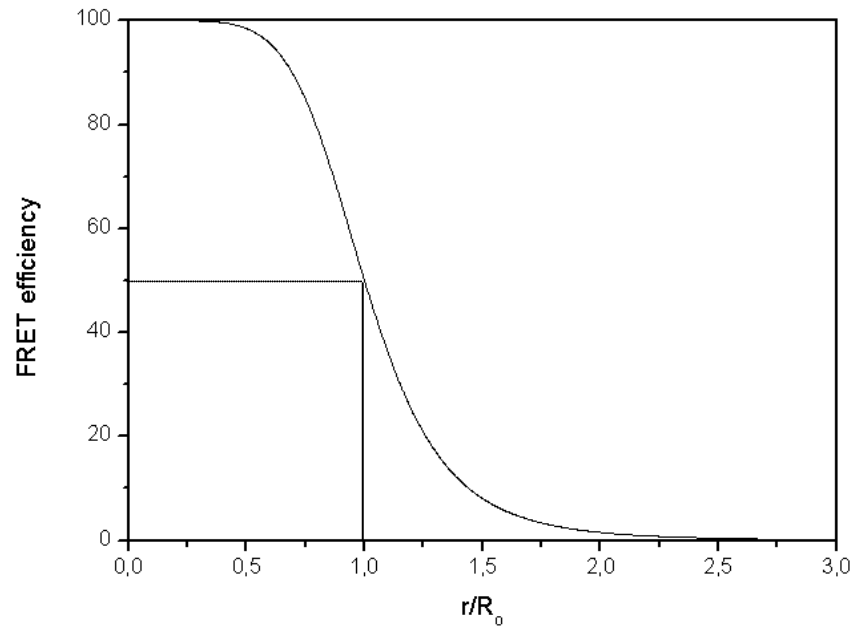


Figure 3.2.2 Dependence of the FRET efficiency on r/R_0 .

As it is shown in Fig. 3.2.2, FRET is effective in the region where $r \leq R_0$. As the energy transfer takes place, several observations are carried out for the investigation. These could be mentioned as the decrease in the donor steady state emission spectra and the lifetime shortening, the increase in the acceptor emission spectra and the prolonged lifetime. The FRET observations are mostly carried over the donor lifetime measurements; in this thesis work, the energy transfer for different systems has been verified by different method of observations.

Chapter 4

Experimental Methods

The methods used in the experiments in the scope of this thesis include photoluminescence spectroscopy and photoluminescence excitation spectroscopy, absorption spectroscopy, quantum efficiency measurement, time resolved photoluminescence spectroscopy, transmission electron microscopy, X-ray photoelectron spectroscopy, inductively coupled plasma mass spectroscopy, thermal gravimetric analysis, quartz crystal microbalance, contact angle measurement, and mechanical testing.

4.1 Photoluminescence spectroscopy and photoluminescence excitation spectroscopy

Photoluminescence and photoluminescence excitation measurements are commonly used to characterize the emission and excitation spectra of the samples. Photoluminescence measurements are carried out by setting the excitation wavelength and scanning the spectrum in the UV and visible, using monochromator equipped systems. In the photoluminescence excitation measurement, for a fixed emission wavelength, the excitation wavelength is scanned for a determined spectrum. The method determines the excitation wavelength appropriate to optically excite the samples.

In-film and in-solution photoluminescence and photoluminescence excitation measurements in this thesis are carried out using Varian Cary Eclipse Fluorescence Spectrometer and Horiba Yvon Fluorolog 3 system.

4.2 Absorption spectroscopy

Absorption measurements are used to investigate the interaction of the incident light with the sample. The monochromatic light incident on the sample is collected at the detector's end to obtain the absorbance value at a specific photon energy comparing it with the blank sample on the complementary light path. Depending on the absorption characteristics of the sample, one can figure out the optical characteristics of the sample. In-solution absorption measurements allow us to determine the particle concentration of a known extinction coefficient or the extinction coefficient of the material with a known concentration, using Lambert-Beer Law. In-solution as well as in-film measurements are made by the Cary UV-VIS spectrophotometer in this thesis.

4.3 Quantum efficiency measurement

The photoluminescence quantum efficiency (also called the quantum yield) is the ratio of the emitted photons per absorbed photons. The calculation of the photoluminescence quantum yields for the QDs is subtle, thus a careful calculation is needed for the analysis. The quantum yield of an unknown sample is

$$Q = Q_{ref} \frac{I}{I_{ref}} \frac{A_{ref}}{A} \frac{n^2}{n_{ref}^2} \quad 4.3.1$$

Here Q denotes the quantum efficiency; I , the spectrally integrated photon count; A , the absorbance value at the excitation wavelength used; and n is the refractive index of the media. "ref" stands for the reference sample.

In order to determine the quantum yield of unknown species, the reference sample with a known quantum yield is used for comparison. In our calculations of the quantum efficiency, we generally use an organic dye, Rhodamine 6G

dissolved in spectroscopic quality ethanol as the reference sample. The reference quantum yield of the dye is known to be 0.95 [84].

In Eqn. 4.3.1, the reabsorption and inner filter effects are not considered. If the sample and the reference sample are too concentrated, then the emission spectra may be misleading due to the inner filtering effect caused by the strong absorption. Apart from that, the excitation wavelength should be chosen carefully to prevent wrong analysis of the quantum yield. In our experiments for the determination of the quantum yield, the absorption curve of the reference dye and QDs are intersected as shown in Fig. 4.3.1. Subsequently, at the intersecting wavelength, both the reference dye and QDs are excited as shown in Fig. 4.3.1.

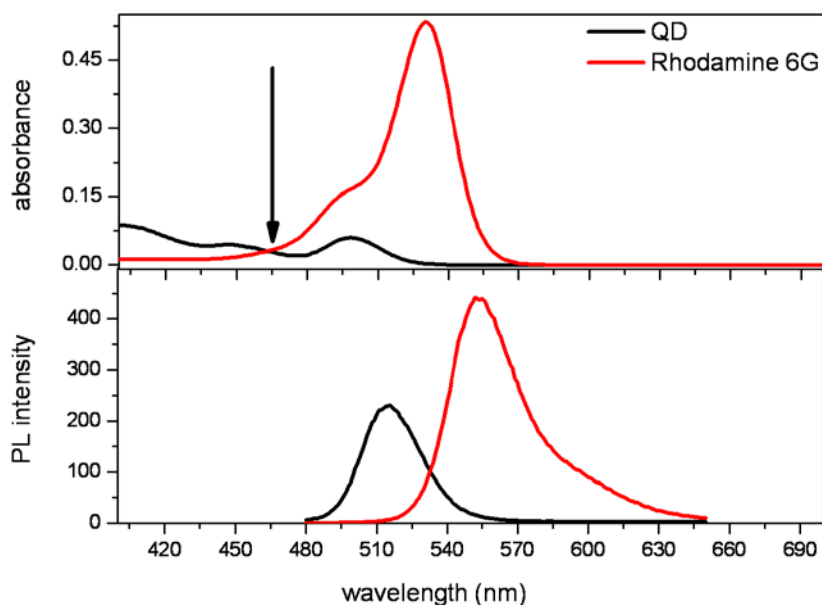


Figure 4.3.1 Emission and absorption spectra of the Rhodamine 6G used for the quantum efficiency measurements and the QDs. Black arrow represents the intersection point of the absorption spectra for both species, which is used as the excitation wavelength.

The absorbance level used for the spectral intersection point of the sample and the reference is chosen to be around 0.1 and the wavelength of this intersection of the absorption spectra is adjusted to be around 460-490 nm, where the slope

of the absorption of the Rhodamine 6G reference dye is flat [85]. Also since the dye sample is not emitting in this wavelength regime, the analysis is safe in means of the inner filtering effect. Finally, comparing the integrated intensities of the reference and the sample, and taking into account the correction for the refractive indices, the quantum yield is calculated.

4.4 Time resolved photoluminescence spectroscopy

Absorption and photoluminescence methods previously described are tools for studying the steady state response of the materials, whereas the time resolved photoluminescence is a very powerful method for determination of the emission kinetics of the sample. Equipped with a pulsed laser diode head, used for the excitation of the sample, with a very short pulse width (picosecond), the emission through the sample is collected as a function of time. This conveys the exponential decay characteristics of the emission dynamics by means of the, so called time correlated single photon count (TCSPC) method. Usually, the instrument response function (IRF) is also used considered for the deconvolution of the decay. The decays are fit with exponential functions to extract the lifetime components. The method allows us to determine the lifetimes (with amplitudes) of the samples, as well as to comment on the energy transfer mechanisms and the lifetime modifications of the samples. Equipped with the He-cryostat in close cycle, allowing for temperature dependent emission kinetics measurements (up to 10 K), we use Pico Quant Fluotime 200 Time Resolved Fluorescence set-up with optical components (mirrors, input-output polarizers, monochromator, iris, etc.), a high sensitivity detector, and timing electronics. The laser diode is operating at 375 nm, with a 80 MHz repetition rate, and a 200 ps width. Data acquisition is carried out by Pico Harp 300 system with a lifetime resolution <10 ps. Data analysis is done by using FluoFit Pro.

4.5 Transmission electron microscopy

Transmission electron microscopy (TEM) allows one to obtain an atomic resolution image of the sample used. Being equipped with a complex electronics, the electron beams of very high energy (10's-100's of keV) is incident on the sample, and the transmitted electrons are focused by the electron lenses. The crystal planes and diffraction patterns can be observed. TEM (FEI, Tecnai G2 F30) has been used to determine the size and shape of the nanocrystalline samples as well as the crystal interplanar spacing.

4.6 Others

Although measurement techniques described below have not been used frequently, they have also been utilized in this thesis and included in this subsection.

4.6.1 X-ray photoelectron spectroscopy

X-ray photoelectron spectroscopy, known as XPS, is a method to determine the elemental composition of the surface of the sample based on the photoelectric effect. Highly energetic X-ray photons incident on the sample eject electrons from the surface. Binding energy of the ejected electrons can be measured using the energy conservation. The binding energy of the electrons, specific to the element, allows the determination of the composition, as well as the stoichiometry of the elements within the sample. The measurement is carried out under high vacuum conditions. The method also allows for depth analysis using the ion beam etching of the sample. XPS (Thermo, K-Alpha high-resolution XPS) is used to study the elemental compositions of the films of nanocrystals within a host matrix.

4.6.2 Inductively coupled plasma mass spectroscopy

Inductively coupled plasma mass spectroscopy (ICP-MS) allows for determining the trace of the elements in solution with ppt (parts per trillion) sensitivity. The Ar plasma decomposes the sample in dispersion to its elemental composition. Using the difference of the masses of the elements under consideration, the equipment allows to determine the exact amount of material within the sample and compare it with the known elemental amount of a control sample. ICP-MS (Thermo Fisher X Series 02) is used for determining the stoichiometry of the alloyed nanocrystal structures.

4.6.3 Thermal gravimetric analysis

Thermal gravimetric analysis (TGA) is used for determining the weight loss by controlled heating of the sample up to 900 °C. Different elements in a compound, e.g., in a powder form, can be investigated by burning the sample under controlled conditions. The implementation of the change in mass with respect to the temperature allows to determine the mass ratio of the sample contents. TGA (TA Instruments, TGA Q500) is used for the determination of the ligand content within the nanocrystals.

4.6.4 Quartz crystal microbalance

The equipment is used for accurate determination of the mass accumulation on the substrate of the quartz crystal by the measurement of the change in the oscillation frequency of the quartz crystal resonator. The method is very powerful for the verification of the monolayer films. Qsence QCM is used in this thesis, for the verification of the binding of the proteins to the nanocrystals.

4.6.5 Contact angle measurement

This technique is used to determine the surface hydrophobicity of the sample. This method allows us to characterize the surface, whether it is hydrophobic or

hydrophilic. The angle at which the nanocrystal-polymer surface makes with the water drop is measured with Dataphysics, OCA 15-EC.

4.6.6 Mechanical testing

Mechanical testing is a tool for characterization of the sample mechanically, by applying a load on the regular shaped sample. By controlled stretching of the material under consideration, the stiffness and elasticity information can be obtained. The characterization tool (Instron 5969 MTS) is used for determining the tensile strength of the nanocrystal-polymer films.

Chapter 5

Exciton harvesting of nanocrystal quantum dots for green fluorescent proteins

This chapter is based in part on the paper work of “Exciton harvesting of nanocrystal quantum dots for green fluorescent proteins,” by Evren Mutlugun, Urartu Ozgur Safak Seker, Pedro Ludwig Hernandez Martinez, and Hilmi Volkan Demir, in submission (2011).

5.1 Introduction

Green fluorescent protein (GFP) is found in a marine organism, *Aequorea Victoria*, known as the jelly fish [86]. In nature, the emission of the GFP at 508 nm takes place, when another protein aequorin interacts with Ca^{2+} ions and emits at 440 nm, which consequently excites GFP [87,88]. Here we extensively study a synthetic approach to mimic the excitation/emission process of GFP-aequorin pair where the aequorin protein was replaced with ZnCdSe QDs which has a longer lifetime compared to that of aequorin. Mediating the energy transfer mechanism between the QDs and the fluorescent proteins, we achieve light harvesting for the GFP up to 15 folds, by overcoming the narrow excitation window of the GFP, together with high levels of lifetime modifications. The synthetic composite of ZnCdSe GFP-QD (which will be called “GFP-QD” further on in the chapter) is subsequently utilized for biosensing applications.

The use of FRET involving fluorescent proteins with QDs have been studied for biotargeting and biosensing purposes thus far [89,90]. However, in the context

of this chapter, we propose the light harvesting of the QD-GFP in a complex for light harvesting applications mediated by FRET mechanism together with the demonstration of the enzymatic reaction for controlling the binding of the donor-acceptor pair.

5.2 Results and Discussion

Within the context of this approach, we followed a route where we started from the basics of the composite formation to the FRET facilitating QD-GFP system. Fig. 5.2.1 shows the emission spectrum of the donor ZnCdSe QDs and the absorption spectrum of the GFP showing that the donor photoluminescence matches well with the absorption of the protein to provide an efficient FRET pair.

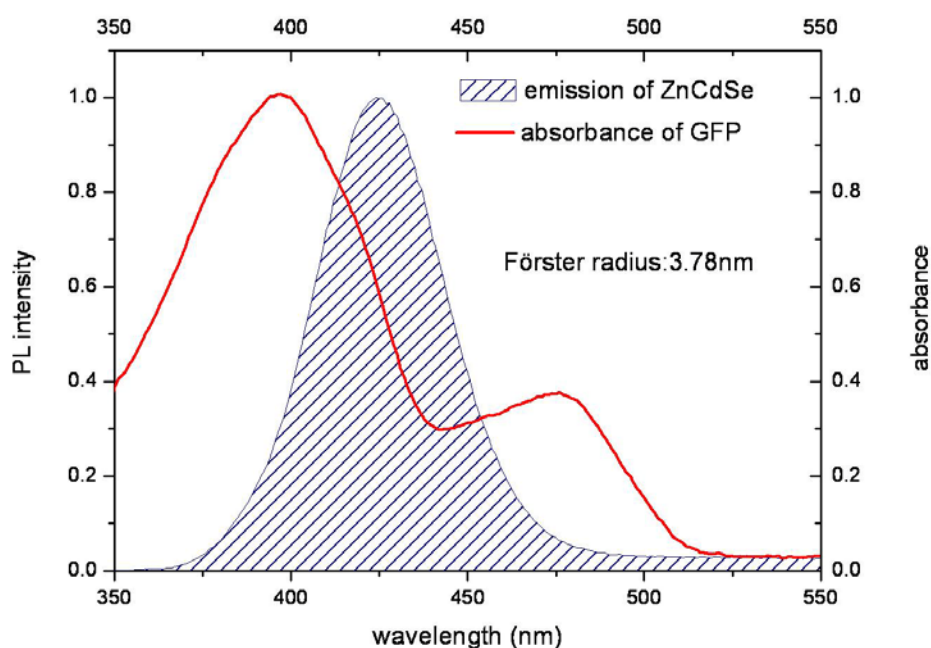


Figure 5.2.1 Donor ZnCdSe QDs emission and acceptor GFP absorption spectra at room temperature.

The synthesis of the QDs is described in the literature [91] . The high resolution TEM image in Fig. 5.2.2 shows the interplanar distance between the atomic planes of the ZnCdSe QDs (scale bar is 2 nm). Since the material is known to reveal cubic structure the unit cell volume is given by Eqn. 5.2.1. The interplanar distance is measured to be 0.31nm for the QDs used. The extinction coefficient is measured experimentally to be $\sim 75,000 \text{ M}^{-1} \text{ cm}^{-1}$.

$$V_{\text{unitcell}} = a^3 \quad 5.2.1$$

Using the size information from the TEM image (see Fig. 5.2.2), one can determine the volume of 1 QD, considering the dots to be spherical, thus given by Eqn. 5.2.2. Therefore the ratio of the volume of the QD to the volume of the unit cell gives us the information on how many unit cells is roughly present in one QD.

$$V_{\text{dot}} = \frac{4}{3} \pi r^3 \quad 5.2.2$$

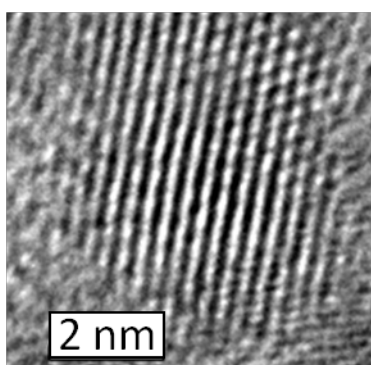


Figure 5.2.2 High resolution TEM image of the ZnCdSe QDs.

If the density of the crystal structure is known, then the mass of the QD in the dispersion of a known volume can be extracted. However, since ZnCdSe is an

alloy structure, here we determine the stoichiometric ratios of the Zn:Cd:Se using the inductively coupled plasma-mass spectroscopy (ICP-MS). As the experiment is carried out, we find the crystal to be $Zn_{0.94}Cd_{0.06}Se$. We can calculate the alloyed QD density by using the weighted densities of the ZnSe and CdSe. The important issue to be addressed here is that the QDs are not only consisting of the atoms building them up, but also there are organic ligands attached to them which make them stable in dispersion. Therefore, a careful analysis needs to be implemented to determine how much of the mass is consisting of the pure elemental constituents itself. To do that, thermo gravimetric analysis (TGA) is used to obtain the mass percentage of the elements of the QDs forming the QDs. Once we have the pure mass of the dispersion of known volume, we calculate the concentration of the QDs in the dispersion.

Although the ultimate aim is to build a functioning FRET facilitating QD-GFP system, we start with the study of the binding of GFP to QDs to form the composite structure. The affinity of the GFP to ZnCdSe is tested using quartz crystals microbalance (QCM). In this test, first the surface of the QCM crystal is decorated. This has been done by the surface functionalization with cysteamine, where the $-SH$ group of the molecule is covalently bound to the gold surface of QCM sensor. The other end of the cysteamine contains NH_2 group, which can be coupled to the carboxyl groups existing on the ZnCdSe QDs. This coupling is achieved using the 1-ethyl-3-(3-dimethylaminopropyl)-carbodiimide (EDC) as the activation agent, which provides the immobilization of nanoparticles on gold surface. Following the immobilization of the QDs, GFP is delivered onto the surface immobilized QDs using a peristaltic pump at a flow rate of $2.5 \mu L/min$. To observe the interaction of GFP with the surface immobilized dots, a concentration dependent strategy is followed to extract the kinetic adsorption constant of the GFP to the QD surface. The absorption of the GFP on QDs is monitored between 2-10 μM concentration range. (Fig. 5.2.3) After pumping each concentration, the weakly bound and non-specifically bound GFP

molecules is removed, with an extensive washing step with using the buffer solution to satisfy the specific binding of GFP on QD surface.

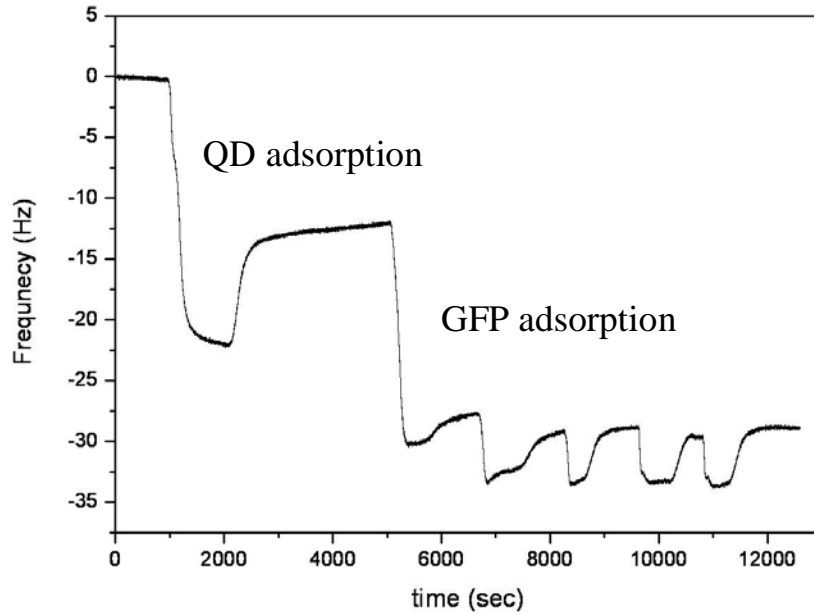


Figure 5.2.3 Adsorption isotherms of GFP on QD modified surface of QCM sensor.

The binding experiments from QCM is fit using the simple Langmuir model [92] to calculate the affinity constant of the GFP bound to QDs. The model is given by Eqn. 5.2.3.

$$\Delta f = \frac{f_{\max} \times C}{K_D + C} \quad 5.2.3$$

Here, Δf denotes the frequency shift as the protein is adsorbed, f_{\max} is the maximum frequency, which corresponds to the saturation frequency due to adsorption, C is the corresponding protein concentration, and K_D is the constant of the binding affinity.

The frequency change in the QCM signal is taken after the adsorption of the each delivery of the protein at a certain concentration on the immobilized dot

surface as shown in Fig. 5.2.3. Each shift upon GFP adsorption is plotted as a function of GFP concentration. Using the single Langmuir adsorption model, we calculate the affinity constant for the binding of the GFP. The equilibrium binding constant for GFP is found to be $6.9 \pm 1.2 \times 10^6 \text{ M}^{-1}$. Compared to the binding information of peptides and proteins on solid surfaces, the affinity of the GFP to dot surface is satisfactory and comparable with the affinity of the most of the thiol based linkers to solid surfaces [93]. The adsorption isotherm and the fitted single Langmuir model curve are given in Fig. 5.2.4. The results indicate that GFP is capable of binding to the surface bound ZnCdSe QDs, which means that the functioning of GFP is good enough to build a composite assembly of QD-GFP.

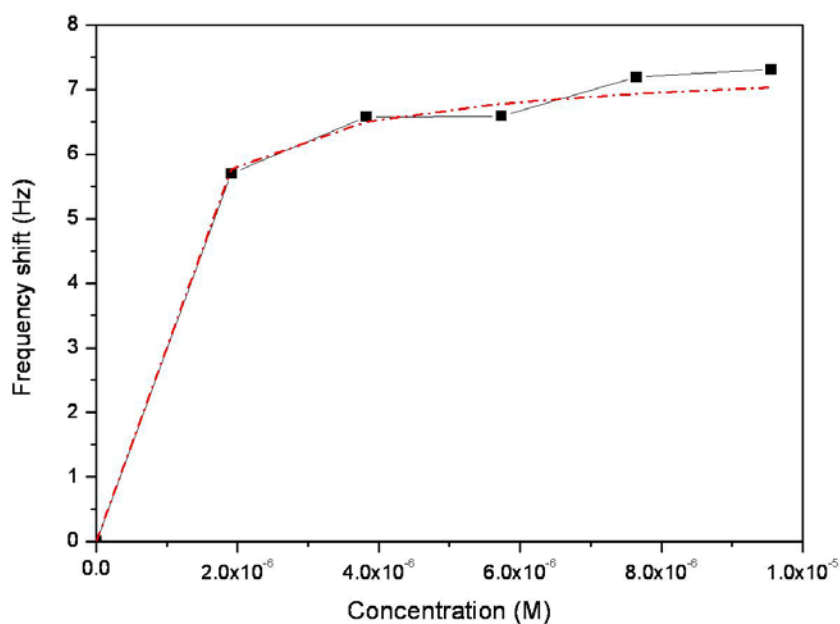


Figure 5.2.4 Single Langmuir adsorption model fit to the adsorption data of his-tagged GFP on surface bound QD. The red line represents the fit as the black dots denote the data points.

In order to verify the formation of the nanobiocomposite, another tool is utilized to test the composite material based on a thermal method, namely the thermogravimetric analysis (TGA). In this approach, we track the change in the

mass of the nanocomposite as a function of temperature. As given in Fig. 5.2.4, increasing the temperature from 50 to 550 °C and monitoring the decomposition of GFP bound around the QD, we observe three different peak points. Each of the peak points represents the decomposition of different groups within the QD-GFP composite (see Fig. 5.2.5).

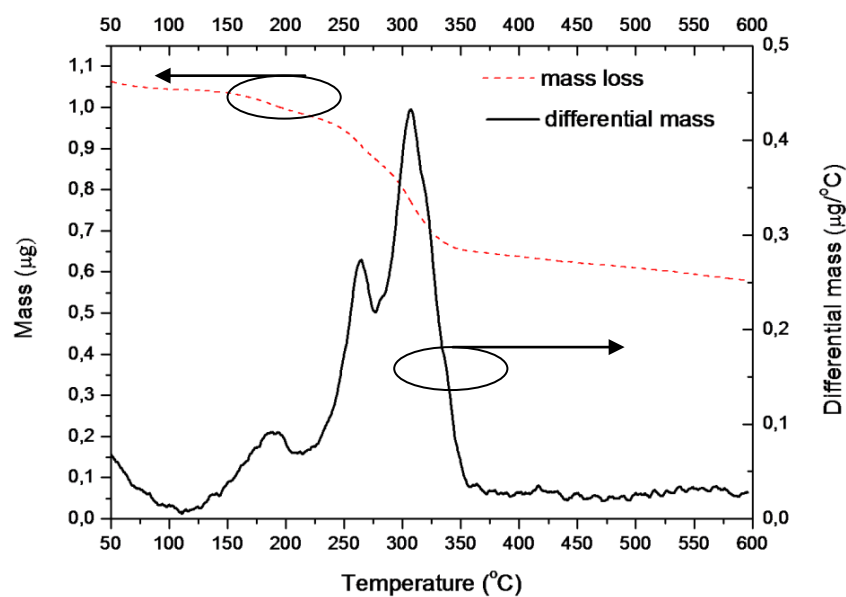


Figure 5.2.5 Mass change monitored in TGA and the derivative of mass change as a function of temperature for the nanocomposite.

Compared to TGA of the QDs alone (Fig. 5.2.6), there is a shift in the peaks of the QD decomposition points, which is due to the formation of the nanocomposite triggered upon a strong interaction between the QD and GFP.

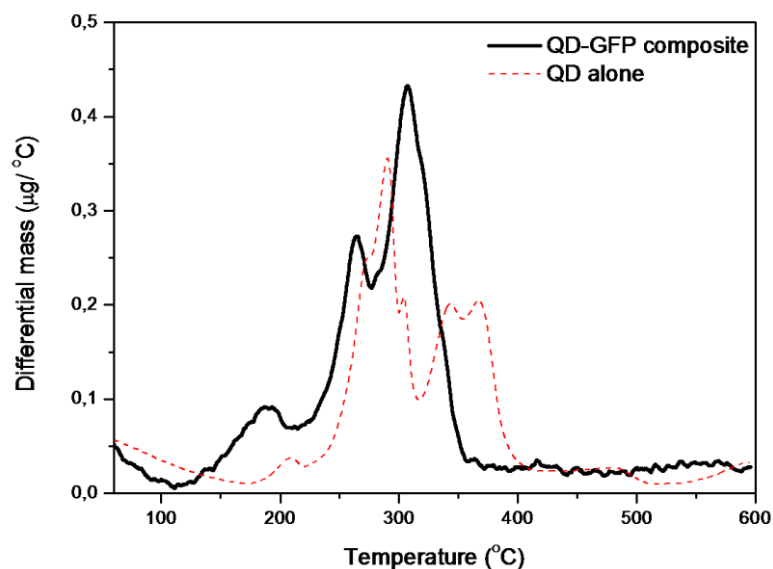


Figure 5.2.6 Comparison of the temperature derivative mass change data for QD and QD-GFP composite material. The shift in QD peaks and emergence of new peaks suggest the formation of new composite material.

Having proved that the system is a composite, we worked on the verification of the energy transfer among the QD-protein complex. In order to study the energy transfer mediated light harvesting, we have performed steady state and time resolved photoluminescence measurements. The steady state measurements demonstrate the effect of the energy transfer from the QDs (D) to GFP (A). As the A/D ratio is changed, we observe the decrease in the emission spectra of the donor QDs, whereas an increase in the acceptor emission spectra is observed as a result of energy feeding from the donor side.

The steady state emission measurements are performed with Cary Fluorometer with the excitation monochromator set at 315 nm. To demonstrate the excitation of the GFP well beyond its excitation spectra, we choose our excitation wavelength to be 315 nm, since the photoluminescence excitation (PLE) intensity of the bare GFP is much lower compared to the bare PLE of the donor QDs specifically characterized at their individual emission wavelengths. The

PLE intensities of the bare GFP and bare QD are given in Fig. 5.2.7 together with their ratio.

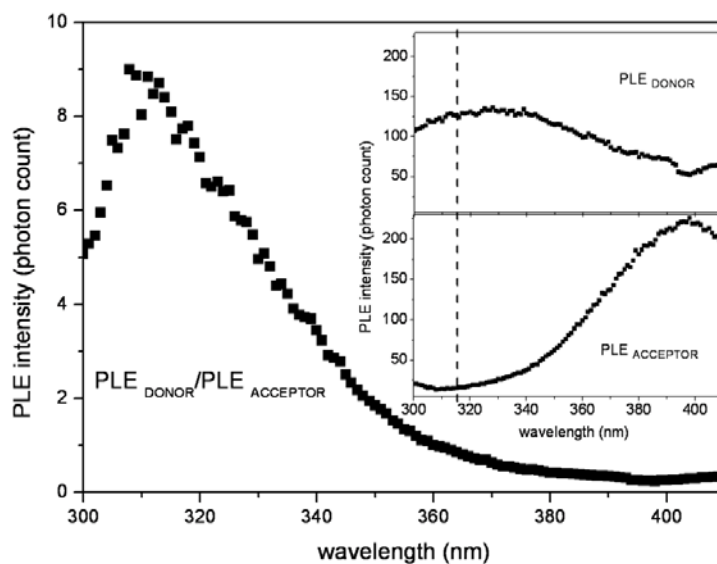


Figure 5.2.7 PLE intensity ratio of the bare QDs at its emission wavelength of 422 nm compared to the bare GFP at its emission wavelength of 508 nm at room temperature. The insets show the individual PLE intensities of the GFP and the QD alone.

The photoluminescence measurements of the dot-protein composite are shown in Fig. 5.2.8. The control experiments are also performed to check the emission of the GFP without donor QDs corresponding to the same acceptor concentration which is used in the donor-acceptor hybrid approach (Fig. 5.2.9). In the control group, due to the increase in the acceptor concentration in solution, the bare GFP intensity also increases. However, the intensity increase of the GFP in the presence of donor QDs is much higher as a result of the nonradiative energy transfer.

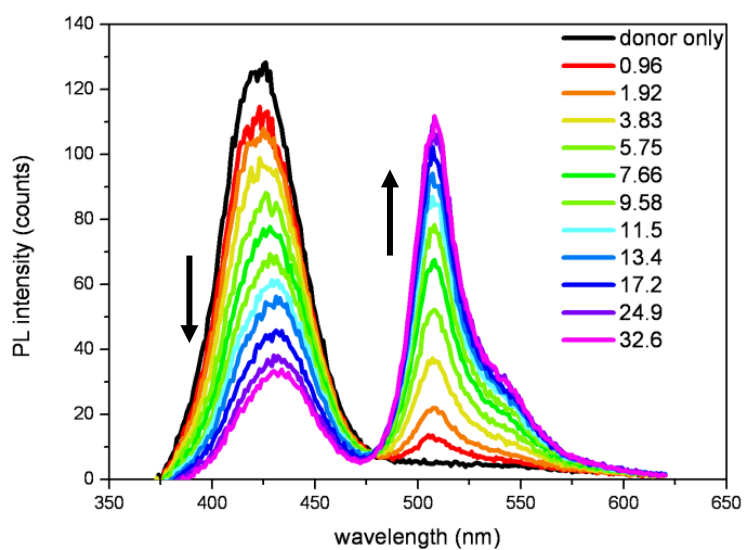


Figure 5.2.8 Change in photoluminescence of the donor-acceptor QD-GFP system with changing A/D concentration ratio (excitation at 315 nm) at room temperature.

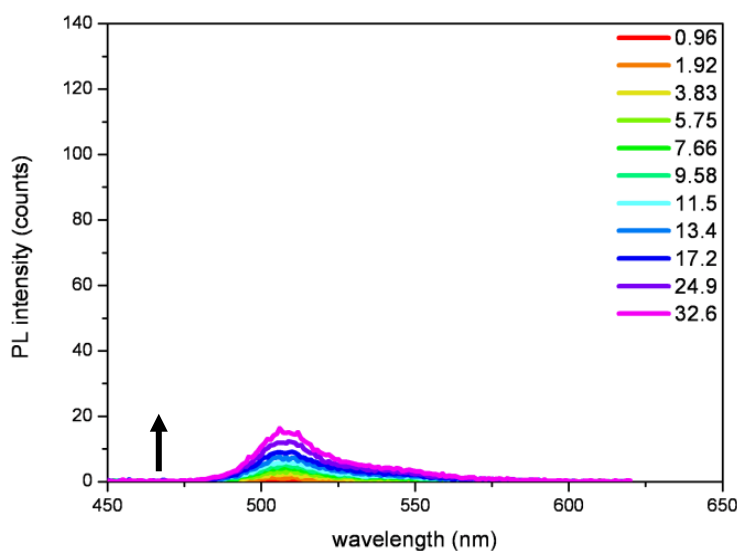


Figure 5.2.9 Control experiments for the photoluminescence of acceptor GFP only with the same acceptor concentration, corresponding to the A/D concentration ratio (excitation at 315 nm) at room temperature.

The enhancement of the bare acceptor emission is extracted from the steady state emission data of the GFP in the presence and absence of the donor QDs. The results are also shown in Fig. 5.2.10.

The enhancement of the acceptor emission is calculated through

$$Enhancement = \left[\frac{\int_{480}^{620} I_A^D(\lambda) d\lambda}{\int_{480}^{620} I_A(\lambda) d\lambda} - 1 \right] \quad 5.2.4$$

Here, I_A is the intensity of the acceptor GFP in the absence of the donor QDs and I_A^D is the intensity of the acceptor in the presence of donor. The wavelength interval from 480 to 620 nm is chosen since the emission spectra of the GFP lies within this region. Carrying out the analysis, we observe the enhancement of the acceptor photoluminescence up to 15 folds corresponding to the A/D ratio of ~ 4 , which is in good agreement with the geometry given in Fig. 5.2.16. As the amount of GFP is further increased, the overall enhancement decreases, because the system is approaching to the case of acceptor only, when A/D is increased further.

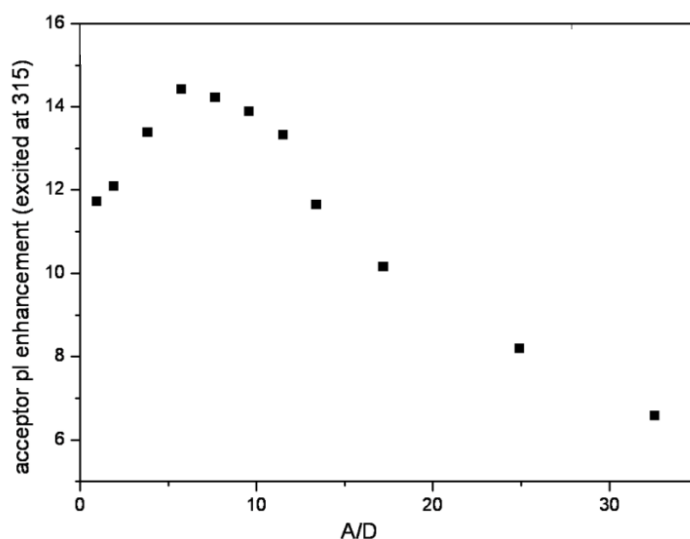


Figure 5.2.10 Enhancement of the GFP photoluminescence using QDs when excited with 315 nm monochromatic light at room temperature.

To verify the energy transfer, we also perform time resolved photoluminescence measurements both at the donor and acceptor emission wavelengths, at 422 and 508 nm, respectively. As changing the concentration of the GFP to QDs, namely

the acceptor/donor concentration ratio, we observe a drastic change in the lifetime of the donor QDs. The experiment was performed using the Pico Quant Time resolved fluorescence set-up. Starting with the A/D concentration ratio of 0.96, we observe the photoluminescence decays getting faster with increasing A/D ratio (see Fig. 5.2.11)

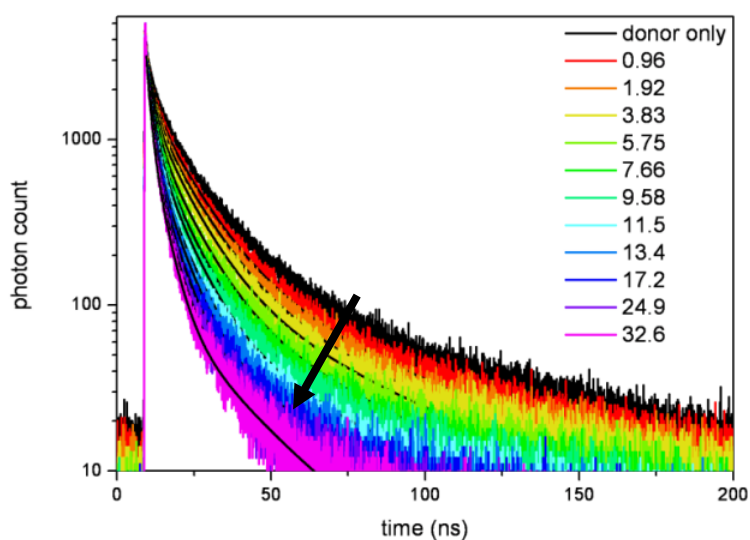


Figure 5.2.11 Time resolved photoluminescence decays of the donor changing with A/D at room temperature.

Here the double exponential fits were used for the observed experimental decays. The lifetime of the donor changes from 10.33 to 2.91 ns as we increase the A/D concentration ratio (Fig. 5.2.12). The change in the lifetime of the donor species in the presence of the acceptor in solution implies the nonradiative type energy transfer.

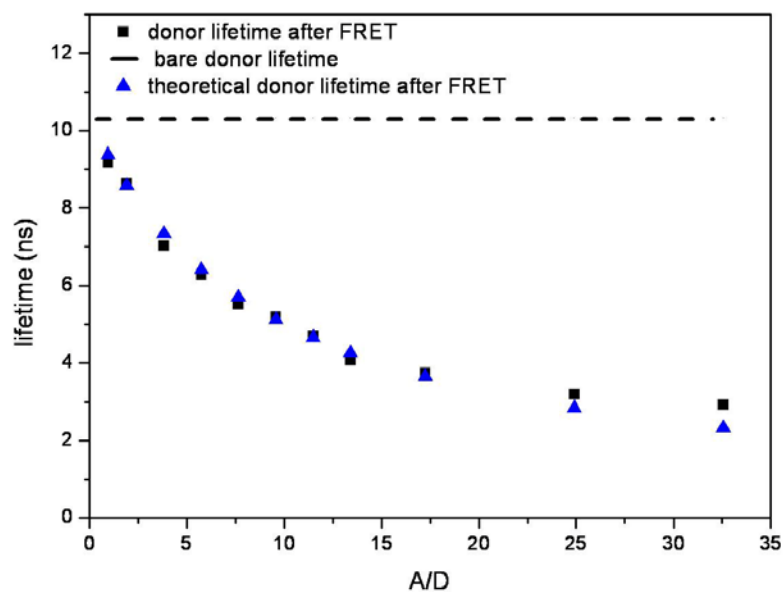


Figure 5.2.12 Donor lifetimes, extracted from time resolved photoluminescence decays, and theoretically predicted, as a function of A/D at room temperature.

In a similar fashion, we also carry out the lifetime measurements from the acceptor side (Fig. 5.2.13). This time, due to the energy feeding from the donor to the acceptor, the acceptor lifetime increases in the presence of donor QDs. For all the different values of A/D studied, we observe an increase in the lifetime values of the acceptor from 3.11 to 4.67 ns for the GFP (Fig. 5.2.14).

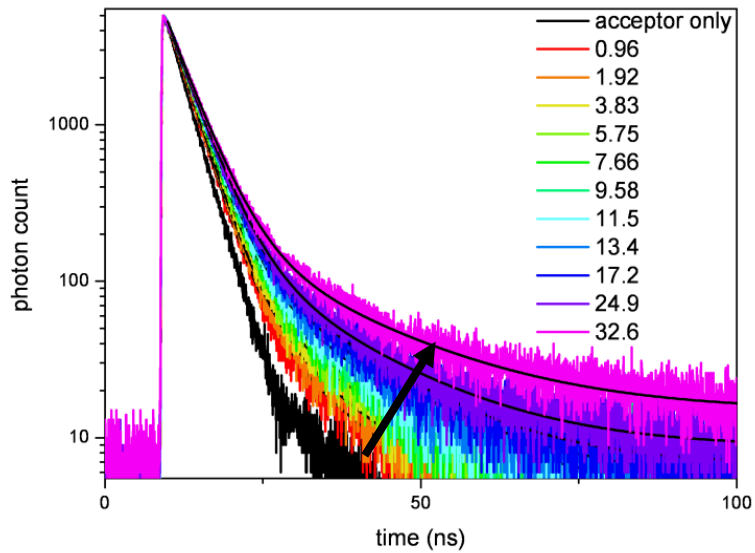


Figure 5.2.13 Time resolved photoluminescence decays of the acceptor changing with A/D at room temperature.

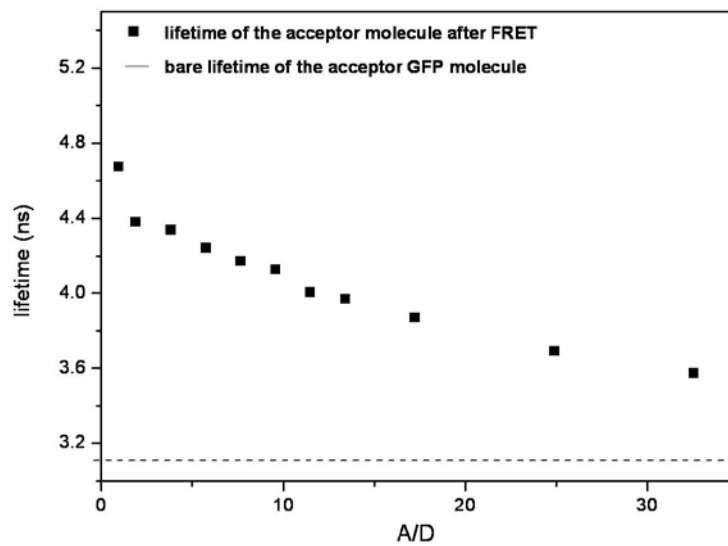


Figure 5.2.14 Acceptor lifetimes, extracted from time resolved photoluminescence decays, as a function of A/D at room temperature.

The observed FRET efficiencies due to the dipolar interaction of the donor acceptor pairs is calculated using Eqn. 5.2.5.

$$\eta = 1 - \frac{\tau_{DA}}{\tau_D} \quad 5.2.5$$

where τ_{DA} is the lifetime of the donor in the presence of the acceptor and τ_D is the bare lifetime of the donor. We observe up to 70% FRET efficiencies for our QD-GFP complex (see Fig.5.2.15). In connection with the theoretical model based on the dipole-dipole interaction, the efficiency levels are in good agreement with the experimentally observed values.

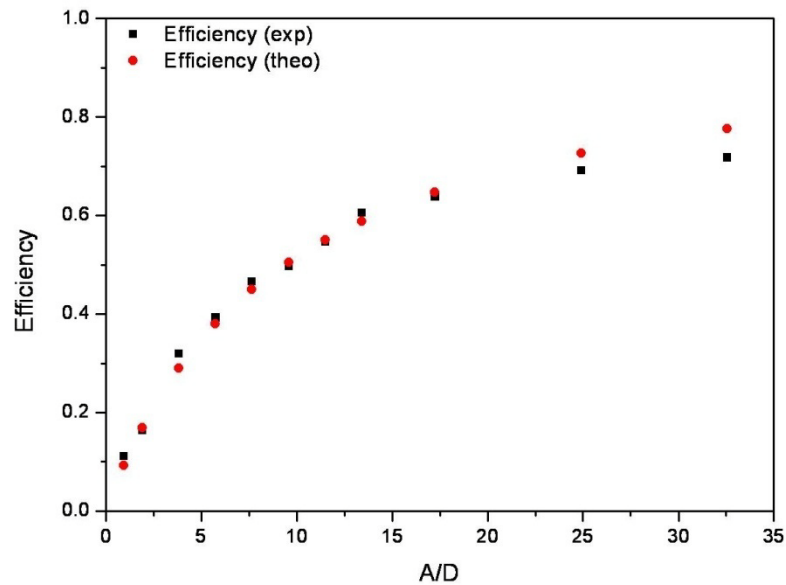


Figure 5.2.15 Theoretical and experimental FRET efficiencies extracted from lifetime measurements at room temperature.

In the theoretical approach, we consider energy transfer from ZnCdSe QD to multiple GFP molecules under exciton-exciton interaction. Within the simplest rate model, the number of excitons (N_{exc}) trapped in the QD, under constant illumination (steady-state condition), is given by

$$-(\gamma_{exc}^D + \gamma_{trans}^{tot})N_{exc}^D + I_D = 0 \quad 5.2.6$$

where N_{exc}^D is the number of donor excitons, I_D is the exciton generation rate due to the light excitation, and $\gamma_{exc}^D = \gamma_{exc,rad}^D + \gamma_{exc,non-rad}^D$ is donor exciton recombination rate in the absence of acceptor. $\gamma_{exc,rad}^D$ and $\gamma_{exc,non-rad}^D$ are the radiative and nonradiative component of γ_{exc}^D . $\gamma_{trans}^{tot} = n\gamma_{trans}$ is the total energy transfer rate between the donor and multiple acceptors. n is the number of acceptor and γ_{trans} is the energy transfer between one donor and one acceptor. By substituting γ_{trans}^{tot} into Eqn. 5.2.6, it can be written as

$$-(\gamma_{exc}^D + n\gamma_{trans})N_{exc}^D + I_D = 0 \quad 5.2.7$$

One defines

$$\gamma_{DA}^D = (\gamma_{exc}^D + n\gamma_{trans}) \quad 5.2.8$$

where γ_{DA}^D is the donor exciton lifetime in the presence of energy transfer. For the energy transfer rate between ZnCdSe QD and GFP, we assume to be Förster-type $\gamma_{trans} = \gamma_D \left(\frac{R_0}{r}\right)^6$, where R_0 is the Förster radius for the D-A pair and r is the separation distance between ZnCdSe QD and GFP. (This assumption is reasonable because the energy transfer between spherical QDs is well described by the Förster theory [94]). Therefore Eqn. 5.2.8 is given as Eqn. 5.2.9

$$\gamma_{DA}^D = \gamma_{exc}^D \left(1 + n \left(\frac{R_0}{r}\right)^6\right) \quad 5.2.9$$

In terms of lifetimes,

$$\tau_{DA}^D = \frac{\tau_{exc}^D}{1 + n \left(\frac{R_0}{r} \right)^6} \quad 5.2.10$$

Here we have considered the distance between the QD-GFP to be 5.49 nm in average, using the semi empirical approach, which is reasonable when compared with the QD diameter of 3.72 nm and GFP size.

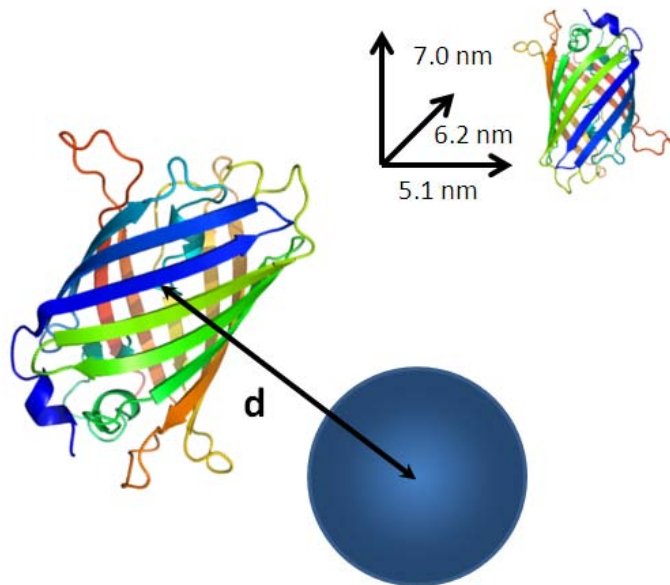


Figure 5.2.16 Schematic representation for the energy transfer from QD to GFP (not drawn to scale). Picture shows a QD surrounded by a GFP molecule. “d” represents the average separation distance between the QD and the GFP over which energy transfer takes place. Inset: Dimensions for the GFP molecule [95].

The enhancement in the FRET efficiencies does not reflect the observed light harvesting enhancement. This is because, as more and more acceptors are introduced, there are more nonradiative channels created for the donor to transfer energy, which results in high FRET efficiencies. On the other hand, the light harvesting is optimal up to a certain level of acceptor per donor amount. When A/D is increased further, the amount of light harvesting is decreased, since the system is evolving towards an acceptor only system.

QD-GFP nanocomposite was further used as a biosensor to detect a protease activity in a given biological medium. In the context of our biosensing applications we aimed to detect trypsin enzyme, which is known as a kind of protease to digest protein molecules. Because our composite system was composed of a protein-GFP and QD connect via a histag linker, once the linker is digested the interactions would be broken and this would result in the destruction of the FRET facilitating nanocomposite system. This series of events can be tracked by monitoring the change in the lifetime of the nanocomposite donor species using a time resolved fluorescence spectroscopy. Upon addition of the trypsin with varying concentrations one can monitor the decrease in the lifetime of the acceptor molecules which was previously enhanced by the FRET process.

Figs. 5.2.17 and 5.2.18 show the effect of the enzyme on the energy transfer among the GFP-QD system. As comparing with the bare lifetime of the GFP, due to the energy transfer, the lifetime of the GFP increases in the presence of the donor QDs. After this point, we introduce enzyme to the solution with a known concentration in a controlled way as to separate the QD-GFP complex. The experiment is followed in a tedious way activating the enzyme at 37°C and allowing enough time for the enzymatic activity to take place. As changing the enzyme concentration in solution, we observe that the lifetime of the QD-GFP complex follows a trend of decreasing back to the initial GFP lifetime. This enables us to use the enzymatic activity to control the distance among the donor-acceptor pair and thus control the FRET efficiency.

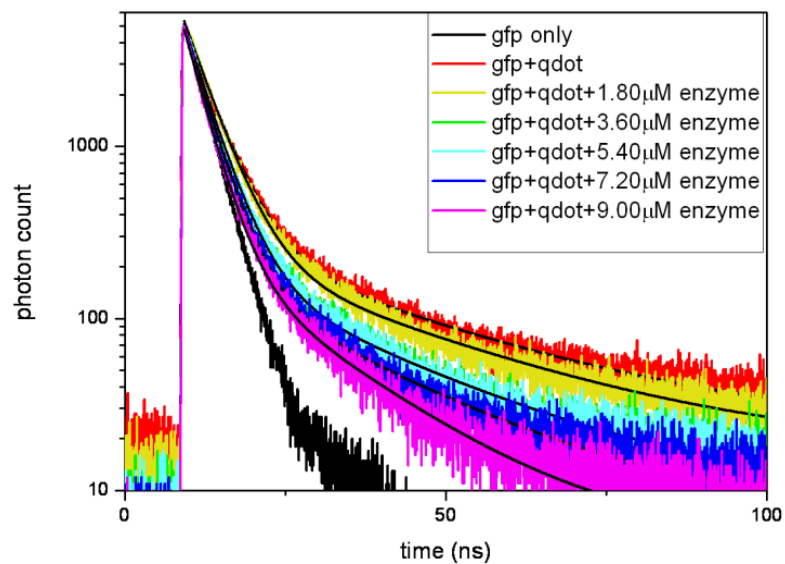


Figure 5.2.17 Room temperature photoluminescence decays of the GFP only, GFP after FRET, and GFP after FRET with controlled enzyme (activated) addition.

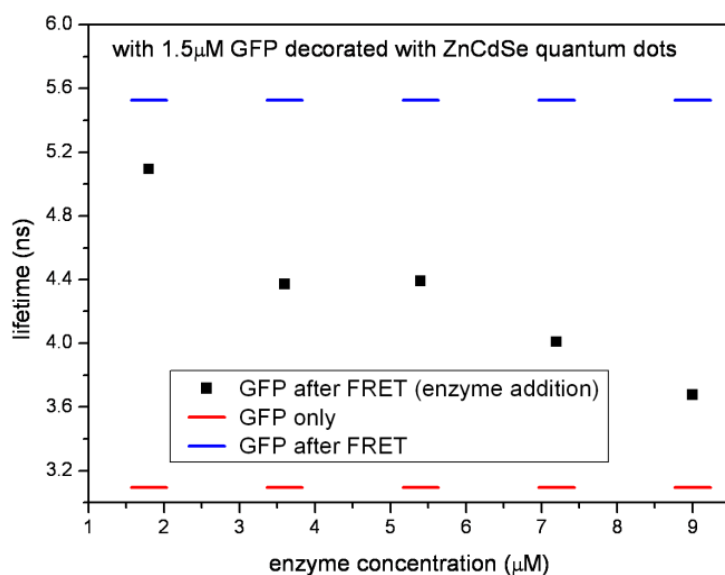


Figure 5.2.18 Lifetime modifications of the GFP only, GFP after FRET, and GFP after FRET with enzyme (activated) addition.

In the control experiments, where we do not activate the enzyme but mix them with the QD-GFP complex (Fig. 5.2.19 and Fig. 5.2.20), we do not observe a significant change, but fluctuations in the photoluminescence decays of the QD-GFP complex. The control experiments are followed in the same manner except for the heat treatment.

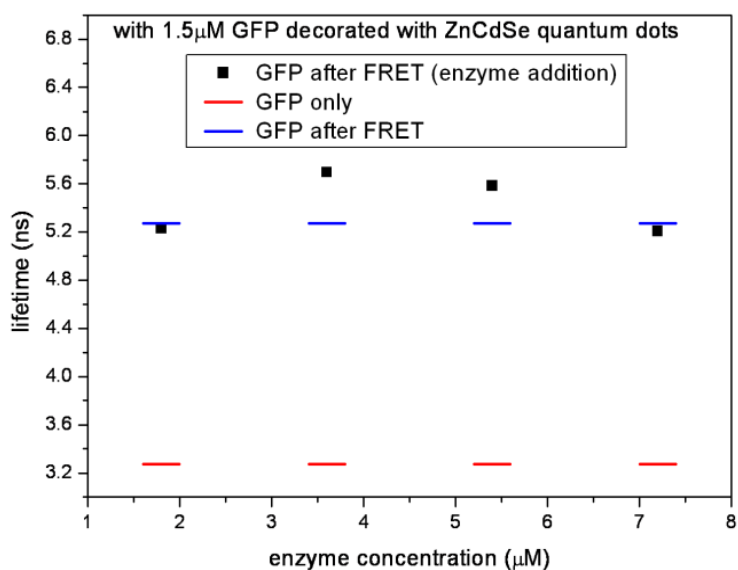


Figure 5.2.19 Lifetime modifications of the GFP only, GFP after FRET, and GFP after FRET with enzyme (unactivated) addition.

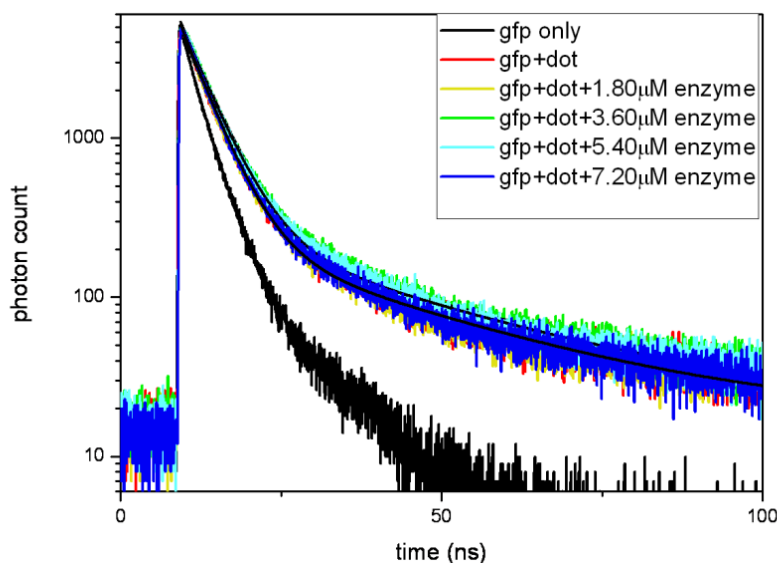


Figure 5.2.20 Room temperature photoluminescence decays of the GFP only, GFP after FRET, and GFP after FRET with enzyme (unactivated) addition.

5.3 Summary

In summary, in this chapter we have shown the composite structures of GFP-QD complexes. The FRET mediated light harvesting results in up to 15 fold enhancement in the emission of the acceptor protein. The lifetime modifications of the donor and acceptor pair has been demonstrated with the theoretical analysis based on dipole-dipole interaction. Furthermore, the trypsin enzyme is implemented for controlling the energy transfer, breaking the bond in between the dot and protein, among the donor-acceptor pairs, as a new potential tool sensing protease activity.

Chapter 6

Excitonic energy transfer from charged quantum dots to organic dye molecules

This chapter is based in part on the publication “Highly efficient nonradiative energy transfer using charged CdSe/ZnS nanocrystals for light harvesting in solution,” Evren Mutlugün, Sedat Nizamoğlu, and Hilmi Volkan Demir, *Applied Physics Letters* 95, 033106 (2009). Reproduced (or ‘Reproduced in part’) with permission from American Institute of Physics. Copyright 2009 American Institute of Physics.

6.1 Introduction

In this chapter we present highly efficient nonradiative Förster resonance energy transfer (FRET) facilitated by the use of positively-charged CdSe/ZnS core-shell nanocrystal quantum dots (QDs) for light harvesting in solution. With rhodamine B (RhB) dye molecules used as the acceptors, our time-resolved photoluminescence measurements show substantial lifetime modifications of these amine-functionalized QD donors from 18.16 to 1.88 ns with FRET efficiencies >90% in solution. These strong modifications allow for light harvesting beyond the absorption spectral range of the acceptor dye molecules. As also has been discussed in Chapter 1, organic dyes are widely used in biolabeling as staining molecules [96,97,98] thanks to their high efficiency and

stability. They are also used in optoelectronics (e.g., dye based lasers [99,100,101]). However, these dye molecules are intrinsically limited in their optical absorption spectral ranges in general. For example, rhodamine B, which is one of the most commonly used dyes, suffers from a characteristically narrow absorption spectrum, typically 450 to 600 nm. Beyond this limited range, it is impossible for RhB to be optically excited efficiently. In various applications, this severely limits the possible spectral range for optically pumping these dyes. For instance, in bioimaging, this prevents the use of dyes in spectral multiplexing, where multiple agents of different colors are used to label different biological targets to be simultaneously excited by a single optical pump [6]. To address these problems, we propose and demonstrate optical excitation of RhB dye molecules in solution based on strong nonradiative Förster resonance energy transfer, enabled with the use of light-harvesting, positively-charged CdSe/ZnS QDs at optical pump wavelengths well below the characteristic absorption spectral range of RhB. This effectively extends the absorption spectral range of RhB acceptor dye molecules in the presence of CdSe/ZnS donor QDs towards shorter wavelengths.

In literature, CdTe based QDs as donors, together with various dyes used as acceptors, have been reported to demonstrate FRET [102,103,104]. Furthermore, CdSe/ZnS QD donors have previously been used for energy transfer to various protein based acceptors [105,106,107]. Additionally, FRET using CdS dots have been investigated [108,109]. In these studies, it has been found that FRET efficiencies are typically not high (below 60%) in solution. CdTe and CdSe/ZnS dots of different sizes have further been studied for energy transfer in film [55,110]. Recently Mayilo *et. al* discussed the use of Ca^{2+} binding to enhance FRET between different sized CdTe nanocrystals in solution [111]. These reports have thus far shown different flavors of semiconductor nanocrystals employed for energy transfer to fluorescent molecules. However, the use of electrostatic interaction between charged QDs and dye molecules in solution for the enhancement of FRET has not been investigated to date. To this

end, the control and tuning of FRET efficiencies and lifetime modifications have also not been studied for electrostatically interacting light-harvesting QD-dye pairs thus far.

6.2 Results and discussion

In this thesis work, using positively-charged amine-functionalized CdSe/ZnS QDs, we present highly efficient FRET-based light harvesting for RhB dye molecules in solution beyond their absorption range, with their FRET efficiencies and lifetime modifications carefully tuned and precisely controlled with QD-dye concentrations. For this purpose, we choose the emission wavelength of our CdSe/ZnS QD donors (around 541 nm) to match well with the absorption range of RhB dye acceptors, while these donor QDs provide a very broad absorption band extending towards short wavelengths (with an absorption band edge of 520 nm).

We find out that the pH of acceptor RhB dyes in aqueous solutions becomes slightly acidic (varying from 6.7 to 6.2) as the concentration of RhB is increased (in the μM range for our experiments). Relying on this observation, to help the donor and acceptor molecules find each other and thus get in close proximity in the solution, especially at lower concentrations, we employ amine-functionalized nanocrystals that are positively charged. These nanocrystals electrostatically interact with the RhB acceptor molecules that are slightly negatively charged in the acidic solution. We experimentally demonstrate significant lifetime modifications of these QDs from 18.16 to 1.88 ns with FRET efficiencies of $>90\%$ in solution. By repeating the same experiments using neutral non-functionalized CdSe/ZnS QDs, we show the effect of donor QD charge on the efficiency of FRET as a function of the acceptor to donor (A/D) concentration ratio.

Fig. 6.2.1(a) presents the time-resolved photoluminescence (TRPL) of amine-functionalized CdSe/ZnS nanocrystal donors (**AF/NC-Ds**) together with RhB acceptors (**RhB-As**) at the donor emission wavelength (541 nm), parameterized with respect to the varied acceptor to donor (A/D) concentration ratio (shown in the figure legend). In this set of experiments, as both the donor nanocrystals and the acceptor dyes are water-soluble, the acceptor molecules are carefully added to the initially prepared aqueous donor solution in controlled increments. These TRPL measurements are taken at room temperature with PicoQuant 200 Fluor Time time-resolved spectroscopy system using an excitation laser source at a pump wavelength of 375 nm. The photon decay lifetimes are calculated by the software package of PicoQuant (FluoFit) using exponential fittings with χ^2 error close to unity. In these TRPL experiments, we observe that the intensity weighted lifetime τ_i of **AF/NC-Ds** is decreased from 18.16 ns to 1.88 ns as the concentration of RhB acceptors (thus, the A/D ratio) is increased. These significant modifications observed in the donor photon lifetimes are attributed to the nonradiative energy transfer enhancing in increments from the donor molecules to the acceptor molecules with the incrementally increasing A/D ratio.

Fig. 6.2.1(b) depicts the decay curves of the same TRPL experiments of Figs. 6.2.1(a) at the same A/D ratios, the only difference being the use of non-functionalized CdSe/ZnS nanocrystal donors (**NF/NC-Ds**) in the solution. In this set of TRPL experiments, we observe the same trend of modifications in emission kinetics of the donor QDs similar to the previous set. As a result of FRET, the donor photon lifetime is decreased in the presence of acceptors. Here it is important to note that ZnS shells that surround CdSe cores and serve as a potential barrier in our nanocrystal structure provides full electronic isolation and prevents tunneling of the confined electron and hole wavefunctions. Therefore, this modification observed in emission kinetics cannot be due to Dexter-type charge transfer.

We also investigate the steady-state photoluminescence (SSPL) of RhB dyes in the presence of amine-functionalized CdSe/ZnS nanocrystals (**AF/NC-Ds + RhB-As**) and of non-functionalized CdSe/ZnS nanocrystals (**NF/NC-Ds + RhB-As**) as a function of A/D ratio, using Cary 100 Fluorometer at a fixed excitation wavelength of 375 nm, the same as that of the excitation source used in TRPL experiments. For each type of QDs, these SSPL experiments are carried over a set of thirty-one samples with varying A/D ratios. For (**AF/NC-Ds + RhB-As**) and (**NF/NC-Ds + RhB-As**), Figs. 6.2.1(c) and 6.2.1(d) show the respective evolution of the photoluminescence spectra of the donor and acceptor molecules changing their A/D concentration ratio in solution. As a result of FRET, we observe that the donor emission is quenched and the acceptor emission is enhanced incrementally as the acceptor-to-donor concentration ratio is increased.

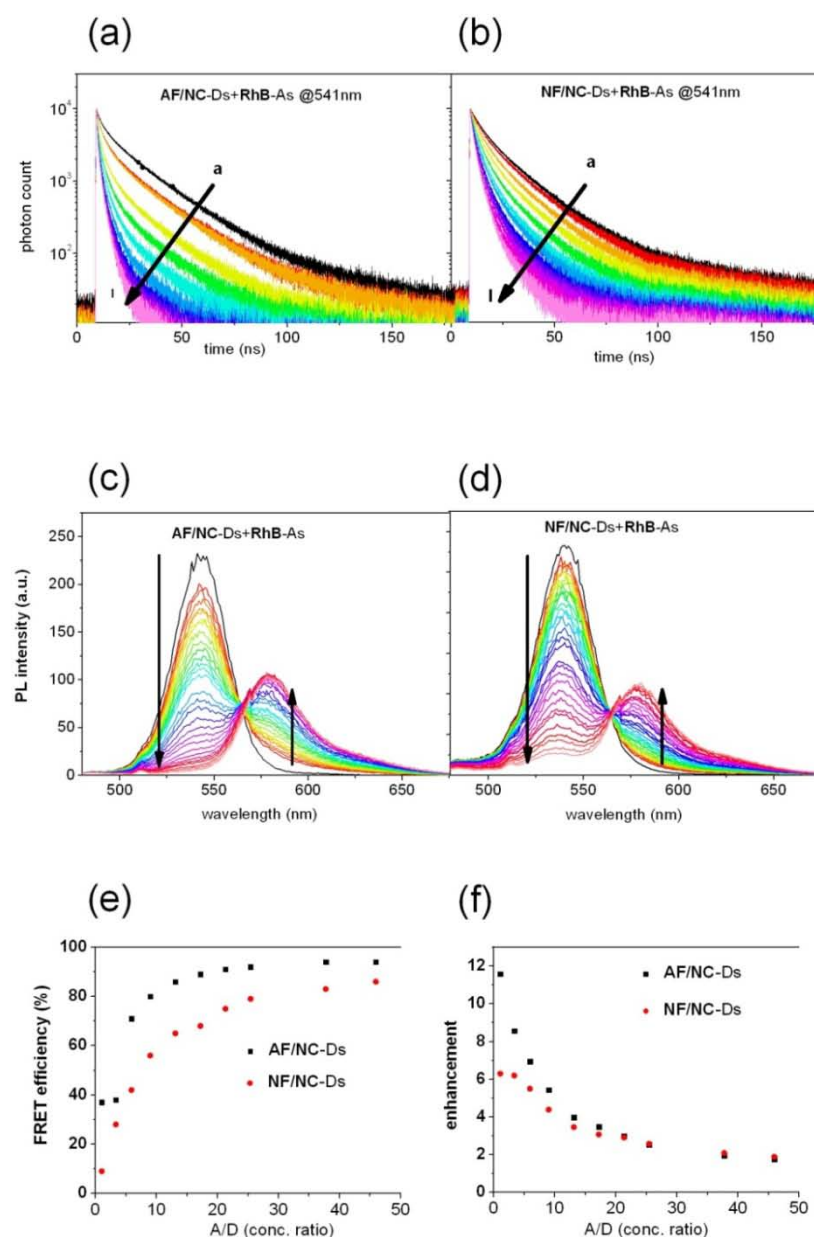


Figure 6.2.1 Room-temperature time-resolved photoluminescence (TRPL) of amine-functionalized CdSe/ZnS nanocrystal donors (AF/NC-Ds) together with RhB acceptors (RhB-As) (a) at the donor emission wavelength (at 541 nm) and (b) TRPL of non-functionalized CdSe/ZnS nanocrystal donors (NF/NC-Ds) together with RhB acceptors (RhB-As) at 541 nm. Room-temperature steady-state photoluminescence (SSPL) of (c) AF/NC-Ds + RhB-As and (d) NF/NC-Ds + RhB-As. All of the TRPL and SSPL measurements are presented as parameterized with respect to the varied concentration ratios of A/D. (e) FRET efficiency levels (extracted from TRPL) and (f) enhancement factor of acceptor emission with respect to the case of acceptors alone (with no donors), both as a function of A/D ratios.

Table 6.2.1 summarizes the results of the time-resolved spectroscopy analyses including the donor photon lifetimes along with their χ^2 error and the FRET efficiencies calculated from TRPL. Table 6.2.1 also presents the experimentally-measured quantum yields of our amine-functionalized and non-functionalized CdSe/ZnS QDs in solution as well as the theoretically-calculated Förster radii of these QD donors for RhB acceptors. Here the Förster radius, R_0 , the distance at which FRET is halved, is calculated using Eqn. 3.2.2 and, The FRET efficiency level is calculated from TRPL using Eqn. 3.2.3. The quantum yield of AF/NC-Ds is measured to be 29.5% whereas that of NF/NC-Ds is found to be 33.0%. Both of them have a calculated Förster radius of ca. 0.56 nm.

L A B E L	Concentration ratio	Using amine-functionalized donors			Using non-functionalized donors		
		Quantum yield	Förster radius		Quantum yield	Förster radius	
		29.5%	5.6 nm		33.5%	5.6 nm	
		Lifetime analysis			Lifetime analysis		
	A/D	τ_i	χ^2	η_{FRET}	τ_i	χ^2	η_{FRET}
a	0.00	18.16	1.09	-	16.65	1.08	-
b	1.03	15.79	1.15	37	15.83	1.08	9
c	3.34	15.44	1.14	38	13.97	1.15	28
d	5.90	11.49	1.22	71	12.29	1.22	42
e	8.98	8.94	1.24	80	10.45	1.26	56
f	13.09	6.32	1.31	86	8.67	1.28	65
g	17.20	3.99	1.27	89	7.88	1.31	68
h	21.30	2.87	1.26	91	6.47	1.38	75
i	25.41	2.51	1.25	92	5.88	1.39	79
j	29.52	2.13	1.23	93	5.13	1.26	79
k	37.73	1.94	1.14	94	4.52	1.32	83
l	45.94	1.88	1.20	94	3.82	1.32	86

Table 6.2.1 List of quantum yields, Förster radii, average decay lifetimes and their χ^2 error limits at the donor emission wavelength, and FRET efficiencies, all for different concentration ratios of A/D when using amine- and non-functionalized CdSe/ZnS nanocrystal donors. All experiments were conducted at room temperature here.

The analysis of TRPL experiments shows that the efficiency level of FRET from the QD donors to the dye acceptors is increased from 37% to 94% when using positively charged amine-functionalized QDs and from 9% to 86% when using neutral non-functionalized QDs, as the A/D concentration ratio is increased, as presented in Table 6.2.1 and depicted in Fig. 6.2.1(e). This shows the same trend of increasing FRET efficiency level with the increased A/D. In Fig. 6.2.1(e), we observe that the amine-functionalized donors converge to a higher level of FRET efficiency faster than the non-functionalized donors do. These analyses suggest that **AF/NC**-Ds tend to exhibit higher efficiency (>90%) in light harvesting for **RhB**-As than **NF/NC**-Ds (although **NF/NC**-Ds possess a slightly higher quantum yield). This enhanced performance of **AF/NC**-Ds in light-harvesting is attributed to the electrostatic interaction between **AF/NC**-Ds and **RhB**-As in solution that possibly keeps them in closer proximity. The Brownian motion of the donor and acceptor molecules in the aqueous medium is also considered to affect FRET in solution at room temperature to some extent, especially for the case of **NF/NC**-Ds; it is otherwise less likely for these to be in close proximity to the acceptor molecules in the solution, given their low concentration levels. Also, in the case of using **AF/NC**-Ds, the screening effects are considered to partially prevent close electrostatic interaction and thus reduce FRET to some extent. Yet, with all other factors in play, we find out that the net effect of the charge of the donor QDs is towards improving Förster resonance energy transfer to the acceptor RhB.

To verify the enhanced emission of the acceptor molecules at the specified pump wavelength (375 nm) we perform SSPL measurement of RhB in the absence of the donor QDs, using exactly the same set of RhB concentrations as in the previous experiments. Fig. 6.2.1(f) shows the enhancement factor calculated for the acceptor dye emission in the presence of **AF/NC**-Ds or **NF/NC**-Ds with respect to the case of the acceptor dyes alone. The enhancement factor is found to be larger for **AF/NC**-Ds than **NF/NC**-Ds at low A/D concentrations, which is once again attributed to the electrostatic interactions in the case of (**AF/NC**-Ds +

RhB-As). As the acceptor amount in solution is increased, the enhancement decreases (despite increasing FRET efficiency) because the donor-acceptor system is evolving towards the case where there are effectively fewer and fewer donor molecules per acceptor molecule, thus converging towards the case of the dyes alone. On the other hand, increasing the overall emission of the acceptor molecules is not feasible at reduced A/D levels since the total emission intensity of the acceptors is low in diluted solutions. Given this trade-off, we find out that there is a good operating point for the A/D concentration ratio (around 10) in the case of **AF/NC-Ds** where a relatively high total emission can be obtained from the acceptor dyes with a good enhancement factor of >4 . Far beyond this point, adding more and more acceptor molecules into the solution provides a diminishing enhancement of the acceptor emissions.

6.3 Summary

In summary, we demonstrated highly efficient FRET-based light-harvesting of positively-charged CdSe/ZnS core-shell nanocrystals to rhodamine B dye molecules in solution by utilizing the electrostatic interaction between them. This proof-of-concept demonstration has led to light-harvesting with FRET efficiency levels of >90%.

Chapter 7

Excitonic energy transfer from water soluble quantum dots to organic dye molecules

This chapter is based in part on the publication “Highly efficient nonradiative energy transfer mediated light harvesting in water using aqueous CdTe quantum dot antennas,” Evren Mutlugün, Olga Samarskaya, Tuncay Ozel, Neslihan Cicek, Nikolai Gaponik, Alexander Eychmüller, and Hilmi Volkan Demir, *Optic Express* 18, 10720-10730 (2010). Reproduced (or ‘Reproduced in part’) with permission from Optical Society of America. Copyright 2010 Optical Society of America.

7.1 Introduction

In this chapter, we present light harvesting of aqueous colloidal QDs to nonradiatively transfer their excitonic excitation energy efficiently to dye molecules in water without requiring ligand exchange. These as-synthesized CdTe QDs used as donors to serve as light-harvesting antennas are carefully optimized to energetically match the electronic structure of Rhodamine B molecules used as acceptors for light harvesting in aqueous medium. By varying the acceptor to donor concentration ratio, we measure the light harvesting factor with substantial lifetime modifications of these water-soluble QDs, from 25.3 to 7.2 ns as a result of their energy transfer with efficiency levels up to 86%.

Not only for the bio-related applications discussed in previous chapters, but also the spectral extension of the organic dyes’ optical absorption is important in

photovoltaic applications where dyes are used as sensitizers [112]. The dye sensitized solar cells require a wide spectral response for an enhanced efficiency, but broadening of the absorption spectra of dyes generally necessitates complicated chemical modifications [113].

To address the limiting characteristic properties of the organic dyes, by using semiconductor QD nanocrystals, nonradiative Förster-type resonance energy transfer can be employed to enable light harvesting at optical wavelengths beyond the absorption range of dye molecules, and thus to effectively extend their absorption. Such nanocrystals feature high-efficiency, Gaussian-like distributed emission along with high tunability of absorption/emission characteristics, which make them good candidates as donors for light harvesting, as we have shown in our previous work [114]. However, the solubility of such donor QDs in aqueous media is a critical issue to provide biocompatibility and enable biological applications [115]. To be dissolved in water, the ligand exchange of nanocrystals is an alternative, but this comes at a cost of significantly decreased quantum efficiency [35]. On the other hand, aqueous CdTe QDs provide as-synthesized water solubility and high quantum yield [74], and their synthesis has already been studied and well established [74, 75]. For these reasons, aqueous CdTe is one of the best candidates as light-harvesting antenna in water. However, such light-harvesting as-synthesized aqueous QDs have not been investigated or demonstrated for light harvesting in water to date, although this is of critical importance for spectrally extended bioimaging and biolabeling applications.

Nonradiative transfer of the electronic excitation energy from electronically excited donor molecules to optically luminescent acceptor molecules in close proximity was first discussed by Theodor Förster in 1948 [116]. Till date FRET has been extensively studied in different FRET pairs of dyes and nanocrystals for various applications [106,108,109,117,118] (also including CdTe nanocrystals [103,104,107,119]). Although these previous reports have

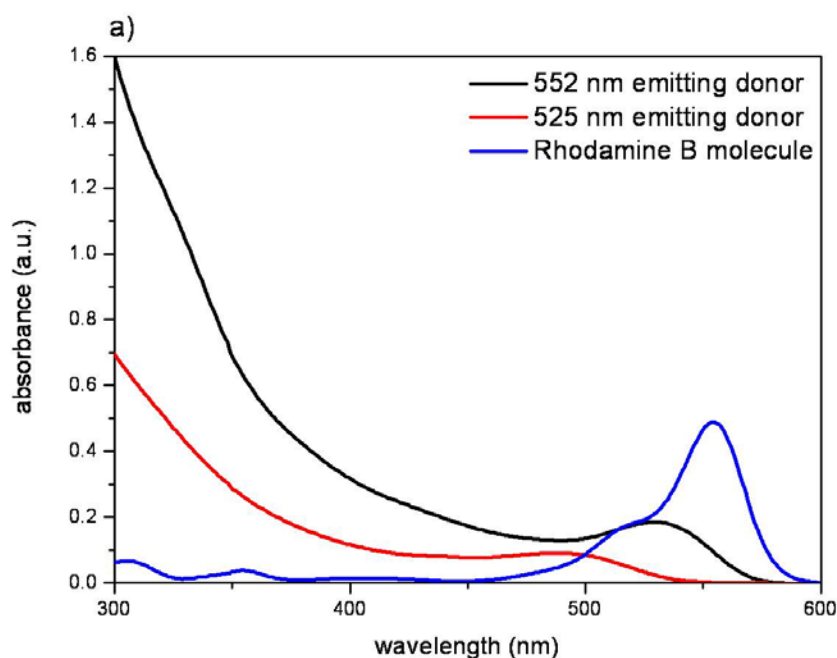
demonstrated FRET mechanism using such a large variety of FRET pairs, light harvesting based on FRET using aqueous nanocrystals has not been reported. In the previous work of our group, light harvesting of organic nanocrystals synthesized in apolar solvents was investigated; this, however, undesirably came at the cost of requiring ligand exchange. Avoiding the need for the ligand exchange, the light harvesting factor of as-synthesized aqueous nanocrystals and their systematic tuning and control in aqueous medium for light harvesting have not been studied.

In this chapter, different than the prior works of our group and the others, we propose and demonstrate light harvesting of aqueous colloidal CdTe QDs to nonradiatively transfer their excitonic excitation energy efficiently to dye molecules in water, and present systematic tuning and control of their light harvesting activity in aqueous medium, without the need for ligand exchange. We investigated the effects of Förster radius of these aqueous nanocrystals on modifying their lifetimes and controlling their light harvesting factor in water. We studied the operation of these CdTe nanocrystal donors, serving as optical antennas for acceptor Rhodamine B molecules, with their steady state photoluminescence spectroscopy and further investigated and analyzed their significantly modified photoluminescence decay kinetics for light harvesting with their time resolved photoluminescence spectroscopy. With acceptor-to-donor concentration ratio varied in water, we controlled the light harvesting factor of the donor CdTe QDs, with their substantial lifetime modifications as a result of the nonradiative energy transfer with high efficiency levels (up to 86%). We further analyzed the controlled change in the lifetime of the acceptor molecules and investigated the resulting trend of increasing energy transfer efficiency versus decreasing light harvesting enhancement of the acceptor emission with the increased A/D concentration ratio, discussing the fundamental tradeoffs and practical feasibility of FRET assisted light harvesting operation with reasonable efficiency and enhancement.

7.2 Results and discussion

In this work we colloidally synthesized aqueous CdTe QDs in two different sizes to study the effect of Förster radius on the energy transfer efficiency and light harvesting activity. Our synthesis procedure follows the method previously described in Chapter 2.2.1.1.

Fig. 7.2.1a shows the optical absorption spectra of these differently sized CdTe QD donors carefully chosen by size selection, along with that of Rhodamine B acceptor molecules in water. Fig. 7.2.1b depicts the photoluminescence spectra of these CdTe QDs selectively chosen to emit at the peak emission wavelengths of 525 and 552 nm (corresponding to 2.04 and 2.98 nm in size, respectively), presented here along with the emission and absorption spectra of the acceptor dye molecules alone to show the spectral overlap. Here the absorbance measurements were taken using Cary UV-VIS spectrophotometer and the photoluminescence measurements were carried out using Cary Eclipse fluorescence spectrophotometer.



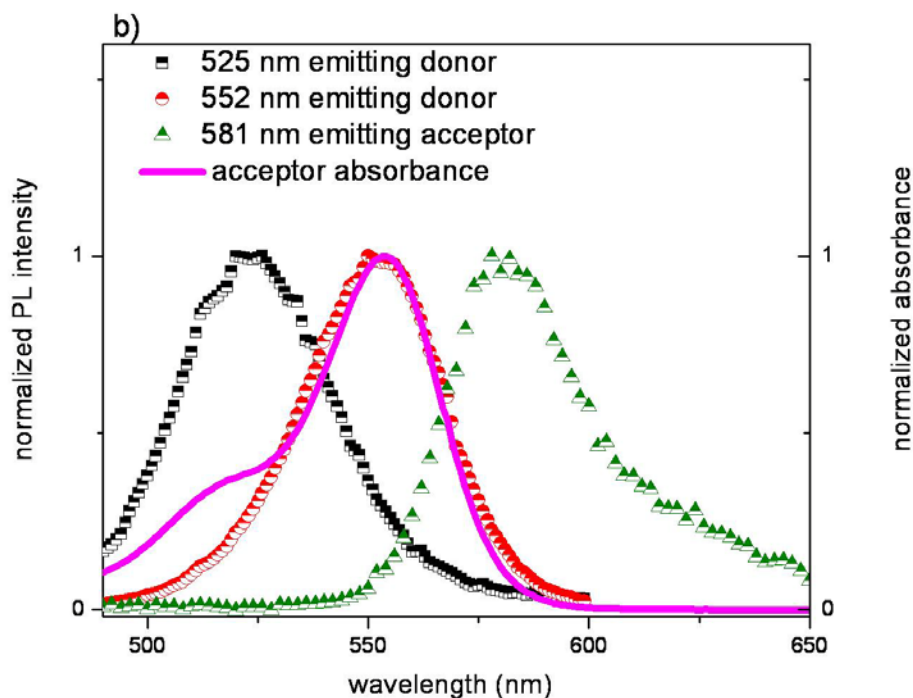


Figure 7.2.2 Room temperature absorbance spectra of the two differently sized aqueous CdTe nanocrystal QDs (emitting at 552 and 525 nm) together with that of the Rhodamine B dye molecules. (b) Normalized room temperature photoluminescence spectra of our aqueous CdTe QDs (donors) selectively chosen to emit at the peak wavelengths of 525 and 552 nm, along with the emission and absorption spectra of the Rhodamine B molecules (acceptors). The donors emitting at 552 nm provide a better spectral match to the electronic structure of these acceptors.

Fig. 7.2.1b is used to calculate the spectral overlap integrals $J(\lambda)$, which leads to 5.5×10^{15} and 9.2×10^{15} for the donor QDs emitting at 525 and 552 nm, respectively. Subsequently, the quantum efficiencies of the donor molecules are experimentally measured to be 10% for 525 nm emitting and 54% for 552 nm emitting dots, using Rhodamine 6G as the reference dye. This increase in the quantum efficiency is commonly observed for this type of nanocrystals with increasing size. Using Eqn. 4.2.2, the Förster radii calculated are $R_o = 4.7$ nm

for 525 nm QDs and $R_o = 6.7$ nm for 552 nm QDs. Based on this observation, the QD donors emitting at 552 nm are found to be a better optimized match to the acceptor dyes, compared to 525 nm emitting dots.

To observe FRET, we first performed SSPL measurements (with optical excitation at 375 nm) while adding controlled amounts of acceptor molecules into the aqueous donor solution, thus changing A/D ratio in increments. Fig. 7.2.2a presents SSPL spectra for our CdTe QDs emitting at 552 nm used as the donors and Fig. 7.2.2b shows the results of the same measurements repeated using 525 nm emitting dots as the donors, both starting with the same concentration levels and changing A/D concentration ratio in an identical manner in water. In this steady state characterization, optical excitation is chosen at 375 nm to be consistent with that of the time resolved measurements that use a 375 nm laser diode pump. It is worth noting that our donor molecules are optically well excited at 375 nm, while this excitation wavelength is out of the absorption range of the acceptor molecules (Fig. 7.2.1a). Here the concentrations of the donors (without acceptors) and the acceptors (without donors) used in Fig. 7.2.1a correspond to the same starting points of Fig. 7.2.2 before adding the acceptor molecules into the aqueous donor solution. As A/D concentration ratio is increased, we clearly observe simultaneously the quenching of donor emission and the enhancement of acceptor emission in increments.

To better understand the emission kinetics, we also performed and analyzed TRPL measurements, again by adding controlled amounts of acceptors into the aqueous donor solution (and changing A/D concentration ratios) in identical increments, both for 552 and 525 nm QD donors. TRPL measurements were conducted using PicoQuant FluoTime 200 time resolved spectroscopy system with a fixed laser diode head at 375 nm wavelength having pulse widths of <70 ps. Fig. 7.2.3 shows the evolution of photon count decay over time, parameterized with respect to the varied A/D concentration ratios, using 552 nm emitting QDs (given in Fig. 7.2.3a) and 525 nm emitting ones (given in Fig.

7.2.3b) at the corresponding donor emission wavelengths. Each decay curve is also shown together with its corresponding numerical triple exponential fits, which exhibit good fitting to the experimental data. These measurements and numerical analyses are performed at the corresponding peak emission wavelengths of the donor nanocrystals since there is an insignificant overlap between the donor and acceptor emission spectra at these peak wavelengths (Fig. 7.2.1b), which makes the analysis safe (with no detectable crosstalk between the emission of donor and acceptor molecules). The comparison of their donor photoluminescence decay lifetimes is also presented as a function of A/D concentration ratio in Fig. 7.2.3c. Here we clearly observe increasingly faster photoluminescence decay of the donors. We also see that the donor lifetimes diverge away more from the starting baseline of only donors and are shortened further more for 552 nm emitting QDs (with its lifetimes modified from 25.3 to 7.2 ns) than those of 525 nm dots (with its lifetimes modified from 20.4 to 7.1 ns). This is because 552 nm emitting CdTe QDs are better optimized to match Rhodamine dye molecules and thus serve as better light-harvesting antennas to these dyes.

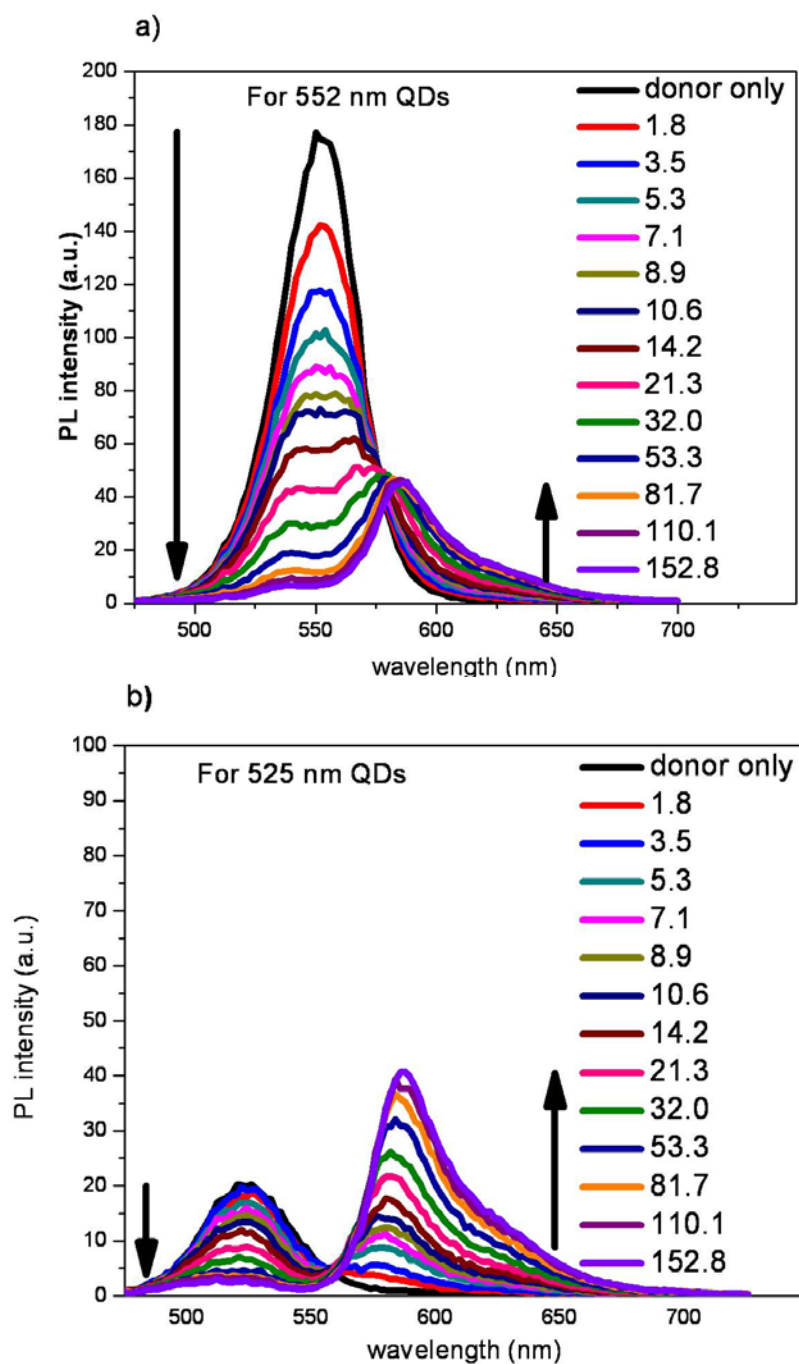
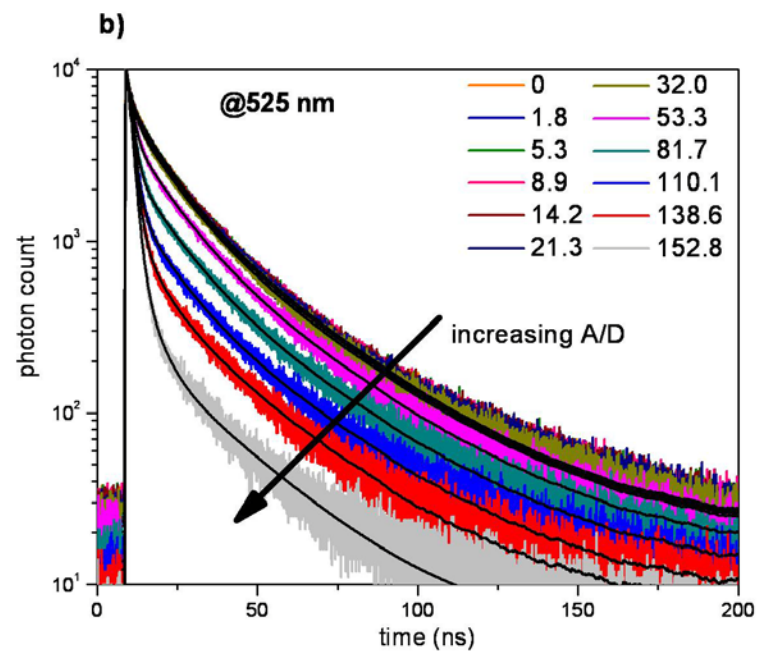
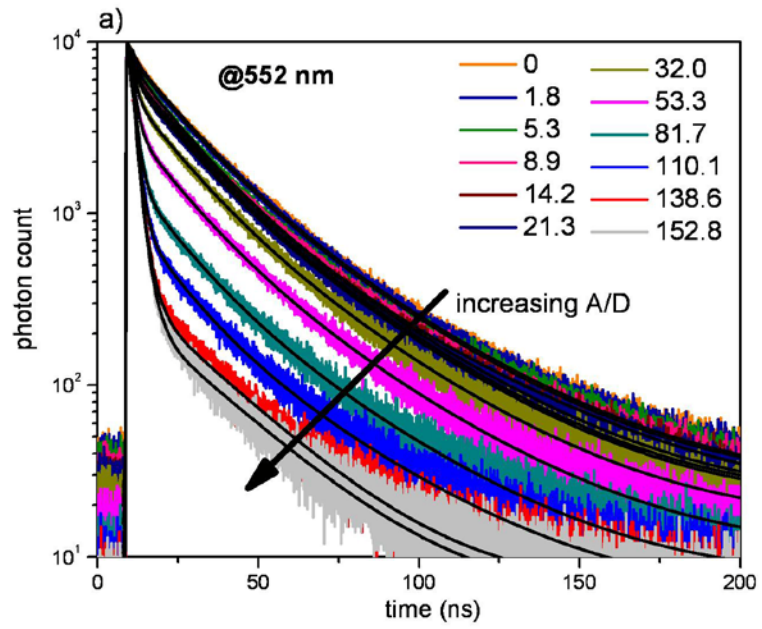


Figure 7.2.3 SSPL spectra taken at room temperature by adding controlled amounts of dye acceptors into the aqueous donor solution using CdTe QDs emitting at the peak wavelength of (a) 552 nm and (b) 525 nm. The legends show the corresponding A/D concentration ratios (A/D=1.8–152.8). (Note that these PL intensity levels are measured using the same arbitrary units and that they are presented using the scales as indicated on their plots, for clear visibility.)



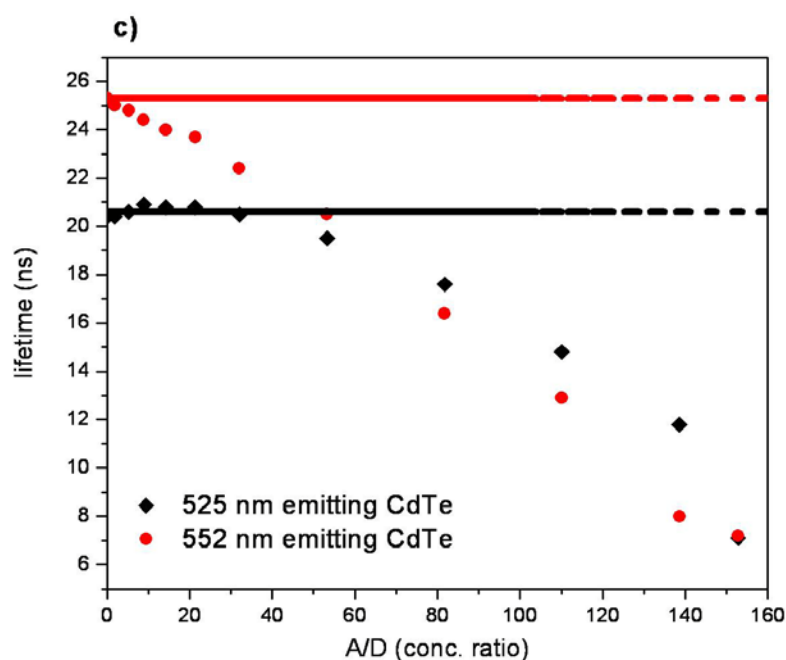


Figure 7.2.4 TRPL measurements of donor molecules taken at room temperature by adding controlled amounts of dye acceptors into the aqueous donor solution, using CdTe QDs emitting at the peak wavelength of (a) 552 nm and (b) 525 nm, all shown together with their corresponding numerical fits, and along with a comparative analysis of the donor photoluminescence decay lifetimes both for 552 and 525 nm emitting dots as a function of A/D concentration ratio (c). In the last plot, the red (black) dotted baseline represents the lifetime of only donors of 552 nm (525 nm) emitting dots, without any acceptors in the mixture.

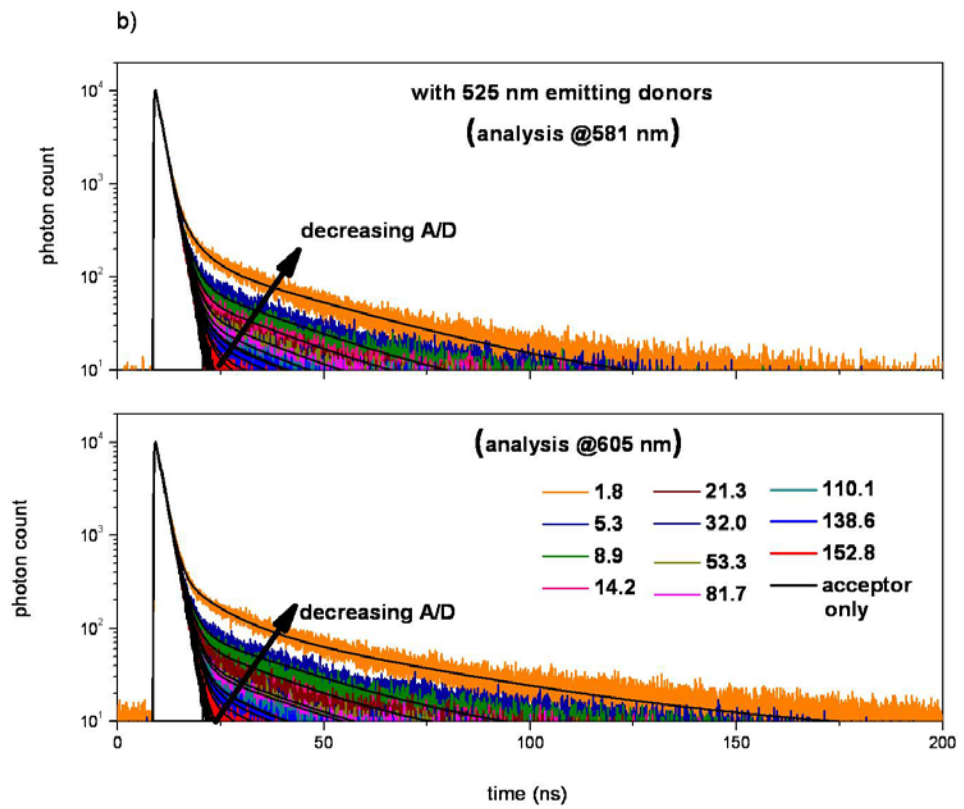
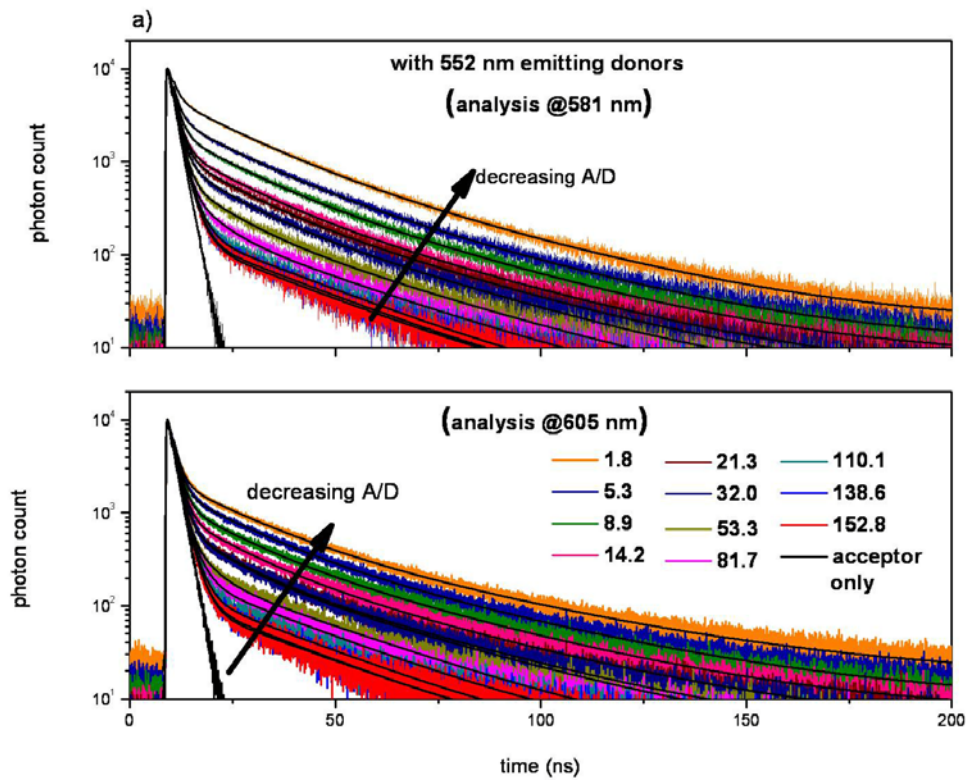
Furthermore, we also performed TRPL characterization and analyses at the acceptor emission wavelengths. The peak emission wavelength of the acceptor is 581 nm, where there is a weak tail component of the donor emission. Therefore, in addition to the peak wavelength 581 nm, we performed all of the measurements and lifetime analyses also at 605 nm where there is no detectable donor emission, for safe comparison. This allowed us to make sure the effect of this tail overlap of the donor at 581 nm is insignificant. The evolution of photon count lifetimes at 581 and 605 nm are given as a function of time together with their numerical fits for 552 nm emitting QDs in Fig. 7.2.4a and for 525 nm emitting QDs in Fig. 7.2.4b. Both of their comparative lifetime analyses are given in Figs 7.2.4c and 7.2.4d. Due to the energy feeding as a result of FRET

process, we see that the acceptor photoluminescence decay lifetimes are increased compared to the baseline of only acceptors, which is consistent with the previous literature [120,121]. Using 552 nm emitting donors, we observe the lifetime of the acceptor molecule increases from 1.68 to 23.24 ns. As a function of the increasing A/D concentration ratio, since the rate of the enhancement on the emission of acceptor molecule decreases for a larger A/D (Fig. 7.2.4c), the modified lifetimes also converge towards the baseline. Regardless of the analyses conducted at either of the wavelengths (581 or 605 nm), we observe the same trend of the acceptor lifetime modifications, again with a stronger modification for the better optimized light-harvesting 552 nm emitting CdTe QDs in these experiments. All of the lifetime analysis results are also listed in Table 7.2.1-7 along with their amplitudes A_i and χ^2 , chi-square values. The intensity weighted lifetime, τ_{int} is calculated using Eqn. 7.2.1

$$\tau_{int} = \frac{\sum_i A_i \tau_i^2}{\sum_i A_i \tau_i} \quad 7.2.1$$

whereas the amplitude wighted lifetime, τ_{amp} is calculated using Eqn. 7.2.2

$$\tau_{amp} = \frac{\sum_i A_i \tau_i}{\sum_i A_i} \quad 7.2.2$$



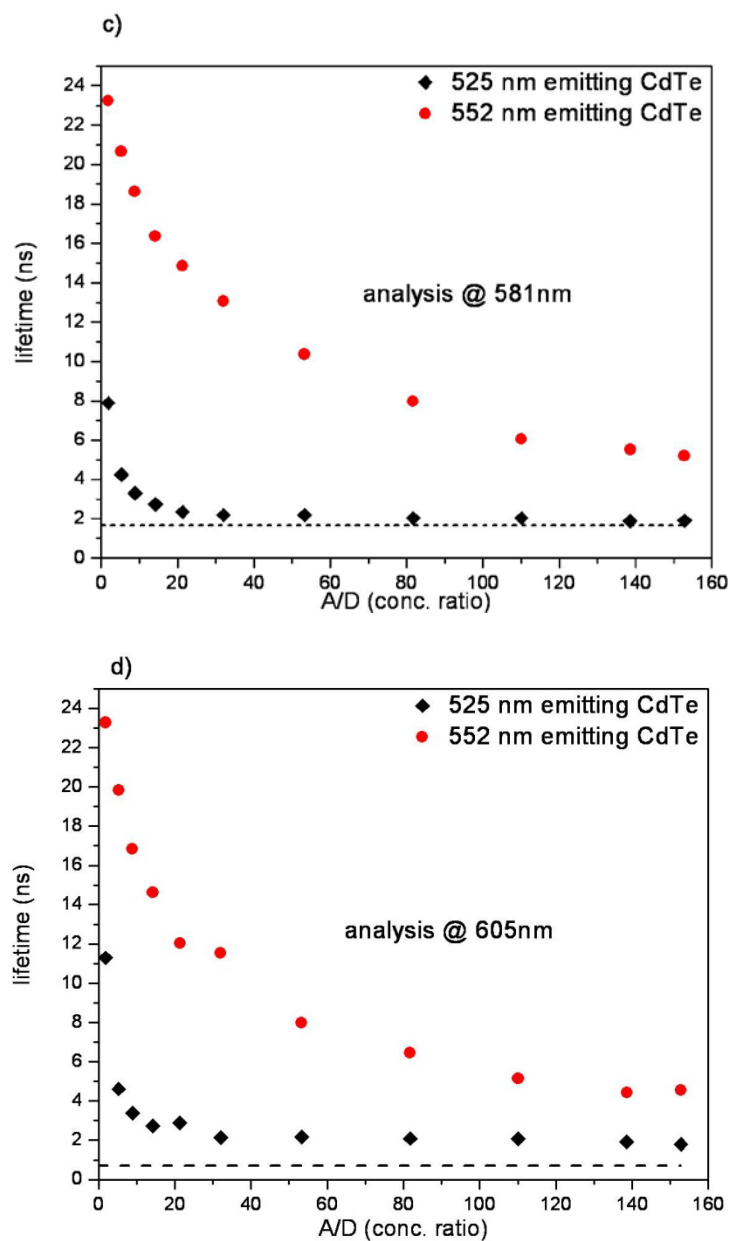


Figure 7.2.5 TRPL measurements of acceptor molecules at room temperature while varying the A/D concentration ratio, shown along with their numerical fits using (a) 552 nm and (b) 525 nm emitting QDs and comparative analysis of the acceptor photoluminescence decay lifetimes for emission (c) at 581 nm (acceptor peak with a weak donor tail) and (d) at 605 nm (strong acceptor tail with no donor tail) as a function of A/D concentration ratios. In both plots (c) and (d), the dashed baseline represents the lifetime of only acceptors without any donors.

TRPL analysis of 525 nm emitting dots at 525 nm with respect to changing A/D										
A/D	A ₁	τ ₁ (ns)	A ₂	τ ₂ (ns)	A ₃	τ ₃ (ns)	τ _{int} (ns)	τ _{amp} (ns)	Eff %	χ ²
0	2341	29.32	4753	10.09	7438	0.84	20.36	8.46	0	1.25
1.8	2334	29.32	4667	9.99	7754	0.80	20.42	8.22	2.80	1.26
5.3	2367	29.52	4631	10.15	7427	0.88	20.63	8.55	~0	1.24
8.9	2357	29.78	4452	10.14	7504	0.91	20.91	8.54	~0	1.22
14.2	2328	29.78	4436	10.23	7513	0.98	20.78	8.55	~0	1.23
21.3	2221	30.08	4212	10.44	7725	1.06	20.82	8.40	0.64	1.21
32.0	2073	30.12	4059	10.65	7618	1.21	20.48	8.35	1.19	1.20
53.3	1541	30.46	3040	10.96	9284	1.37	19.48	6.71	20.65	1.15
81.7	1023	30.70	1985	10.96	11229	1.48	17.59	4.90	42.01	1.20
110.1	720	29.36	1248	9.56	12322	1.51	14.76	3.62	57.22	1.22
138.6	556	27.19	10004	6.93	12980	1.50	11.77	2.85	66.26	1.20
152.8	247	25.69	963	4.77	13079	1.43	7.14	2.07	75.50	1.22

Table 7.2.1 TRPL measurement analysis of the 525 nm emitting donors at 525 nm varying the A/D concentration ratio.

TRPL analysis of 525 nm emitting dots at 581 nm with respect to changing A/D									
A/D	A ₁	τ ₁ (ns)	A ₂	τ ₂ (ns)	A ₃	τ ₃ (ns)	τ _{int} (ns)	χ ²	
1.8	177	31.96	1037	4.33	13648	1.35	7.88	1.20	
5.3	108	25.46	4150	2.34	10953	1.17	4.25	1.11	
8.9	85	22.51	6648	2.05	8545	1.03	3.30	1.09	
14.2	61	21.51	7053	2.02	8142	1.02	2.74	1.03	
21.3	53	18.52	8478	1.92	6934	0.93	2.34	1.18	
32.0	42	18.33	8653	1.92	6712	0.91	2.19	1.14	
53.3	45	17.89	8789	1.90	6729	0.91	2.19	1.16	
81.7	39	16.05	9252	1.88	6092	0.86	2.03	1.19	
110.1	27	18.97	8715	1.92	6689	0.93	2.03	1.20	
138.6	26	15.15	9299	1.90	6109	0.87	1.89	1.15	
152.8	12	24.03	9177	1.86	6236	0.90	1.90	1.36	

Table 7.2.2 TRPL measurement analysis of the 525 nm emitting donors at 581 nm varying the A/D concentration ratio.

TRPL analysis of 525 nm emitting dots at 605 nm with respect to changing A/D								
A/D	A ₁	τ_1 (ns)	A ₂	τ_2 (ns)	A ₃	τ_3 (ns)	τ_{int} (ns)	χ^2
1.8	128	46.63	404	9.03	14116	1.46	11.29	1.16
5.3	117	26.16	5379	2.23	9774	1.07	4.62	1.17
8.9	98	21.87	7350	2.02	7983	0.99	3.39	1.19
14.2	51	23.24	7585	2.00	7815	0.98	2.73	1.07
21.3	57	23.50	7200	2.05	8094	1.02	2.88	1.06
32.0	44	16.98	8977	1.93	6397	0.90	2.15	1.23
53.3	45	17.29	8895	1.90	6614	0.86	2.16	1.22
81.7	38	17.00	9089	1.92	6397	0.88	2.09	1.21
110.1	29	18.90	9230	1.91	6061	0.88	2.07	1.20
138.6	27	15.80	9512	1.89	5789	0.83	1.92	1.25
152.8	13	17.37	9138	1.86	6186	0.88	1.79	1.18

Table 7.2.3 TRPL measurement analysis of the 525 nm emitting donors at 605 nm varying the A/D concentration ratio.

TRPL analysis of 552 nm emitting dots at 552 nm with respect to changing A/D										
A/D	A ₁	τ_1 (ns)	A ₂	τ_2 (ns)	A ₃	T ₃ (ns)	τ_{int} (ns)	τ_{amp} (ns)	Eff. %	χ^2
0	2524	36.75	6271	15.85	4265	1.26	25.26	1.12	0	1.12
1.8	2605	35.90	6016	15.61	4662	1.21	25.02	1.13	3.90	1.13
5.3	1572	41.03	6062	15.95	5216	1.57	24.81	1.17	12.83	1.17
8.9	2151	35.78	4973	15.35	6317	1.27	24.40	1.14	20.63	1.14
14.2	2212	34.70	4567	14.76	6742	1.32	23.99	1.11	25.14	1.11
21.3	2063	34.85	4498	14.92	6827	1.42	23.67	1.12	26.55	1.12
32.0	1561	34.80	3657	14.87	8501	1.46	22.44	1.14	41.63	1.14
53.3	967	35.42	2418	14.83	10387	1.56	20.51	1.13	58.55	1.13
81.7	521	34.78	1201	13.95	12215	1.62	16.38	1.15	74.03	1.15
110.1	320	34.61	720	12.74	13095	1.63	12.86	1.17	80.54	1.17
138.6	348	25.09	3560	2.78	10949	1.33	8.01	1.23	85.23	1.23
152.8	269	25.79	4194	2.65	10499	1.28	7.16	1.15	86.08	1.15

Table 7.2.4. TRPL measurement analysis of the 552 nm emitting donors at 552 nm varying the A/D concentration ratio.

TRPL analysis of 552 nm emitting dots at 581 nm with respect to changing A/D								
A/D	A ₁	τ_1 (ns)	A ₂	τ_2 (ns)	A ₃	τ_3 (ns)	τ_{int} (ns)	χ^2
1.8	1566	35.80	3515	15.18	8940	1.41	23.23	1.12
5.3	1042	34.53	2124	14.24	10977	1.44	20.67	1.10
8.9	774	34.15	1518	13.53	12159	1.46	18.64	1.12
14.2	508	34.86	1080	13.33	12809	1.48	16.38	1.16
21.3	486	32.94	913	12.23	13030	1.50	14.85	1.12
32.0	425	31.51	755	10.77	13304	1.49	13.05	1.14
53.3	278	31.41	543	9.88	13606	1.51	10.36	1.14
81.7	237	28.43	568	6.27	13723	1.48	7.96	1.12
110.1	209	25.08	4409	2.48	10629	1.18	6.05	1.05
138.6	181	24.82	5258	2.32	9634	1.13	5.51	1.06
152.8	167	24.72	4266	2.44	10793	1.19	5.22	1.05

Table 7.2.5 TRPL measurement analysis of the 552 nm emitting donors at 581 nm varying the A/D concentration ratio

TRPL analysis of 552 nm emitting dots at 605 nm with respect to changing A/D								
A/D	A ₁	τ_1 (ns)	A ₂	τ_2 (ns)	A ₃	τ_3 (ns)	τ_{int} (ns)	χ^2
1.8	701	42.56	1591	15.37	11970	1.46	23.28	1.13
5.3	548	40.07	1320	14.82	12481	1.51	19.85	1.11
8.9	478	36.82	971	13.21	13060	1.52	16.85	1.15
14.2	342	37.02	763	13.08	13383	1.53	14.63	1.14
21.3	306	33.70	594	10.39	13481	1.50	12.05	1.14
32.0	300	33.09	596	10.16	13407	1.53	11.55	1.17
53.3	255	27.88	897	4.70	13627	1.43	7.99	1.10
81.7	225	25.53	3185	2.73	11804	1.26	6.47	1.09
110.1	161	24.90	5866	2.28	9180	1.11	5.13	1.05
138.6	134	23.86	6681	2.16	8412	1.04	4.42	1.08
152.8	119	25.71	5840	2.25	9138	1.09	4.55	0.98

Table 7.2.6 TRPL measurement analysis of the 552 nm emitting donors at 605 nm varying the A/D concentration ratio.

TRPL analysis of 581 nm emitting Rhodamine B molecules at 581 nm							
A ₁	τ ₁ (ns)	A ₂	τ ₂ (ns)	A ₃	τ ₃ (ns)	τ _{int} (ns)	χ ²
-17	0.001	8277	1.98	7105	1.006	1.68	1.88
TRPL analysis of 581 nm emitting Rhodamine B molecules at 605 nm							
A ₁	τ ₁ (ns)	A ₂	τ ₂ (ns)	A ₃	τ ₃ (ns)	τ _{int} (ns)	χ ²
10225	1.89	25883	0.53	-22115	0.45	1.69	1.23

Table 7.2.7. TRPL measurement analysis of the 581 nm emitting acceptors at 581 and 605 nm varying the A/D concentration ratio.

Figs 7.2.3 and 7.2.4 demonstrate clearly the effect of Förster radius on the lifetime modifications of the donor and acceptor molecules. For further analysis, we also calculate energy transfer efficiency and light harvesting enhancement of the acceptor emission. The energy transfer efficiency is extracted from the amplitude weighted donor lifetime, τ_{amp} in the presence and absence of the acceptor molecules using Eqn. 7.2.3

$$\eta_{FRET} = 1 - \frac{\tau_{DA}}{\tau_D} \quad 7.2.3$$

Here τ_{DA} is the amplitude weighted lifetime of donors in the presence of acceptors and τ_D is that of donors in the absence of acceptors.

Fig. 7.2.5a reveals the comparison of efficiency levels extracted from TRPL measurements. Here we observe that the energy transfer efficiency increases with the increased A/D concentration ratio, as the donors find more acceptors around them to transfer more of their excitation energy. Tuning the A/D concentration ratios, and using better optimized 552 nm emitting QD donors, we observe a maximum energy transfer efficiency of 86%, which is obtained at an A/D concentration ratio of 152.8 in our experiments. This comparison shows

that the efficiency levels are higher using 552 nm emitting QDs than those of 525 nm emitting ones.

To show the effect of nonradiative energy transfer mediated light harvesting on the emission enhancement of the acceptor molecules, we further compute the light-harvesting factor for the acceptor emission (Fig. 7.2.5b) These calculations are carried out through fitting SSPL measurements (in Fig. 7.2.2) of the donor QDs to a Gaussian distribution and comparing the overall emission (donor+acceptor mixture) with the emission of only acceptors (corresponding to the same concentration of acceptor molecules used in each A/D concentration point). In these calculations, the tail overlap of the donor emission on the acceptor emission is also considered, and any possible contribution from the tail (although weak) is also subtracted. Here we observe that the relative enhancement factor of the acceptor emission is decreased with the increased A/D concentration ratio, because the acceptors increasing in number find fewer donors around them to be fed via nonradiative energy transfer, which indicates a tradeoff between the efficiency and light harvesting factor.

Also, we again observe that 552 nm emitting aqueous CdTe QDs are better light-harvesting antennas in water for Rhodamine B dye molecules in comparison to those QDs emitting at 525 nm. In the light of these experiments and analyses, such light harvesting is possible; however, one needs to consider the tradeoff between the efficiency and the enhancement factor to choose an operating point. These results also indicate that nonradiative energy transfer assisted light harvesting may enable QD multiplexed dye biodetection systems.

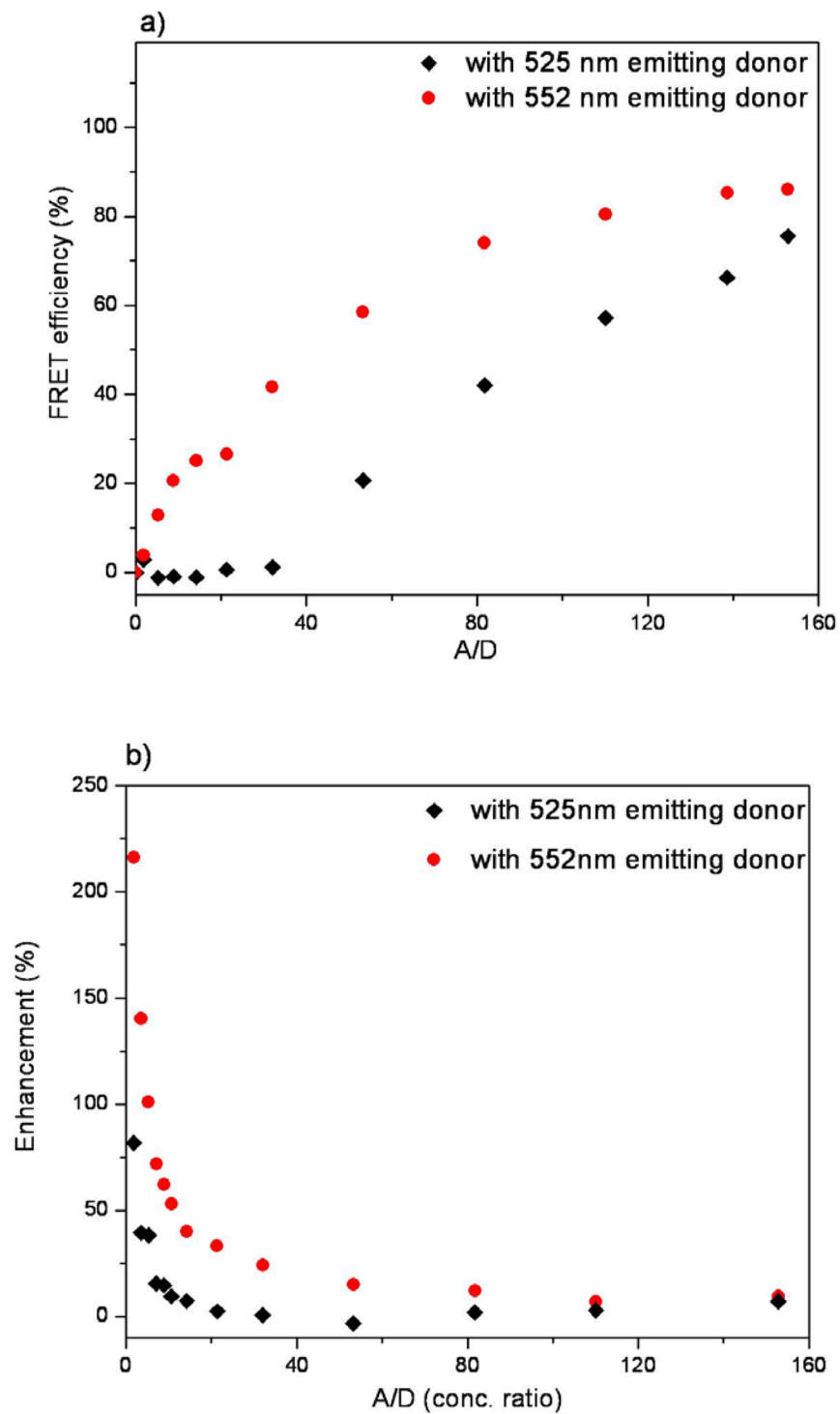


Figure 7.2.6 Comparison of (a) FRET efficiencies and (b) enhancement of the acceptor emission at room temperature, using 552 nm and 525 nm emitting CdTe QD donors, as a function of the A/D concentration ratio.

7.3 Summary

In this chapter, we have presented nonradiative energy transfer based light harvesting of aqueous colloidal CdTe QD antennas for dye molecules in water. Our experiments show that these QDs used as donors need to be carefully optimized to match Rhodamine B used as acceptors. In our experiments, we have observed strong lifetime modifications of these CdTe QDs from 25.3 to 7.2 ns. We have demonstrated the energy transfer efficiency tuning up to 86% as the acceptor-donor concentration ratio is varied. Since there is no additional electrostatic interaction to keep the QD and dye in close proximity, the achieved efficiency levels is smaller than the case with the interaction (Chapter 6). These experiments indicate that nonradiative energy transfer mediated light harvesting using aqueous QDs leads to enhanced emission of dye molecules in water at wavelengths beyond the absorption range of the dyes. One should also note that a good operating point in the A/D concentration ratio for a specific donor-acceptor pair has to be set to provide both reasonably high efficiency and high light harvesting of the acceptor emission.

Chapter 8

Excitonic interactions in very large-area free-standing membranes of colloidal InP/ZnS quantum dots

This chapter is based in part on the paper work of “Very large-area free-standing membranes of colloidal InP/ZnS quantum dots,” Evren Mutlugun, Pedro Ludwig Hernandez Martinez, Yasemin Coskun, Cuneyt Eroglu, Talha Erdem, Vijay K. Sharma, Emre Unal, Subhendu K. Panda, Stephen G. Hickey, Nikolai Gaponik, Alexander Eychmuller, and Hilmi Volkan Demir, in submission (2011).

8.1 Introduction

In this chapter we propose and demonstrate the fabrication of flexible, freestanding membranes of colloidal InP/ZnS QDs (QDs) with fatty acid ligands in very large areas (over $50\text{ cm} \times 50\text{ cm}$), which have been developed for excitonic interactions towards remote phosphor applications for high-temperature light-engines in solid-state lighting. Embedded in poly (methyl methacrylate) matrix, while the formation of stand-alone films using those QDs commonly capped with TOPO and oleic acid is not possible, the ligand myristic acid employed for the synthesis of these QDs imparts a strong hydrophobic character to the thin film and enables easy peel-off and membrane formation even in large areas, thereby avoiding the need for a ligand exchange. When

hybridized with a blue LED, these Cd-free QD membranes allow for high color-rendering, warm white light generation (with a CRI ~90 and a CCT <3500 K). In the membrane, the temperature-dependent emission kinetics and energy transfer dynamics among different-sized InP/ZnS QDs are studied. High energy transfer efficiency (up to 80%) and strong donor lifetime modification (from 18 to 4 ns) are achieved. The suppression of the nonradiative channels is observed when the membrane is cooled to cryogenic temperatures. The changes in the experimental lifetime of the donor and acceptor InP/ZnS QDs as a result of the excitonic energy transfer are in excellent agreement with our theoretical model based on the exciton-exciton interaction among the membrane dots. The ability to make such very large-area, flexible, freestanding Cd-free QD membranes paves the way for environmental friendly phosphor applications including flexible, surface-emitting light-engines using point-source inorganic LEDs.

In the past few decades the colloidal QDs have gained substantial interest for innovative applications including those in solid state lighting [122,123]. The demand for QD particles arises as a result of their unique optical and electronic properties. The band gap engineering, by choosing the size and composition of the particles, has made semiconductor QDs very versatile in various applications [14,124]. From an application point of view, the use of these QDs is essential, not only in solution but also in a host media. Till date, there have been previous reports on polymer-QD composites. The QDs, mostly the II-VI type Cd based ones, have been studied extensively for their use in polymer matrix to benefit from the advantageous properties of the polymers [125,126,127]. By using them in a composite form, QDs gain elasticity and processability which they cannot provide in their synthesized form [128]. Film formation using QDs in solution is challenging and requires a high level of understanding of the behavior of complex mixtures of such materials in order to make films with high optical quality. The optimal QD film should be capable of standing alone; provide versatility, flexibility, mechanical strength; and be able to be fabricated in large areas. This requirement presently drives the research on stand-alone flexible

films of QDs. Considering the research efforts for the large-area flexible electronics [129], the implementation of the QD based large-area systems is highly desirable for large-area optoelectronic device applications, e.g., sensors and displays. So far, literature lacks on the demonstration of free standing QD films except for a few reports with just of a few cm \times cm area. In their report, Tetsuka *et. al.* [130] presented small-area flexible clay films of Cd-containing QDs. Although this work provides a good level of understanding of the use of QDs in films, the procedure is challenging since it requires ligand exchange of the dots and preparation of the clay suspension. Also, from the applications point of view, the use of Cd-containing QD films are not favored due to their toxicity. Therefore, In-based QDs make a strong candidate as a possible alternative to their toxic Cd-containing counterparts.

While research on Cd-based colloidal QDs (CdSe, CdTe, CdSe/CdS, CdSe/ZnS) is quite mature with respect to their synthesis and applications [58,131,132,133, 134]. Research on In-based QDs has mainly focused on the synthesis methodology and understanding of the growth mechanisms and crystal structure of these dots [79, 80, 135,136,137,138,139]. Moreover, the use of In-based QDs for various applications have not been investigated except for a few reports that discuss about lasing possibilities and imaging of cells [140,141]. To cater for these missing points, we propose and demonstrate a flexible, stand-alone, very large-area films of InP/ZnS QDs promising for high-end applications. We also show white light generation using these membranes hybridized on a blue LED platform for remote phosphor application and study the emission kinetics and nonradiative energy transfer among the different sized QDs as a function of temperature, which has not been addressed in the literature till date.

8.2 Results and discussion

In this work, InP/ZnS QDs with fatty acid ligands are used, which do not require any ligand exchange in the subsequent membrane formation process. The ligand, myristic acid, employed for the synthesis of QDs, is a fatty acid that provides a good hydrophobic surface when mixed with poly (methyl methacrylate) (PMMA) (Fig.8.2.1). Furthermore, QDs dissolved in PMMA can be peeled off easily from the substrate after the solvent is evaporated (see Fig. 8.2.1). In addition, control experiments were performed using only PMMA and PMMA mixed with TOPO and oleic acid capped QDs and it was found that these do not allow the formation of stand-alone films.

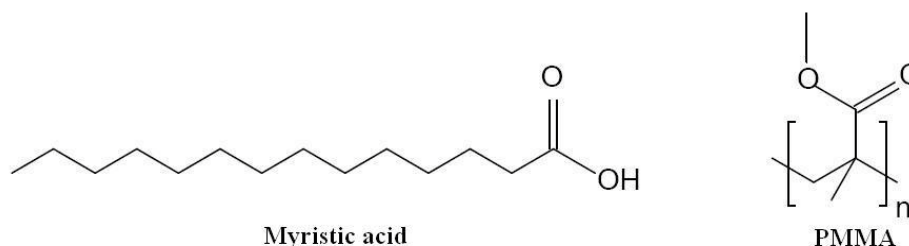


Figure 8.2.1. Chemical structure of the myristic acid (left) and PMMA (right).

The details of the sample preparation are given as follows: As-synthesized InP/ZnS QDs (for which the synthesis method is given in Section 3.3.1) are cleaned using isopropanol, acetone and methanol extraction to get rid of the excess amount of organic ligands and the precipitated particles are dissolved in fresh hexane. PMMA, A15 (MicroChem) is diluted with anisole and the QDs are injected into the PMMA resin under strong mixing conditions. The solution is stirred further for 30 min to prevent any possible agglomeration and to mix well the QDs with the PMMA and then drop-casted on the pre-cleaned glass substrate. The QD film is left to dry under a controlled evaporation set-up overnight and then peeled off easily from the substrate to provide a high optical

quality, free-standing, flexible film. The peeling of the film is possible because of the interaction of the ligand of the QDs, the fatty myristic acid, with PMMA, thus providing a hydrophobic layer on glass substrate ready to be peeled off from the surface. The contact angle measurements provided in the Fig. 8.2.2 also confirms that the films are hydrophobic.

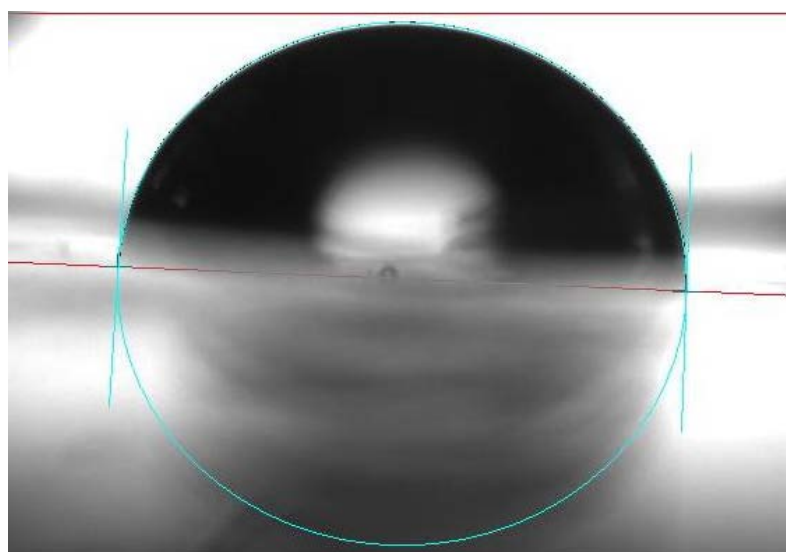


Figure 8.2.2 Contact-angle measurement of the free standing InP/ZnS film showing the hydrophobic property with contact angles of $\sim 89^\circ$ (for left and right).



Figure 8.2.3 Photograph of the 50 cm \times 50 cm PMMA-InP/ZnS QD membrane under room light (left) and UV illumination (right).

In order to characterize the internal elemental structure of the film, we carried out X-ray photoelectron spectroscopy (XPS) experiments. The high resolution Carbon 1s and Oxygen 1s spectra for the PMMA polymer, InP/ZnS QDs and the composite are shown in Fig. 8.2.4. For PMMA, C 1s spectra are resolved into three components with different bonding states, i.e., C-C at 285 eV, O-CH₃ at 286.5 eV, and O-C=O at 288.9 eV, respectively. O 1s spectra of PMMA consist of two components, i.e., C=O at 532.1 eV and C-O-C at 533.6 eV. The atomic percentage of the peaks are C-C (51.49 %), O-CH₃ (15.12 %), O-C=O (11.18 %), C=O (9.79 %), and C-O-C (12.42 %), which is almost similar to standard XPS spectra of PMMA [142]. High Resolution C 1s and O 1s spectra of QDs (due to ligands) show single peaks at 285.0 eV and 532.1 eV, respectively. The C 1s spectra of the composite (PMMA-QD film) are also resolved into three components and O 1s spectra are resolved into two components similar to pure PMMA. Although we do not observe shifts in the peaks, we observe modifications in the atomic percentages of the peaks due to the presence of QDs in the composite. In this the atomic percentage of the peaks are C-C (58.58 %), O-CH₃ (11.03 %), O-C=O (5.26 %), C=O (22.29 %) and C-O-C (2.84 %). We also observed a huge decrease in the intensity of C 1s peak of pure QDs in the mixture, which also suggests change in the microenvironment of QDs in the presence of PMMA.

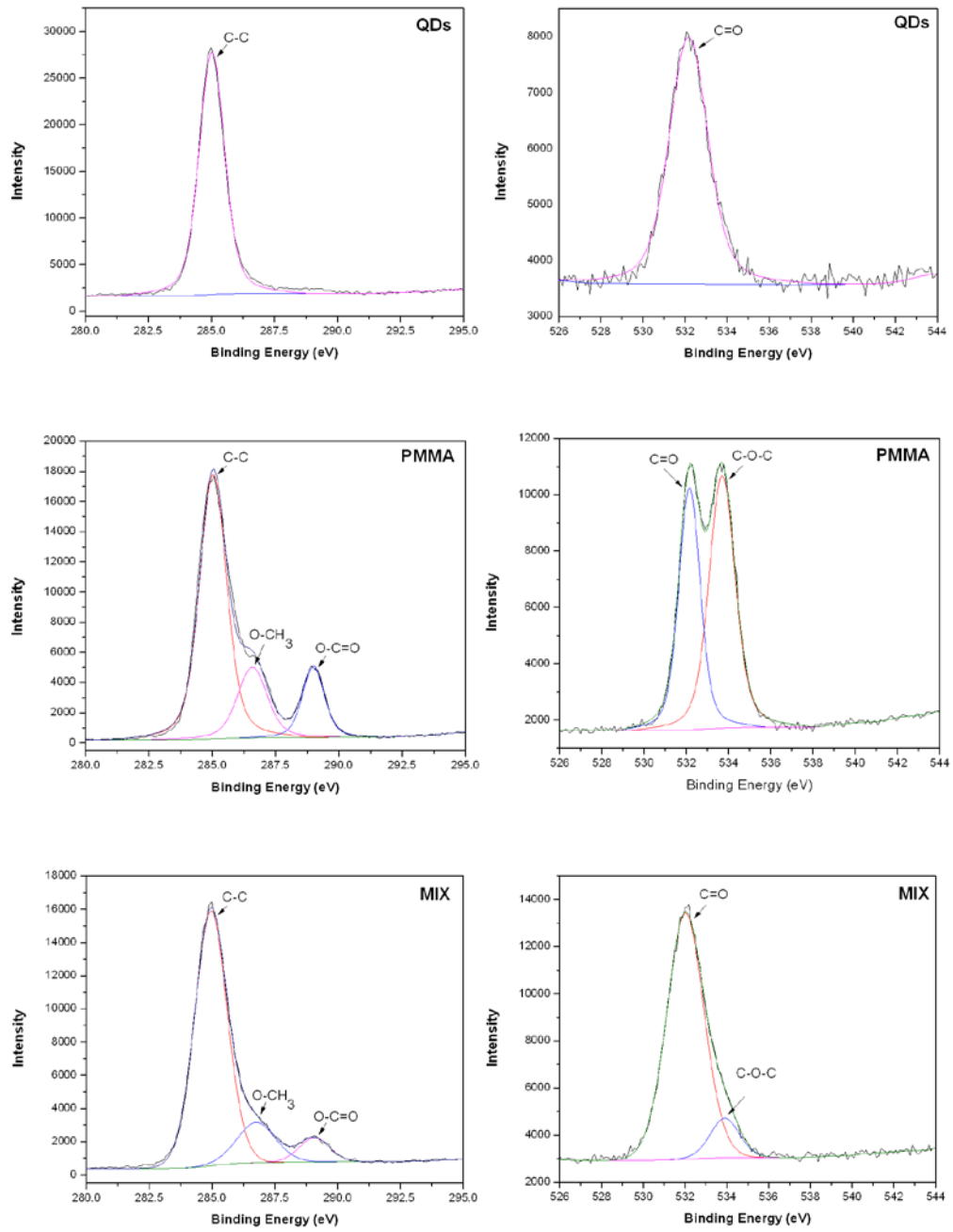


Figure 8.2.4 XPS spectra of InP/ZnS QD only, PMMA only, and the composite membrane for elemental carbon analysis.

A typical XPS survey spectrum for the PMMA-QD composite is shown in Fig. 8.2.5. The survey scan indicates the presence of In, P, Zn, and S from the InP/ZnS QDs as well as C, and O from the PMMA polymer. A high-resolution XPS spectrum for all elements has been also shown. The In core is orbit split to $3d_{5/2}$ and $3d_{3/2}$, with the $3d_{5/2}$ peak positioned at 444.40 eV and the $3d_{3/2}$ peak positioned at 451.96 eV. The P 2p core shows two peaks, one at 129.17 eV corresponding to P from InP and the other at 132.54 eV corresponding to oxidized P species. HR-XPS spectra of S 2p (161.86 eV) and spin-orbit split Zn $2p_{3/2}$ (1021.70 eV), $2p_{1/2}$ (1044.76 eV) are also presented. This is further confirmed by the shift in the QD elemental peaks by 0.3 eV in the composites in comparison to the pure QDs (see Fig. 8.2.5) [143]. This shift is presumably due to the fact that existence of polymer influences the microenvironment of the elemental ions in QDs. XPS results confirmed that the PMMA QD mixture is a composite structure.

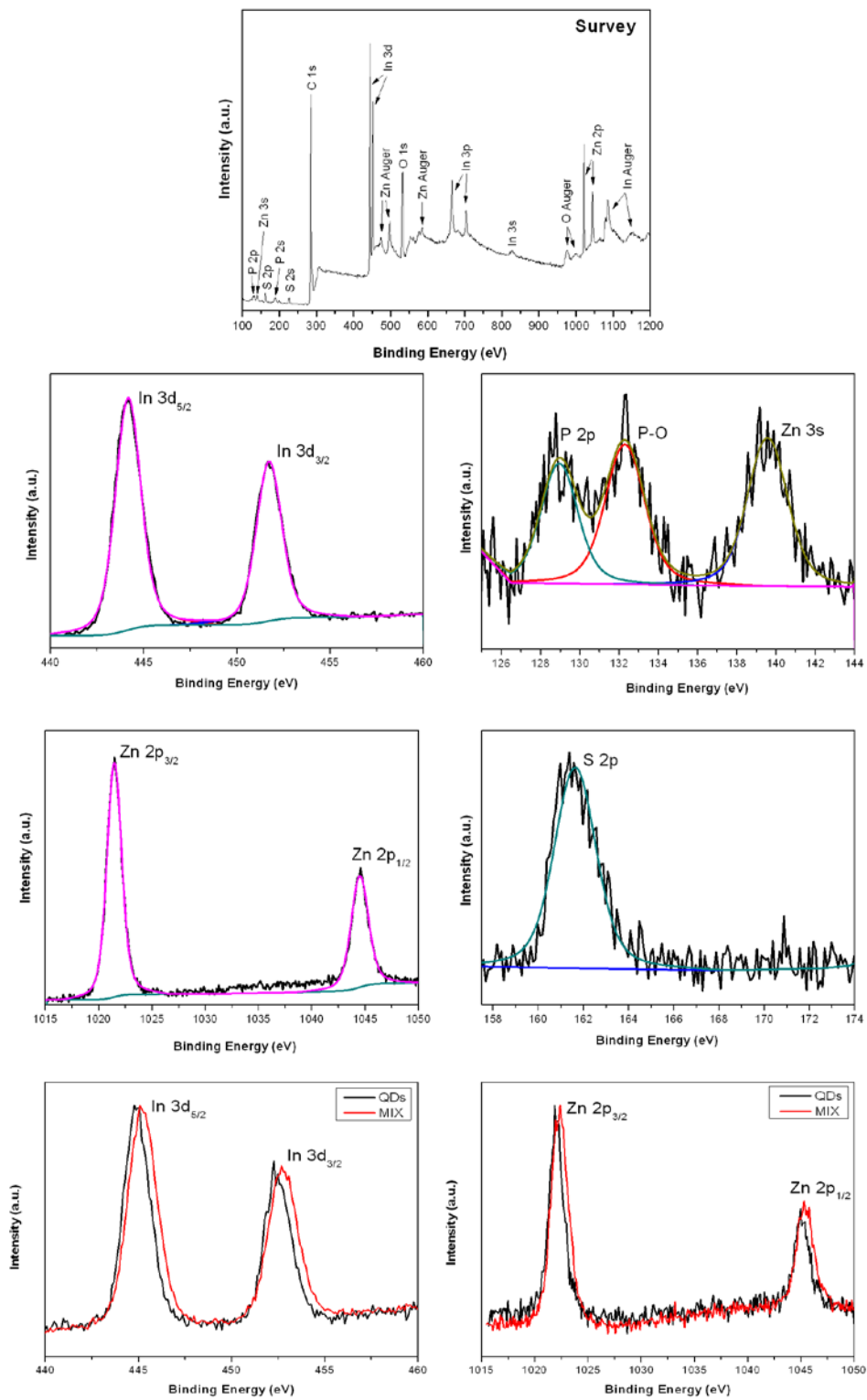


Figure 8.2.5 XPS spectra of the InP/ZnS QD-PMMA membrane.

In order to investigate the mechanical properties of the film, a stress-strain characterization applying a load on the membrane is performed. For the tests using a 35 μm thick film, the ultimate tensile strength, σ_{uts} , is found to be 28.6 MPa, while the offset yield strength at 0.2%, $\sigma_{.2\% \text{ys}}$, is 28.4 MPa and the Young modulus, E , is 2.85 GPa, which is in the range of the reported Young Modulus value for the PMMA (see Fig. 8.2.6).

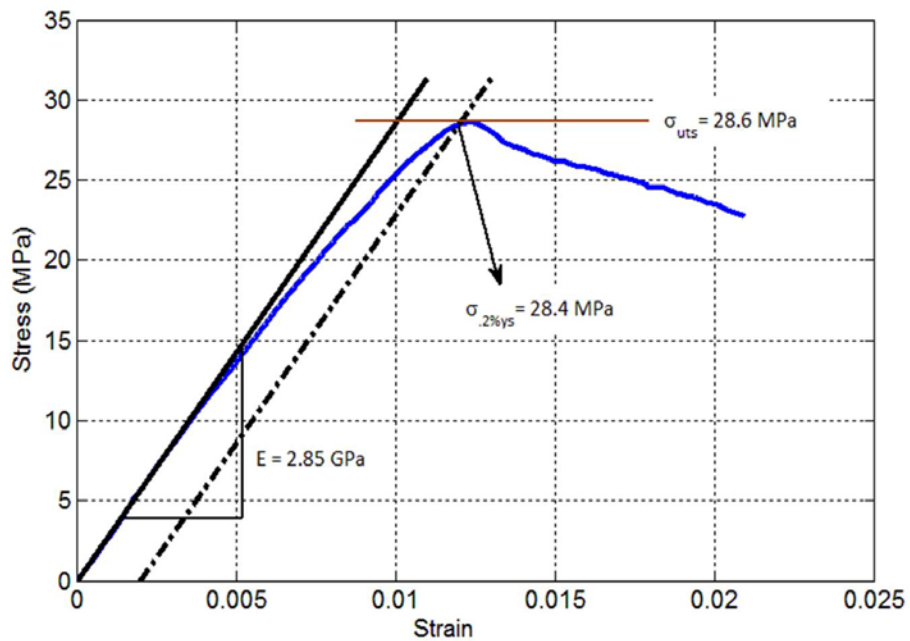


Figure 8.2.6 Stress-strain measurement of a 35 μm thick InP/ZnS QD-PMMA film.

To investigate the kinetics of InP/ZnS QDs in film form, we studied a Förster-type nonradiative energy transfer (FRET) between the different sized dots. The use of QDs as energy transfer agents for FRET-based applications is also an important area for the utilization of QDs since FRET plays a significant role in the development of new platforms for light detection, light harvesting, etc. [7,144,145,146]. Such FRET-based systems have been widely used in connection with dyes, proteins, and other nanostructured materials including nanowires, quantum wells, and QDs [46,105,106,107,147,148,149,150].

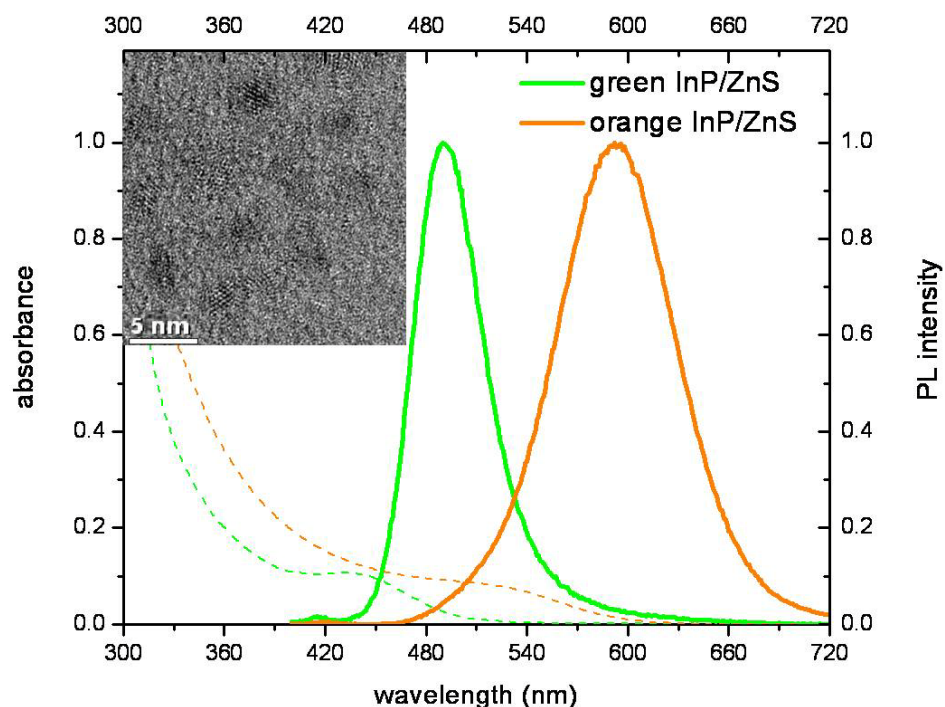


Figure 8.2.7 Normalized room temperature photoluminescence (solid line) and absorption (dashed line) spectra of the donor and acceptor InP/ZnS QDs. Transmission electron microscopy (TEM) image of the donor/acceptor QDs (inset).

Fig. 8.2.7 shows the emission and absorption spectra of exemplary InP/ZnS QDs in solution together with the transmission electron microscopy (TEM) image in the inset. The donor and acceptor QD diameter here is measured to be ~ 2.4 and 2.8 nm, respectively both with a size variation of $\sim <10\%$. The acceptor QDs are chosen to emit around 100 nm away from the donor emission peak to prevent the emission overlap to a significant extent.

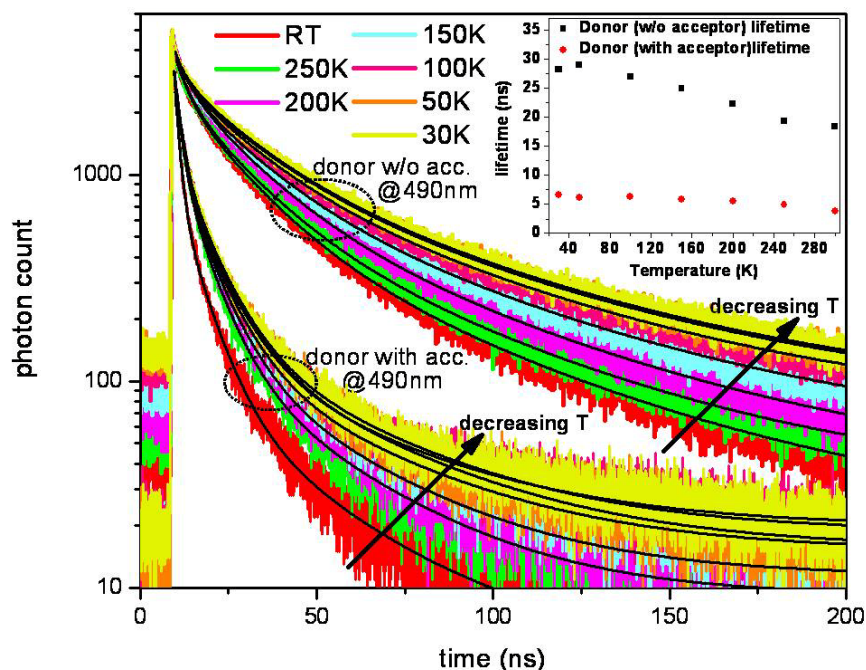


Figure 8.2.8 Time resolved photoluminescence (TRPL) spectra of the donor QD without the acceptor (top) and the donor QD with the acceptor (bottom), measured at the donor emission wavelength of 490 nm, as a function of decreasing sample temperature (inset). The exponential fits of the observed decays for the donor (with and without acceptor) are also given.

The effect of the acceptor on the donor emission kinetics, i.e., FRET between the dots, is studied by comparing the time resolved photoluminescence (TRPL) spectra of the bare donor QD containing film with the donor-acceptor mix QD film (with both samples having the same donor concentration) (see Fig. 8.2.8). In the films, the peak emission wavelengths of the donor and acceptor QDs are 490 and 590 nm, respectively. Therefore, they are spectrally well separated from each other (see Fig. 8.2.14), which makes the time-resolved analysis viable. The temperature dependence of the time-resolved fluorescence for each species of interest was also investigated and the decay curves were fit using a tri-exponential fitting function. Using tri-exponentials for the fitting is due to the nontrivial emission kinetics of the InP/ZnS QDs. The amplitude-weighted-lifetime values, for the donor only films, range from 18.45 to 28.26 ns as the sample temperature is decreased from 300 to 30 K. As the donor only sample

was cooled from room temperature to cryogenic temperatures (30 K), the photoluminescence decay curves slowed down, which implies the suppression of nonradiative recombination channels. (The in-film PL intensity of the donor and acceptor QDs as a function of temperature is given in Fig. 8.2.9.) In addition, we compare the emission kinetics of the donor only sample with the donor-acceptor hybrid membrane. We observe a significant decrease in the lifetime of the donor QDs when they are in the presence of acceptors. In other words, the donor lifetime decreases as it transfers its excitation energy to an acceptor present in close proximity in the film. Another conclusion derived from the temperature dependent lifetime measurements of the hybrid film is that, as the film is cooled to cryogenic temperatures, the nonradiative recombination channels are suppressed. Therefore, the lifetime becomes longer as in the case of the donor only film. These results are shown in Fig. 8.2.8 together with the insets of the temperature dependent lifetimes of the donor only and hybrid samples, and are summarized in Table 8.2.1. The change of the photoluminescence intensity of the donor and acceptor QDs as changing the sample temperature is also shown in Fig. 8.2.9, which indicates the suppression of the nonradiative recombination as the sample is cooled down.

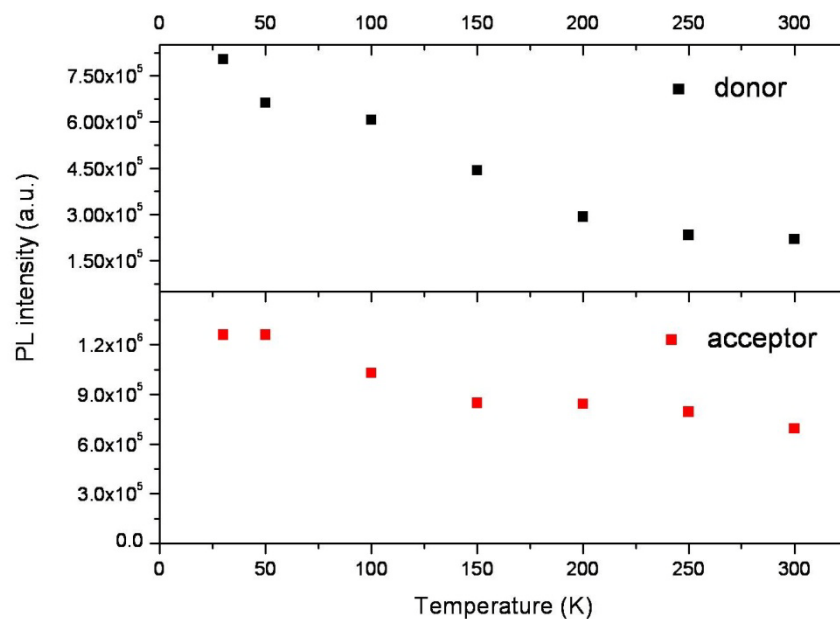


Figure 8.2.9 Temperature dependent photoluminescence intensity of the donor (top) and acceptor (bottom) QDs, extracted from the time-resolved photoluminescence measurement. The photoluminescence intensity is extracted from the set-up using the same time interval for the photon counts.

Using the modification of the donor lifetimes, we calculate the corresponding FRET efficiencies using Eqn. 7.2.1. We observe ~80% energy transfer efficiency (see Fig. 8.2.10 and Table 8.2.2), which is in good agreement with our theoretical model based on exciton-exciton interaction. In addition, the donor energy transfer rates, extracted from the experimentally measured lifetime values have been given in Fig. 8.2.11.

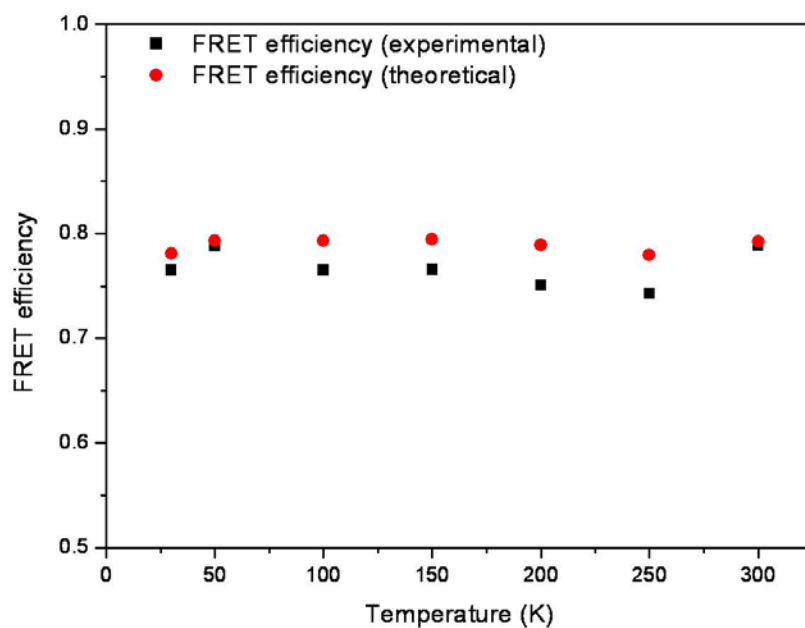


Figure 8.2.10 Theoretical (red circles) and experimental (black squares) FRET efficiencies as a function of temperature.

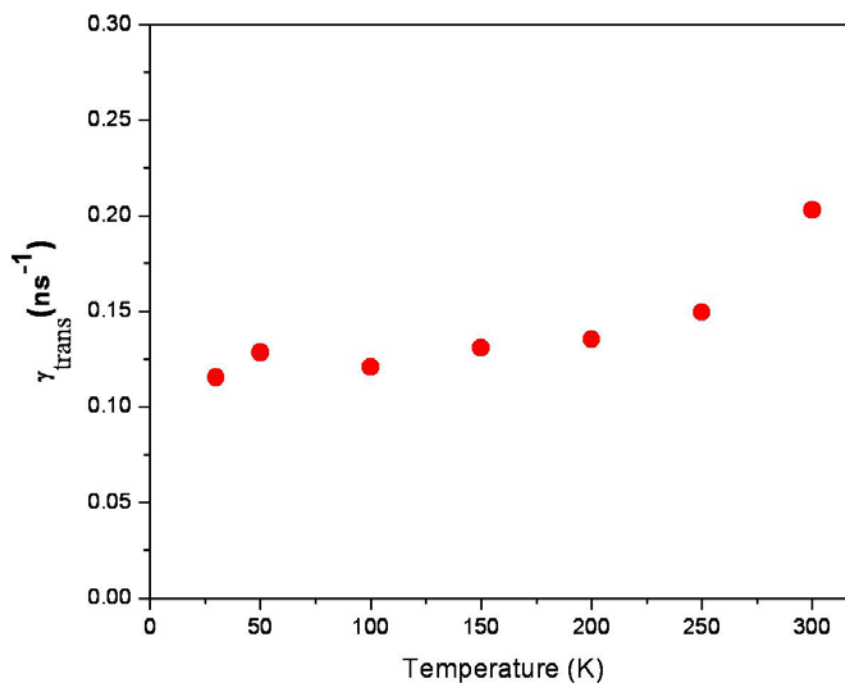


Figure 8.2.11 Donor energy transfer rate calculated using the experimentally measured lifetime values as a function of temperature.

From the acceptor point of view, the energy feeding increases its lifetime, which is an indication for the FRET mechanism. Fig. 8.2.12 depicts the decays and the modifications observed in the acceptor lifetime when an acceptor only film is compared with that of a hybrid film. The acceptor lifetime increases as the sample is cooled to cryogenic temperatures. By comparing the acceptor emission in the hybrid form with the acceptor only case (with the same amount of acceptor dots), we observe that the acceptor lifetime is increased as a result of the energy transfer indicating the Förster-type energy transfer. Due to the possible emission overlap, stemming from the donor emission tail that extends towards the peak emission wavelength of the acceptor, we also investigated the changes in the lifetime of the acceptor emission at 640 nm, far from the donor emission tail. The acceptor lifetime trends are similar to those observed at 590 nm; but, in this case, the lifetime values are greater because the decay kinetics of the QDs is different at different wavelengths.

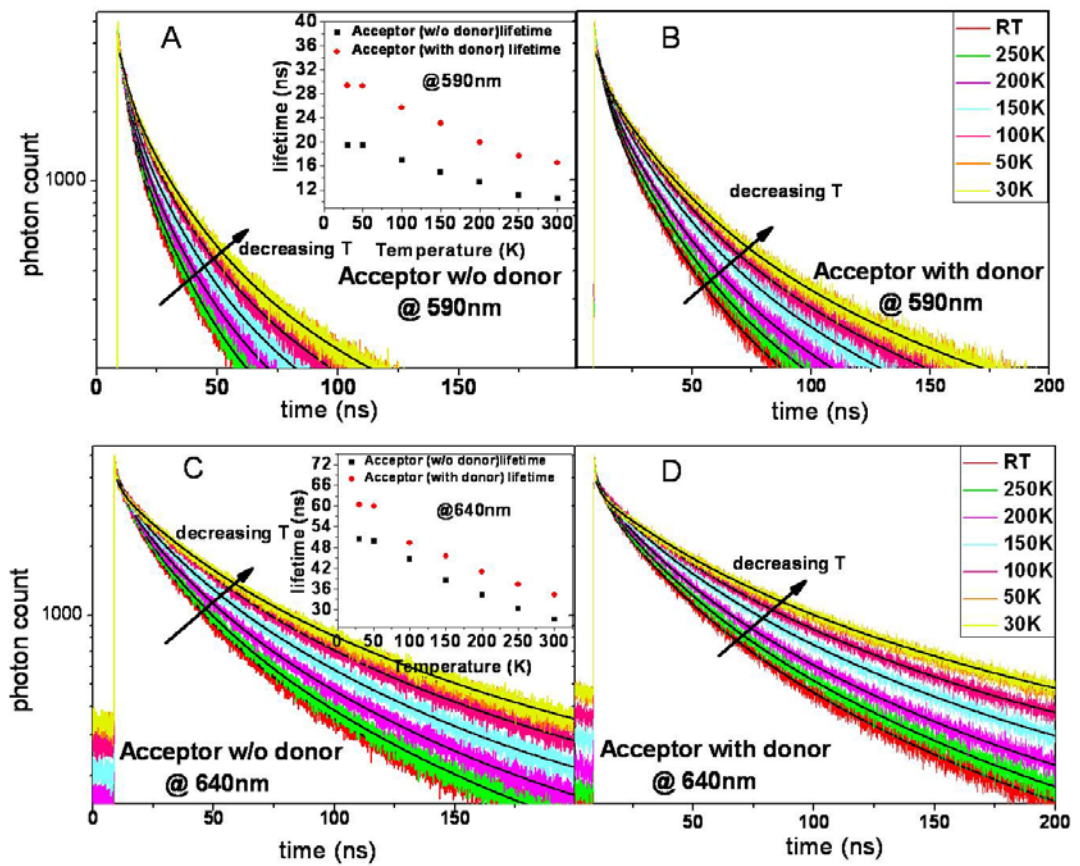


Figure 8.2.12 (A) TRPL spectra of the acceptor without the donor (at 590 nm); (inset) the acceptor lifetimes (with and without the donor). (B) TRPL of the acceptor with the donor (at 590 nm). (C) TRPL of the acceptor (without the donor) (at 640 nm, far from the donor emission tail), (inset) the acceptor lifetimes (with and without the donor). (D) TRPL of the acceptor (with the donor) (at 640 nm). All curves and data are given parametrized with respect to or as a function of the temperature and the lifetimes are fit with triple exponentials.

Analysis of the changes in the lifetime of the acceptor				
Temp (K)	Acceptor lifetime (@590nm) (ns)	Donor+Acceptor hybrid lifetime (exp)(@590nm) (ns)	Donor+Acceptor hybrid lifetime (theory) (ns)	Donor+Acceptor hybrid lifetime (theory, including T dependence) (ns)
300	10.53	16.56	18.84	17.65
250	11.07	17.62	19.80	20.87
200	13.33	19.92	23.85	24.09
150	14.94	23.14	26.73	27.31
100	16.95	25.73	30.32	30.53
50	19.46	29.33	34.81	33.75
30	19.44	29.39	34.78	35.04

Table 8.2.1 Experimental and theoretical changes in the lifetime of the acceptor alone and in the hybrid film with the donor at different temperatures.

In our theoretical approach, we describe the optical properties of InP/ZnS QDs consisting of two different sizes. We consider a single QD pair composing of a donor (a smaller QD) and an acceptor (a larger QD), which are under exciton-exciton interaction. Within the simplest rate model, the lifetime in the presence of an acceptor is given by

$$\tau_{DA}^D = \frac{\tau_{exc}^D}{1 + \left(\frac{R_0}{r}\right)^6} \quad 8.2.1$$

where τ_{DA}^D is the donor (acceptor) exciton lifetime when the energy transfer takes place. The energy transfer rate (γ_{trans}) between the D-A QD pair is given by

$$\gamma_{trans} = \frac{1}{\tau_D} \left(\frac{R_0}{r}\right)^6 \quad 8.2.2$$

where R_0 is the Förster radius for the D-A pair and r is the separation distance for the D-A QD pair.

Table 8.2.2 shows the experimental and theoretically calculated lifetimes for the donor and acceptor pairs when the measurements are analyzed at both the donor and acceptor emission wavelengths. The average separation distance, r , between the D-A pair is estimated to be 3.63 nm. The Förster radius is calculated as 4.52 nm.

Analysis of the changes in the lifetime of the donor					
Temp (K)	Donor lifetime (@490nm) (ns)	Donor+Acceptor hybrid lifetime(exp)(@490nm) (ns)	Donor+Acceptor mixed lifetime (theory, including T dependence) (ns)	FRET eff. (exp)	FRET eff. (theory, including T dependence)
300	18.45	3.89	3.83	0.789	0.793
250	19.32	4.97	4.26	0.742	0.779
200	22.27	5.55	4.70	0.751	0.789
150	24.99	5.85	5.14	0.766	0.794
100	26.99	6.33	5.57	0.765	0.793
50	29.04	6.14	6.01	0.789	0.793
30	28.26	6.63	6.18	0.765	0.781

Table 8.2.2 Experimental and theoretical changes in the lifetime of the donor alone and in the hybrid film with the acceptor, along with the FRET efficiencies, at different temperatures.

Fig. 8.2.13 illustrates exciton-exciton interaction model we use for a donor (D) and acceptor (A) QD pair. Within the simplest rate model, the number of excitons (N_{exc}) trapped in the QD, under constant illumination (steady-state condition), is given by

$$-(\gamma_{exc}^D + \gamma_{trans})N_{exc}^D + I_D = 0 \quad 8.2.3$$

$$-(\gamma_{exc}^A)N_{exc}^A + \gamma_{trans}N_{exc}^D + I_A = 0 \quad 8.2.4$$

where $N_{exc}^{D(A)}$ is the number of donor (acceptor) excitons, $I_{D(A)}$ is the exciton generation rate due to the light excitation, and $\gamma_{exc}^{D(A)} = \gamma_{exc,rad}^{D(A)} + \gamma_{exc,non-rad}^{D(A)}$ is the donor (acceptor) exciton recombination rate in the absence of the acceptor (donor). $\gamma_{exc,rad}^{D(A)}$ and $\gamma_{exc,non-rad}^{D(A)}$ are the radiative and nonradiative components of $\gamma_{exc}^{D(A)}$. γ_{trans} is the energy transfer rate between the donor and acceptor. By substituting N_{exc}^D from Eqn. 8.2.3, Eqn. 8.2.4 can be written as

$$-(\gamma_{exc}^A)N_{exc}^A + \gamma_{trans} \left(\frac{I_D}{\gamma_{exc}^D + \gamma_{trans}} \right) + I_A = 0 \quad 8.2.5$$

Assuming that $I_D \cong I_A = I_0$, then Eqn. 8.2.3 and 8.2.5 are rearranged as follows:

$$-(\gamma_{exc}^D + \gamma_{trans})N_{exc}^D + I_0 = 0 \quad 8.2.6$$

$$-(\gamma_{exc}^A) \left(\frac{\gamma_{exc}^D + \gamma_{trans}}{\gamma_{exc}^D + 2\gamma_{trans}} \right) N_{exc}^A + I_0 = 0 \quad 8.2.7$$

From the last two equations, one defines

$$\gamma_{DA}^D = (\gamma_{exc}^D + \gamma_{trans}) \quad \mathbf{8.2.8}$$

$$\gamma_{DA}^A = (\gamma_{exc}^A) \left(\frac{\gamma_{exc}^D + \gamma_{trans}}{\gamma_{exc}^D + 2\gamma_{trans}} \right) \quad \mathbf{8.2.9}$$

where $\gamma_{DA}^{D(A)}$ is the donor (acceptor) exciton recombination rate in the presence of energy transfer. For the energy transfer rate between the D-A QD pair, we use $\gamma_{trans} = \gamma_D \left(\frac{R_0}{r} \right)^6$, where R_0 is the Förster radius for the D-A pair and r is the separation distance for the D-A QD pair (This assumption is reasonable because the energy transfer between spherical QDs is well described by the Förster theory). Therefore, Eqns. 8.2.8 and 8.2.9 are given by

$$\gamma_{DA}^D = \gamma_{exc}^D \left(1 + \left(\frac{R_0}{r} \right)^6 \right) \quad \mathbf{8.2.10}$$

$$\gamma_{DA}^A = \gamma_{exc}^A \left(\frac{1 + \left(\frac{R_0}{r}\right)^6}{1 + 2\left(\frac{R_0}{r}\right)^6} \right) \quad 8.2.11$$

In terms of lifetimes,

$$\tau_{DA}^D = \frac{\tau_{exc}^D}{1 + \left(\frac{R_0}{r}\right)^6} \quad 8.2.12$$

$$\tau_{DA}^A = \tau_{exc}^A \left(\frac{1 + 2\left(\frac{R_0}{r}\right)^6}{1 + \left(\frac{R_0}{r}\right)^6} \right) \quad 8.2.13$$

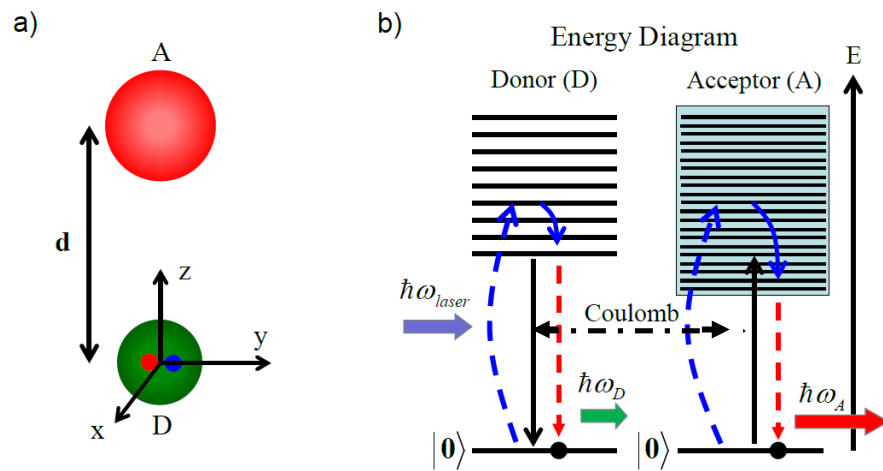


Figure 8.2.13 (a) Donor-Acceptor (D-A) schematic for a single donor (D) and acceptor (A). (b) Energy diagram for the D-A pair energy transfer process. Blue dashed lines represent the absorption process of the QD (donor/acceptor). Blue solid lines show fast relaxation process. Red dashed lines illustrate light emission process (relaxation from the lowest excited state to the ground state). Black solid lines represent the energy transfer from the donor to the acceptor. Horizontal black dashed line shows the Coulomb interaction between the donor and acceptor.

Fig. 8.2.14 shows the emission spectra of the donor only and acceptor only photoluminescence spectra of the QDs, together with the hybrid donor-acceptor emission spectra under the room temperature conditions. As a result of FRET, the donor emission is suppressed by ~80% whereas the overall acceptor emission is increased by ~30%, which is obtained from the hybrid emission spectra (fit to the donor-acceptor emission in a Gaussian profile form, as shown in the inset of Fig. 8.2.14). We also compare the results of the time-resolved measurements with the room temperature steady-state measurements. The modification of the steady-state photoluminescence of the donor and acceptor matches quite well that of the room temperature time-resolved lifetime modifications (79% for the donor and 57% for the acceptor). This implies that the excitons transferred from the donor are partly contributed to the nearby acceptor. Here the theoretical analysis, we considered the temperature dependence using a semi empirical approach by calculating the change in the lifetime of the donor/acceptor species as a function of temperature (see inset Fig. 8.2.8 and 8.2.9).

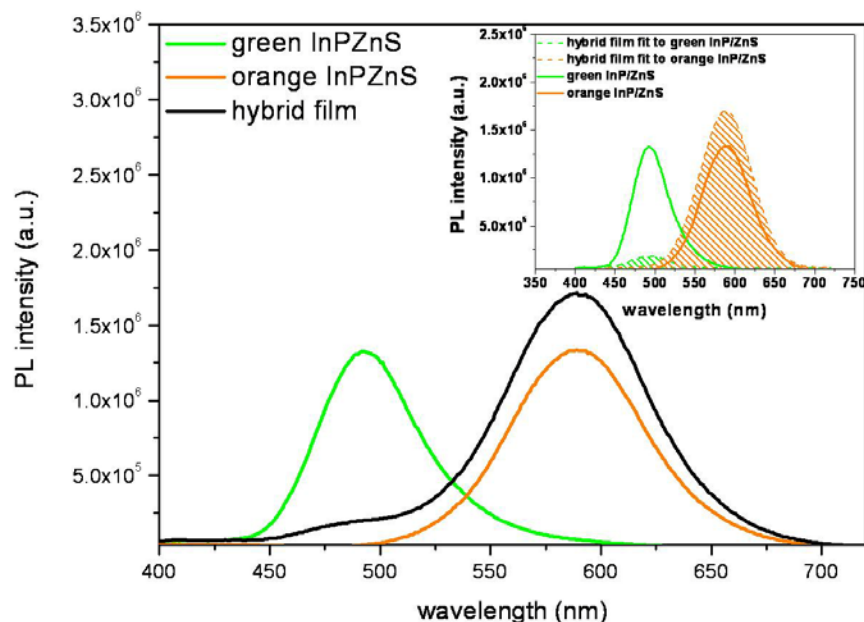


Figure 8.2.14 Steady-state room temperature photoluminescence spectra of the donor only, acceptor only and hybrid film. Steady-state room temperature photoluminescence spectra of the donor only, acceptor only and hybrid film of the same when the hybrid emission is fit to the donor and acceptor emissions as Gaussian curves (inset).

Finally, as a possible promising demonstration of the stand-alone films, we employed the bilayer films for the white light generation, to be hybridized on a blue LED platform. The white light generation using InP-based emitters has been addressed in the literature by Nann and coworkers using red emitting InP/ZnS QDs, whereas the green gap has been resolved using a doped phosphors. On the other hand in this work, as the first time demonstration, we present the white LED (WLED), in which both red and green color components have been provided by our bilayer architecture consisting of green and red InP/ZnS QDs forming the membrane.

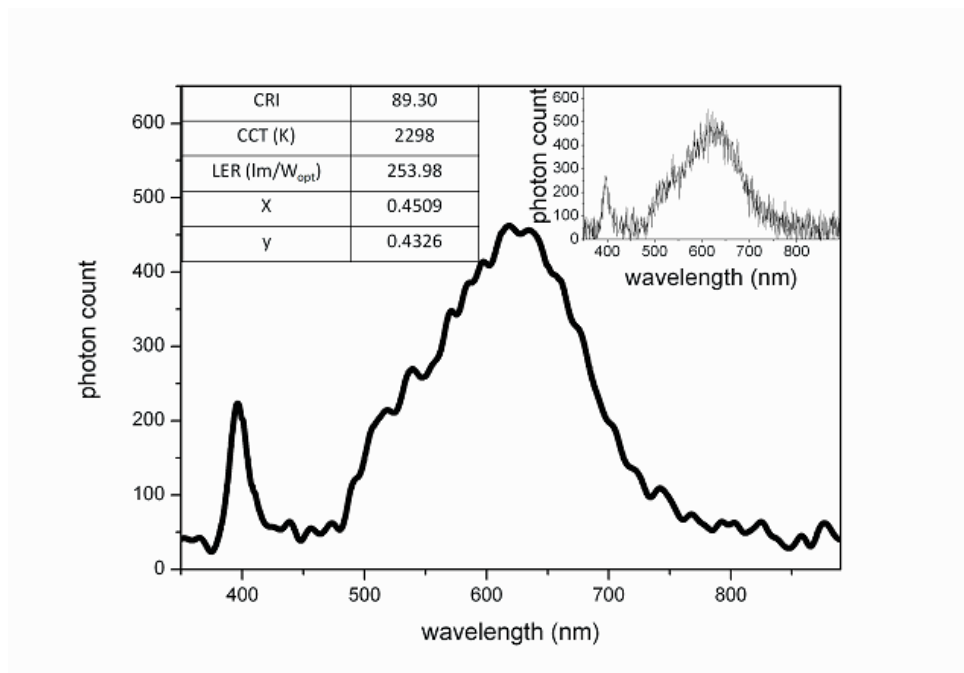


Figure 8.2.15 Emission spectra of the color-conversion white LED (WLED) when the blue LED chip is hybridized with our bilayer InP/ZnS QDs.

Fig. 8.2.15 shows the emission spectra of the blue LED hybridized with the green-red emitting QD films. The white light generation using the excitation from the blue LED results in a color rendering index CRI value of 89.30 with a correlated color temperature CCT of 2298 K and a luminous efficacy of optical radiation LER of 253.98 lm/W_{opt}. Here these figures of merits used are explained as follows: The color rendering index, CRI, is the capability to reflect the true colors of the illuminated objects. The correlated color temperature, CCT, is the temperature defined for the closest Planckian black-body radiator to the operating point on the chromaticity diagram. Luminous efficacy of optical radiation, LER, is the spectral efficiency of the light source recognized by the human eye [151].

8.3 Summary

In this chapter, the fabrication of the very large-area, free-standing films of the InP/ZnS QDs and its WLED application have been demonstrated. Different sized QDs have been used to study the Förster- type nonradiative energy transfer between them. The experimental data match well the theoretical results based on an exciton-exciton interaction model among the donor-acceptor pairs. Furthermore, the temperature dependent emission kinetics of the donor-acceptor species has been studied to provide a better understanding of the emission kinetics. The implementation of the very large-area Cd-free QD membrane and the FRET among them QDs holds great promise for future innovative optoelectronics and biological applications.

Chapter 9

Conclusions

To date FRET has been used as a tool for various purposes including the determination of molecular distance, molecular conformational changes and biomolecular activity. In the previous literature, QDs have been used with organic dyes and fluorophores to form FRET mediating systems. In this thesis, we proposed and demonstrated tunable, versatile FRET mediated light harvesting systems, together with the introduction of a new concept of the enhancement of the acceptor emission by FRET mechanism. From the light harvesting application point of view, the FRET efficiency itself is found to be misleading as strong FRET does not necessarily imply strong light harvesting. In our work, the light harvesting is demonstrated using the steady-state photoluminescence enhancement of the acceptor side, supported by the increased lifetime of the acceptor due to the energy feeding from the donor species. This enhancement of the acceptor emission has been used as a powerful proof-of-concept demonstration to make the point for the use of the energy transfer mechanisms that we have addressed in light harvesting.

In the scope of this thesis work, we studied the implementation of nanocrystal QDs for several light harvesting systems. We proposed and demonstrated the light harvesting mediated by the excitonic energy transfer both for the QD-organic dye and the quantum-dot fluorescent protein complexes to overcome the limitations of these organic fluorophores. We also demonstrated very large-area stand-alone flexible membranes of Cd-free QDs (50 cm × 50 cm) to provide new possibilities for high-end, large-scale light harvesting applications. A short itemized summary of overall achievements and contributions to the literature in this thesis is given as follows.

- Colloidal quantum dot synthesis:

- Synthesis of various kinds of semiconductor nanocrystals including aqueous CdTe and organic CdSe,
- Synthesis of near-unity efficiency CdSe/CdS QDs using SILAR method.
- Synthesis of Cd-free core/shell InP/ZnS QDs.

- Demonstration of FRET mediated light harvesting in QD-fluorescent protein complexes:

- Enhancement of green fluorescent protein emission by the use of water soluble QDs up to 15 folds and demonstration of controlled energy transfer by enzymatic activity.

- Demonstration of FRET mediated light harvesting in QD-organic dye pairs:

- Exciton harvesting of organic dyes with charged CdSe/ZnS QDs providing more than 10 fold emission enhancement for dye molecules, together with 90% FRET efficiencies.
- Utilizing water-based different-sized CdTe QDs for efficient exciton harvesting, and tuning of the energy transfer to organic dye molecules with >85 % FRET efficiencies and strong lifetime modifications.

- Implementation of large-area flexible membranes of Cd-free QDs:

- Demonstration of very large-area (50 cm × 50 cm), flexible and stand-alone membranes of InP/ZnS QD-polymer composites.

- Study of temperature dependent emission kinetics and energy transfer mechanism among different sized quantum dots.
- Proof-of-concept demonstration of white light generation with InP/ZnS QD-polymer composites using the excitation from the blue LED resulting in a color rendering index CRI value of 89.30 with a correlated color temperature CCT of 2298 K and a luminous efficacy of optical radiation LER of 253.98 lm/W_{opt}.

These results presented in this thesis overall provide a good level of understanding about the physics and applications of the Förster-type nonradiative energy transfer mediated light harvesting systems. The integration of such colloidal quantum dots with organic dye molecules and fluorescent proteins is believed to open up new possibilities with our proposed exciton harvesting enabled systems. Furthermore, with our proof-of-concept demonstrations, the large-area flexible membranes will pave the way for high-end, large-area systems. One of future directions is to make high-efficiency Cd-free quantum dots and utilize them in innovative light harvesting systems.

Below is given a list of SCI journal publications that resulted from this thesis research and related work during my graduate study at Bilkent University.

- **E. Mutlugun**, P. L. H. Martinez, Y. Coskun, C. Eroglu, T. Erdem, V. K. Sharma, E. Unal, S. K. Panda, S. G. Hickey, N. Gaponik, A. Eychmuller, and H. V. Demir, “Very large-area free-standing membranes of colloidal InP/ZnS quantum dots,” in submission (2011).

- **E. Mutlugun**, U. O. S. Seker, P. L. H. Martinez, and H. V. Demir “Exciton harvesting of nanocrystal quantum dots for green fluorescent proteins,” in submission (2011).

- **E. Mutlugun**, O. Samarskaya, T. Ozel, N. Cicek, N. Gaponik, A. Eychmuller, and H. V. Demir, “Highly efficient nonradiative energy transfer mediated light harvesting in water using aqueous CdTe quantum dot antennas,” *Optics Express*, **18**, 10, 10720-10730 (2010).

- B. Güzeltürk*, **E. Mutlugun***, X.Wang, K. L. Pey, and H. V. Demir, “Photovoltaic nanopillar radial junction diode architecture enhanced by integrating semiconductor quantum dot nanocrystals as light harvesters,” *Applied Physics Letters*, **97**, 093111 (2010). (*equal contribution)

- **E. Mutlugun**, S. Nizamoglu, and H. V. Demir, “Highly efficient nonradiative energy transfer using charged CdSe/ZnS nanocrystals for light-harvesting in solution,” *Applied Physics Letters*, **95**, 033106 (2009).

- **E. Mutlugun**, I. M Soganci, and H. V. Demir, “Photovoltaic nanocrystal scintillators hybridized on Si solar cells for enhanced conversion efficiency in UV,” *Optics Express*, **16**, 3537-3545 (2008).

- **E. Mutlugun**, I. M. Soganci, and H. V. Demir, “Nanocrystal hybridized scintillators for enhanced detection and imaging on Si platforms in UV,” *Optics Express* **15**, 1128-1134 (2007).

- H. V. Demir, S. Nizamoglu, T. Erdem, **E. Mutlugun**, N. Gaponik, A. Eychmüller, “Quantum dot integrated LEDs using photonic and excitonic color conversion,” *Nano Today*, **6**, 632 (2011).

- H. V. Demir, U. O. S. Seker, G. Zengin, **E. Mutlugun**, E. Sari, C. Tamerler and M. Sarikaya, “Spatially Selective Assembly of Quantum Dot Light Emitters in an LED Using Engineered Peptides,” *ACS Nano*, **5**, 2735 (2011).

- T. Ozel, S. Nizamoglu, M. A. Sefunc, O. Samarskaya, I. O. Ozel, **E. Mutlugun**, V. Lesnyak, N. Gaponik, A. Eychmuller, S. V. Gaponenko, and H. V. Demir, “Anisotropic Emission from Multilayered Plasmon Resonator Nanocomposites of Isotropic Semiconductor Quantum Dots,” *ACS Nano*, **5**, 1328 (2011).

- N. K. Perkgoz, R. S. Toru, E. Unal, M. A. Sefunc, S. Tek, **E. Mutlugun**, I. M. Soganci, H. Celiker, G. Celiker and H. V. Demir, “Photocatalytic hybrid nanocomposites of metal oxide nano-particles enhanced towards the visible spectral range,” *Applied Catalysis B: Environmental*, **105**, 77 (2011).

- N. Cicek, S. Nizamoglu, T. Özel, **E. Mutlugun**, D. U. Karatay, V. Lesnyak, T. Otto, N. Gaponik, A. Eychmüller, and H. V. Demir, “Structural tuning of color chromaticity through nonradiative energy transfer by interspacing CdTe nanocrystal monolayers,” *Applied Physics Letters*, **94**, 061105 (2009).

- S. Nizamoglu, **E. Mutlugun**, O. Akyuz, N. Kosku Perkgoz, H. V. Demir, L. Liebscher, S. Sapra, N. Gaponik, A. Eychmüller, “White emitting CdS quantum dot nanoluminophores hybridized on near-ultraviolet LEDs for high-quality white light generation and tuning,” *New Journal of Physics*, **10**, 023026 (2008).

- S. Nizamoglu, **E. Mutlugun**, T. Özel, H. V. Demir, S. Sapra, N. Gaponik, A. Eychmüller, “Dual-color emitting quantum-dot-quantum-well CdSe-ZnS heteronanocrystals hybridized on InGaN/GaN light emitting diodes for high-quality white light generation,” *Applied Physics Letters*, **92**, 113110 (2008).

- H. V. Demir, S. Nizamoglu, **E. Mutlugun**, T. Özel, S. Sapra, N. Gaponik, A. Eychmüller, “Tuning shades of white light with multi-color quantum-dot-quantum-well emitters based on onion-like CdSe-ZnS heteronanocrystals,” *Nanotechnology*, **19**, 335203 (2008).

- T. Özel, I. M. Soganci, S. Nizamoglu, I. O. Huyal, **E. Mutlugun**, S. Sapra, N. Gaponik, A. Eychmüller, and H. V. Demir, “Selective enhancement of surface-state emission and simultaneous quenching of interband transition in white-luminophor CdS nanocrystals using localized plasmon coupling,” *New Journal of Physics*, **10**, 083035 (2008).

- I. M. Soganci, S. Nizamoglu, **E. Mutlugun**, O. Akin, and H. V. Demir, “Localized plasmon-engineered spontaneous emission of CdSe/ZnS nanocrystals closely-packed in the proximity of Ag nanoisland films for controlling emission linewidth, peak, and intensity,” *Optics Express* **15**, 14289-14298 (2007).

- S. Tek, **E. Mutlugun**, I. M. Soganci, N. Kosku Perkgoz, D. Yucel, G. Celiker, and H. V. Demir, “Comparative study of optically activated nanocomposites with photocatalytic TiO₂ and ZnO nanoparticles for massive environmental decontamination,” *Journal of Nano Photonics* **1**, 011685 (2007).

- H. V. Demir, S. Nizamoglu, T. Ozel, **E. Mutlugun**, I. O. Huyal, E. Sari, E. Holder, and N. Tian, “White light generation tuned by dual hybridization of nanocrystals and conjugated polymers,” *New Journal of Physics* **9**, 362 (2007).

BIBLIOGRAPHY

[1] A. Miyawaki, A. Sawano, and T. Kogure, "Lighting up cells: labelling proteins with fluorophores," *Nature Cell Biol.*, **5**, Supp. S1–S7 (2003).

[2] Y. Wua, K. Sefaha, H. Liua, R. Wanga, and W. Tana, "DNA aptamer–micelle as an efficient detection/delivery vehicle toward cancer cells," *PNAS*, **107**, 5-10 (2010).

[3] D. G. Duda, K. S. Cohen, D. T. Scadden, and R. K. Jain, "A protocol for phenotypic detection and enumeration of circulating endothelial cells and circulating progenitor cells in human blood," *Nature Protocols*, **2**, 805-810 (2007).

[4] K. Li, Y. Chen, S. Li, H. G. Nguyen, Z. Niu, S. You, C. M. Mello, X. Lu, and Q. Wang, "Chemical Modification of M13 Bacteriophage and Its Application in Cancer Cell Imaging," *Bioconjugate Chem.*, **21**, 1369-1377 (2010).

[5] C. Ornelas, R. Lodescar, A. Durandin, J. W. Canary, R. Pennell, L. F. Liebes, and M. Weck, "Combining Aminocyanine Dyes with Polyamide Dendrons: A Promising Strategy for Imaging in the Near-Infrared Region," *Chem.-A Euro. J.*, **17**, 3619–3629 (2011).

[6] U. R. Genger, M. Grabolle, S. C. Jaricot, R. Nitschke, and T. Nann, "Quantum dots versus organic dyes as fluorescent labels," *Nature Methods*, **5**, 763 (2008).

- [7] I. Medintz and H. Mattoussi, "Quantum dot based resonance energy transfer and its growing application in biology," *Phys.Chem. Phys*, **11**, 17-45 (2009).
- [8] E. A. J. Erijman and T. M. Jovin, "FRET imaging," *Nature Biotech.*, **21**, 1387-1395 (2003).
- [9] R. Rossetti, S. Nakahara, and Brus, L. "Quantum size effects in the redox potentials, resonance Raman spectra, and electronic spectra of CdS crystallites in aqueous solution," *The Journal of Chem. Phys.*, **79**, 1086-1088 (1983).
- [10] W.C.W. Chan, S. Nie, "Quantum Dot Bioconjugates for Ultrasensitive Nonisotopic Detection," *Science*, **281**, 2016 (1998).
- [11] X. Gao, L. Yang, J. A. Petros, F. F. Marshall, J. W. Simons, S. Nie, "In vivo molecular and cellular imaging with quantum dots," *Curr. Opin. Biotech.*, **16**, 63 (2005).
- [12] J. Tang, K. W. Kemp, S. Hoogland, K. S. Jeong, H. Liu, L. Levina, M. Furukawa, X. Wang, R. Debnath, D. Cha, K. W. Chou, A. Fischer, A. Amassian, J. B. Asbury, and E. H. Sargent, "Colloidal-Quantum-Dot Photovoltaics Using AtomicLigand Passivation," *Nature Mater.* **10**, 765-771 (2011).
- [13] J. M. Caruge, J. E. Halpert, V. Wood, V. Bulovic, and M. G. Bawendi, "Colloidal quantum-dot light-emitting diodes with metal-oxide charge transport layers," *Nature Photonics*, **2**, 247 - 250 (2008).
- [14] X. Michalet, F. F. Pinaud, L. A. Bentolila, J. M. Tsay, S. Doose, J. J. Li, G. Sundaresan, A. M. Wu, S. S. Gambhir, and S. Weiss, "Quantum Dots for Live Cells, in Vivo Imaging, and Diagnostics," *Science*, **307**, 538-544 (2005).

- [15] A. C. S. Samia, X. Chen, and C. Burda, "Semiconductor Quantum Dots for Photodynamic Therapy," *J. A. C. S.*, **125**, 15736-1573 (2003).
- [16] C. B. Murray, D. J. Norris, and M. G. Bawendi, "Synthesis and characterization of nearly monodisperse CdE (E= sulfur, selenium, tellurium) semiconductor nanocrystallites," *J. A. C. S.*, **115**, 8706 (1993).
- [17] A. P. Alivisatos, "Semiconductor Clusters, Nanocrystals, and Quantum Dots," *Science*, **271**, 933-937 (1996).
- [18] M. A. Green, *Third Generation Photovoltaics: Advanced Solar Energy Conversion*, Springer, 2005.
- [19] W. Huynh, J. Dittmer, W. Libby, G. Whiting, and A. Alivisatos, "Controlling the Morphology of Nanocrystal-Polymer Composites for Solar Cells," *Adv. Funct. Mater.*, **13**, 73-79 (2003).
- [20] J. M. Luther, M. Law, M. C. Beard, Q. Song, M. O. Reese, R. J. Ellingson, and A. J. Nozik, "Schottky Solar Cells Based on Colloidal Nanocrystal Films" *Nano Lett.* **8**, 3488 (2008).
- [21] H. Liu, J. Tang, I. J. Kramer, R. Debnath, G. I. Koleilat, X. Wang, A. Fisher, R. Li, L. Brzozowski, L. Levina, and E. H. Sargent, "Electron Acceptor Materials Engineering in Colloidal Quantum Dot Solar Cells" *Adv. Mater.* **23**, 3832-3837 (2011).
- [22] H. J. Lee, J. H. Yum, H. C. Leventis, S. M. Zakeeruddin, S. A. Haque, P. Chen, S. I. Seok, M. Grätzel, and M. K. Nazeeruddin, "CdSe Quantum Dot-Sensitized Solar Cells Exceeding Efficiency 1% at Full-Sun Intensity" *J. Phys. Chem. C* **112**, 11600 (2008).

- [23] Q. Shen, J. Kobayashi, L. J. Diguna, T. Toyoda, “Effect of ZnS coating on the photovoltaic properties of CdSe quantum dot-sensitized solar cells” *J. Appl. Phys.* **103**, 084304 (2008).
- [24] Z. Quanxin, G. Xiaozhi, H. Xiaoming, S. Huang, D. Li, Y. Luo, Q. Shen, T. Toyoda, and Q. Meng, “Highly efficient CdS/CdSe-sensitized solar cells controlled by the structural properties of compact porous TiO₂ photoelectrodes,” *Phys. Chem. Chem. Phys.* **13**, 4659-4667 (2011).
- [25] V. L. Colvin, M. C. Schlamp, and A. P. Alivisatos, “Light-emitting diodes made from cadmium selenide nanocrystals and a semiconducting polymer,” *Nature* **370**, 354 (1994).
- [26] H. Mattoussi, L. H. Radzilowski, B. O. Dabbousi, E. L. Thomas, M. G. Bawendi, and M. F. Rubner, “Electroluminescence from heterostructures of poly (phenylene vinylene) and inorganic CdSe nanocrystals,” *J. Appl. Phys.* **83**, 7965 (1998).
- [27] S. Coe, W. K. Woo, M. G. Bawendi, and V. Bulovic, “Electroluminescence from single monolayers of nanocrystals in molecular organic devices,” *Nature* **420**, 800 (2002).
- [28] J. S. Steckel, P. Snee, S. Coe-Sullivan, J. P. Zimmer, J. E. Halpert, P. Anikeeva, L. A. Kim, V. Bulovic, and M. G. Bawendi, “Color-Saturated Green-Emitting QD-LEDs,” *Angew. Chem. Int. Edt.* **45**, 5796–5799 (2006).
- [29] P. O. Anikeeva, J. E. Halpert, M. G. Bawendi, and V. Bulovic “Quantum Dot Light-Emitting Devices with Electroluminescence Tunable over the Entire Visible Spectrum” *Nano Lett.* **9**, 2532–2536 (2009).

- [30] S. Nizamoglu, T. Ozel, E. Sari, and H. V. Demir, "White light generation using CdSe/ZnS core-shell nanocrystals hybridized with InGaN/GaN light emitting diodes," *Nanotechnology* **18**, 065709 (2007).
- [31] S. Jun, H. Jang, J. Lim, B. Kim, and Y. Kim, "White-Light-Emitting Diodes with Quantum Dot Color Converters for Display Backlights," *Adv. Mater.* **22**, 3076–3080 (2010).
- [32] T. H. Kim, K. S. Cho, E. K. Lee, S. J. Lee, J. Chae, J. W. Kim, D. H. Kim, J. Y. Kwon, G. Amaratunga, S. Y. Lee, B. L. Choi, Y. Kuk, J. M. Kim, and K. Kim, "Full-colour quantum dot displays fabricated by transfer printing," *Nature Photon.* **5**, 176–182 (2011).
- [33] B. Dubertret, P. Skourides, D. J. Norris, V. Noireaux, A. H. Brivanlou, A. Libchaber, "In vivo imaging of quantum dots encapsulated in phospholipid micelles," *Science* **298**, 1759–1762 (2002).
- [34] W. Guo, J. J. Li, Y. A. Wang, and X. Peng, "Conjugation chemistry and bioapplications of semiconductor box nanocrystals prepared via dendrimer bridging," *Chem. Mater.* **15**, 3125–3133 (2003).
- [35] S. Kim and M. G. Bawendi, "Oligomeric ligands for luminescent and stable nanocrystal quantum dots," *J. A. C. S.* **125**, 14652–14653 (2003).
- [36] S. Jacobs, V. Subramaniam, A. Schonle, T. M. Jovin, S. W. Hell, "EGFP and DsRed expressing cultures of Escherichia coli imaged by confocal, two photon and fluorescence lifetime microscopy," *FEBS Lett.* **479**, 131-135 (2000).

- [37] M. Y. Han, X. Gao, J. Z. Su, S. M. Nie, "Quantum-dot-tagged microbeads for multiplexed optical coding of biomolecules," *Nature Biotech.* **19**, 631-635 (2001).
- [38] W. C. Chan, D. J. Maxwell, X. Gao, R. E. Bailey, M. Han, S. Nie, "Luminescent quantum dots for multiplexed biological detection and imaging," *Curr. Opin. Biotechnol* **13**, 40–46 (2002).
- [39] B. Atmaja, B. H. Lui, Y. Hu, S. E. Beck, C. W. Frank, and J. R. Cochran, "Targeting of Cancer Cells Using Quantum Dot–Polypeptide Hybrid Assemblies That Function as Molecular Imaging Agents and Carrier Systems," *Adv. Funct. Mater.* **20**, 4091–4097 (2010).
- [40] X. Gao, Y. Cui, R. M. Levenson, L. W. K. Chung, and S. Nie, "In vivo cancer targeting and imaging with semiconductor quantum dots," *Nature Biotech.* **22**, 969 - 976 (2004).
- [41] X. Wu, H. Liu, J. Liu, K. N. Haley, J. A. Treadway, J. P. Larson, N. Ge, F. Peale, and M. P. Bruchez, "Immunofluorescent labeling of cancer marker Her2 and other cellular targets with semiconductor quantum dots," *Nature Biotech.* **21**, 41 - 46 (2002).
- [42] S. Pathak, E. Cao, M. C. Davidson, S. Jin, and G. A. Silva, "Quantum dot applications to neuroscience: new tools for probing neurons and glia," *J. Neurosci* **26**, 1893–1895 (2006).
- [43] N. G. Portney and M. Ozkan, "Nano-oncology: drug delivery, imaging, and sensing," *Anal. Bioanal. Chem.* **384**, 620–630 (2006).

- [44] B. I. Ipe, M. Lehnig, and C. M. Niemeyer, "On the generation of free radical species from quantum dots," *Small* **1**, 706–709 (2005).
- [45] K. E. Sapsford, L. Berti, I. L. Medintz, "Materials for fluorescence energy transfer analysis beyond traditional donor-acceptor combinations," *Angew. Chem. Int. Edn.*, **45**, 4562-4588 (2006).
- [46] I. L. Medintz, A. R. Clapp, H. Mattoussi, E. R. Goldman, B. Fisher, and J. M. Mauro, "Self-assembled nanoscale biosensors based on quantum dot FRET donors," *Nature Mat.*, **2**, 630 (2003).
- [47] A. R. Clapp, I. L. Medintz, B. R. Fisher, G.P. Anderson, and H. Mattoussi, "Can Luminescent Quantum Dots Be Efficient Energy Acceptors with Organic Dye Donors?," *J. A. C. S.*, **127**, 1242–1250 (2005).
- [48] R. Gill, I. Willner, I. Shweky, and U. Banin, "Fluorescence Resonance Energy Transfer in CdSe/ZnS-DNA Conjugates: Probing Hybridization and DNA Cleavage," *J. Phys. Chem. B*, **109**, 23715 (2005).
- [49] U. O. S. Seker, T. Ozel, and H. V. Demir, "Peptide-Mediated Constructs of Quantum Dot Nanocomposites for Enzymatic Control of Nonradiative Energy Transfer," *Nano Letters*, **11**, 1530-1539 (2011).
- [50] H. Liu, G. Liang, E. S. Abdel-Halim, and J. J. Zhu, "A sensitive and selective quantum dots-based FRET biosensor for the detection of cancer marker type IV collagenase," *Anal. Methods*, **3**, 1797-1801(2011).

- [51] P. T. Snee, R. C. Somers, G. Nair, J. P. Zimmer, M. G. Bawendi, and D. G. Nocera, "A Ratiometric CdSe/ZnS Nanocrystal pH Sensor," *J. A. C. S.* **128**, 13320 (2006).
- [52] A. R. Clapp, I. L. Medintz, H. T. Uyeda, B. R. Fisher, E. R. Goldman, M. G. Bawendi, and H. Mattoussi, "Quantum Dot-Based Multiplexed Fluorescence Resonance Energy Transfer," *J. A. C. S.*, **127**, 18212 (2005).
- [53] V. Bagalkot, L. Zhang, E. Levy-Nissenbaum, S. Jon, P. W. Kantoff, R. Langer, and O. C. Farokhzad, "Quantum dot -Aptamer conjugates for synchronous cancer imaging, therapy, and sensing of drug delivery based on Bi-fluorescence resonance energy transfer," *Nano Letters*, **7**, 3065 (2007).
- [54] G. Jiang, A. S. Susha, A. A. Lutich, F. D. Stefani, J. Feldmann, and A. L. Rogach, "Cascaded FRET in Conjugated Polymer/Quantum Dot/Dye-Labeled DNA Complexes for DNA Hybridization Detection," *ACS Nano*, **3**, 4127–4131 (2009).
- [55] N. Cicek, S. Nizamoglu, T. Ozel, E. Mutlugun, D. U. Karatay, V. Lesnyak, T. Otto, N. Gaponik, A. Eychmüller, and H. V. Demir, "Structural tuning of color chromaticity through nonradiative energy transfer by interspacing CdTe nanocrystal monolayers," *Appl. Phys. Lett.*, **94**, 061105 (2009).
- [56] S.V. Gaponenko, "Optical Properties of Semiconductor Nanocrystals," Cambridge (1998).
- [57] L. Brus, "Electronic wave functions in semiconductor clusters: experiment and theory," *J. Phys. Chem.*, **90**, 2555-2560 (1986).
- [58] Z. A. Peng and X. Peng, "Formation of High-Quality CdTe, CdSe, and CdS Nanocrystals Using CdO as Precursor," *J. A. C. S.*, **123**, 183-184 (2001).

- [59] A. M. Kapitonov, A. P. Stupak, S. V. Gaponenko, E. P. Petrov, A. L. Rogach, and A. Eychmüller, “Luminescence Properties of Thiol-Stabilized CdTe Nanocrystals,” *J. Phys. Chem. B*, **103**, 10109–10113 (1999).
- [60] L. Qu, Z. A. Peng, and X. Peng, “Alternative Routes toward High Quality CdSe Nanocrystals,” *Nano Lett.*, **1**, 333–337 (2001).
- [61] W. W. Yu, and X. Peng, “Formation of High-Quality CdS and Other II–VI Semiconductor Nanocrystals in Noncoordinating Solvents: Tunable Reactivity of Monomers,” *Angew. Chem. Int. Edt.*, **41**, 2368–2371 (2002).
- [62] O. I. Micic, C. J. Curtis, K. M. Jones, J. R. Sprague, and A. J. Nozik, “Synthesis and Characterization of InP Quantum Dots,” *J. Phys. Chem.*, **98**, 4966–4969 (1994).
- [63] D. Battaglia and X. Peng, “Formation of high quality InP and InAs nanocrystals in a noncoordinating solvent,” *Nano Lett.*, **2**, 1027–1030 (2002).
- [64] M.A Hines and P. G. Sionnest, “Bright UV-blue luminescent colloidal ZnSe nanocrystals,” *Journal of Phys. Chem. B*, **102**, 3655–3657 (1998).
- [65] L.S. Li, N. Pradhan, Y. Wang, and X. Peng, “High quality ZnSe and ZnS nanocrystals formed by activating zinc carboxylate precursors,” *Nano Lett.*, **4**, 2261–2264 (2004).
- [66] W. W. Yu, J. C. Falkner, B.S. Shih and V. L. Colvin, “Preparation and characterization of monodisperse PbSe semiconductor nanocrystals in a noncoordinating solvent,” *Chem. Mater.*, **16**, 3318–3322 (2004).

- [67] M. A. Hines and G. D. Scholes, “Colloidal PbS nanocrystals with size-tunable near-infrared emission: observation of post-synthesis self-narrowing of the particle size distribution,” *Adv. Mater.*, **15**, 1844–1849 (2003).
- [68] S. Haubold, M. Haase, A. Kornowski, and H. Weller, “Strongly luminescent InP/ZnS core-shell nanoparticles,” *Chem. Phys. Chem.*, **2**, 331–334 (2001).
- [69] D. V. Talapin, R. Koeppel, S. Götzinger, A. Kornowski, J. M. Lupton, A. L. Rogach, O. Benson, J. Feldmann, and H. Weller, “Highly Emissive Colloidal CdSe/CdS Heterostructures of Mixed Dimensionality,” *Nano Lett.*, **3**, 1677–1681 (2003).
- [70] D. V. Talapin, A. L. Rogach, A. Kornowski, M. Haase, and H. Weller, “Highly Luminescent Monodisperse CdSe and CdSe/ZnS Nanocrystals Synthesized in a Hexadecylamine–Trioctylphosphine Oxide–Trioctylphosphine Mixture,” *Nano Lett.*, **1**, 207–211, (2001).
- [71] T. M. Inerbaev, A. E. Masunov, S. I. Khondaker, A. Dobrinescu, A. V. Plamadă and Y. Kawazoe, “Quantum chemistry of quantum dots: Effects of ligands and oxidation,” *J. Chem. Phys.*, **131**, 044106 (2009).
- [72] I. Nabiev, S. Mitchell, A. Davies, Y. Williams, D. Kelleher, R. Moore, Y. K. Gun’ko, S. Byrne, Y. P. Rakovich, J. F. Donegan, A. Sukhanova, J. Conroy, D. Cottell, N. Gaponik, A. Rogach, Y. Volkov, “Nonfunctionalized nanocrystals can exploit a cell’s active transport machinery delivering them to specific nuclear and cytoplasmic compartments,” *Nano Lett.*, **7**, 3452–3461 (2007).
- [73] A. L. Rogach, “Semiconductor Nanocrystal Quantum Dots,” Springer (2008).

[74] N. Gaponik, D. V. Talapin, A. L. Rogach, K. Hoppe, E. V. Shevchenko, A. Kornowski, A. Eychmüller, and H. Weller, “Thiol-Capping of CdTe nanocrystals: An alternative to organometallic synthetic routes,” *J. Phys. Chem. B*, **106**, 7177-7185 (2002).

[75] A. L. Rogach, T. Franzl, T. A. Klar, J. Feldmann, N. Gaponik, V. Lesnyak, A. Shavel, A. Eychmüller, Y. P. Rakovich, and J. F. Donegan, “Aqueous synthesis of thiol-capped CdTe nanocrystals: State-of-the-art,” *J. Phys. Chem. C*, **111**, 14628-14637 (2007).

[76] A. Shavel, N. Gaponik, and A. Eychmüller, “Covalent Linking of CdTe Nanocrystals to Amino-Functionalized Surfaces,” *Chem. Phys. Chem*, **6**, 449–451 (2005).

[77] B. Güzeltürk, E. Mutlugün, X. Wang, K. L. Pey and H. V. Demir, “Photovoltaic nanopillar radial junction diode architecture enhanced by integrating semiconductor quantum dot nanocrystals as light harvesters,” *App. Phys. Lett.*, **97**, 093111 (2010).

[78] W. Liu, A. B. Greytak, J. Lee, C. R. Wong, J. Park, L. F. Marshall, W. Jiang, P. N. Curtin, A. Y. Ting, D. G. Nocera, D. Fukumura, R. K. Jain, and M. G. Bawendi, “Compact Biocompatible Quantum Dots via RAFT-Mediated Synthesis of Imidazole-Based Random Copolymer Ligand,” *J. A. C. S.*, **132**, 472–483 (2010).

[79] L. Li and P. Reiss, “One-pot Synthesis of Highly Luminescent InP/ZnS Nanocrystals without Precursor Injection,” *J. A. C. S.*, **130**, 11588-9 (2008).

- [80] J. Ziegler, S. Xu, E. Kucur, F. Meister, M. Batentschuk, F. Gindele, and T. Nann, "Silica-Coated InP/ZnS Nanocrystals as Converter Material in White LEDs," *Adv. Mater.*, **20**, 4068-4073 (2008).
- [81] H. Fu and A. Zunger, "InP quantum dots: Electronic structure, surface effects, and the redshifted emission," *Phys. Rev. B*, **56**, 1496–1508 (1997).
- [82] B. Valeur, "Molecular Fluorescence," Wiley (2002).
- [83] Robert M Clegg, "The vital contributions of Perrin and Förster," *Biophotonics Int.*, **11**, 42 (2004).
- [84] K. H. Drexhage, "Fluorescence efficiency of laser dye," *J. Res. Natl. Bur. Stand.A*, **80A**, 421– 428 (1976).
- [85] M. Grabolle, M. Spieles, V. Lesnyak, N. Gaponik, A. Eychmüller, and U. Resch-Genger, "Determination of the Fluorescence Quantum Yield of Quantum Dots: Suitable Procedures and Achievable Uncertainties," *Anal. Chem.*, **81**, 6285-6294 (2009).
- [86] R. Tsien, "Constructing and Exploiting the Fluorescent Protein Paintbox (Nobel Lecture)," *Angew. Chem. Int. Edt.*, **48**, 5612 (2009).
- [87] A .Y Gorokhovatsky, V. V. Marchenkov, N. V. Rudenko, T. V. Ivashina, V. N. Ksenzenko, N. Burkhardt, G. V. Semisotnov, L. M. Vinokurov, Y. B. Alakhov, "Fusion of *Aequorea victoria* GFP and aequorin provides their Ca²⁺-induced interaction that results in red shift of GFP absorption and efficient bioluminescence energy transfer," *Biochem. Biophys. Res. Commun.*, **320**, 703 (2004).

- [88] S. K. Deo, M. Mirasoli, S. Daunert, "Bioluminescence resonance energy transfer from aequorin to a fluorophore: an artificial jellyfish for applications in multianalyte detection," *Anal. Bioanal. Chem.*, **381**, 1387 (2005).
- [89] A. M. Dennis and G. Bao, "Quantum Dot-Fluorescent Protein Pairs as Novel Fluorescence Resonance Energy Transfer Probes," *Nano Lett.*, **8**, 1439 (2008).
- [90] V. R. Hering, G. Gibson, R. I. Schumacher, A. F. Alario, and M. J. Politi, "Energy Transfer between CdSe/ZnS Core/Shell Quantum Dots and Fluorescent Proteins," *Bioconjugate Chem.*, **18**, 1705 (2007).
- [91] V. Lesnyak, A. Plotnikov, N. Gaponik, and A. Eychmüller, "Toward efficient blue-emitting thiol-capped $Zn_{1-x}Cd_xSe$ nanocrystals," *J. Mater. Chem.*, **18**, 5142 (2008).
- [92] E. Yuca, A. Y. Karatas, U. O. S. Seker, M. Gungormus, G. D. Doganay, M. Sarikaya, C. Tamerler, "In Vitro Labeling of Hydroxyapatite Minerals by an Engineered Protein," *Biotech and Bioeng.*, **108**, 1021 (2011).
- [93] U. O. S. Seker, B. Wilson, D. Sahin, C. Tamerler, and M. Sarikaya, "Quantitative Affinity of Genetically Engineered Repeating Polypeptides to Inorganic Surfaces," *Biomacromolecules*, **10**, 250 (2009).
- [94] Lakowicz, J. R., *Principles of fluorescence spectroscopy*; Springer: New York, 2006.
- [95] PDB Protein Data Bank
<http://www.rcsb.org/pdb/explore/explore.do?structureId=1EMA>

- [96] C. A. Blanco, O. Perera, J. D. Ray, E. Taliercio, and L. Williams III, "Incorporation of rhodamine B into male tobacco budworm moths *Heliothis virescens* to use as a marker for mating studies," *J. Insect Sci.*, **6**, 1-10 (2006).
- [97] K. E. Sapsford, L. Berti, and I. L. Medintz, "Fluorescence Spectroscopy: Applications in Chemical Biology in Wiley Encyclopedia of Chemical Biology," John Wiley Sons Inc., (2008).
- [98] A. Waggoner, "Fluorescent labels for proteomics and genomics," *Curr. Opin. Chem. Biol.*, **10**, 62 (2006).
- [99] B. I. Stepanov and A. N. Rubinov, "Stimulated optical emission of organic dye solutions," *Zhu. Pri. Spek.* **7**, 507-521 (1967).
- [100] F. P. Schafer, "Organic Dyes in Laser Technology," *Angew. Chem. Int. Edt.*, **9**, 9-25 (1970).
- [101] P. M. W. French, A. S. L. Gomes, A. S. Gouvela-Neto, and J. R. Taylor, "A femtosecond hybrid mode locked Rhodamine B dye laser," *Optics Comm.*, **59**, 366 (1986).
- [102] F. Muller, S. Gotzinger, N. Gaponik, H. Weller, J. Mlynek, and O. Benson, "Investigation of Energy Transfer between CdTe Nanocrystals on Polystyrene Beads and Dye Molecules for FRET-SNOM Applications," *J. Phys. Chem. B* **108**, 14527 (2004).
- [103] E. Alphantery, L. M. Walsh, Y. Rakovic, A. L. Bradley, J.F. Donegan, and N. Gaponik, "Highly efficient Förster resonance energy transfer between CdTe nanocrystals and Rhodamine B in mixed solid films," *Chem. Phys. Lett.*, **388**, 100 (2004).

- [104] Q. Chen, Q. Ma, Y. Wan, X. Su, Z. Lin, and Q. Jin, "Studies on fluorescence resonance energy transfer between dyes and water-soluble quantum dots," *Luminescence*, **20**, 251 (2005).
- [105] D. M. Willard, L. L. Carillo, J. Jung, and A. V. Orden, "CdSe-ZnS quantum dots as resonance energy transfer donors in a model protein-protein binding assay," *Nano Lett.*, **1**, 469 (2001).
- [106] A. R. Clapp, I. L. Medintz, J. M. Mauro, B. R. Fisher, M. G. Bawendi, and H. Mattoussi, "Fluorescence Resonance Energy Transfer Between Quantum Dot Donors and Dye-Labeled Protein Acceptors," *J. A. C. S.*, **126**, 301 (2004).
- [107] A. R. Clapp, I. L. Medintz, and H. Mattoussi, "Förster Resonance Energy Transfer Investigations Using Quantum-Dot Fluorophores," *Chem. Phys. Chem.*, **7**, 47 (2006).
- [108] S. Sadhu and A. Patra, "Donor-Acceptor Systems: Energy Transfer from CdS Quantum Dots/Rods to Nile Red Dye," *Chem. Phys. Chem.*, **9**, 2052 (2008).
- [109] P. S. Chowdhury, P. Sen, and A. Patra, "Optical properties of CdS nanoparticles and the energy transfer from CdS nanoparticles to Rhodamine 6G," *Chem. Phys. Lett.*, **413**, 311 (2005).
- [110] S. Nizamoglu and H. V. Demir, "Resonant nonradiative energy transfer in CdSe/ZnS core/shell nanocrystal solids enhances hybrid white light emitting diodes," *Opt. Express*, **16**, 13961 (2008).

- [111] S. Mayilo, J. Hilhorst, A. S. Susha, C. Höhl, T. Franzl, T. A. Klar, A. L. Rogach, and J. Feldmann, "Energy Transfer in Solution-Based Clusters of CdTe Nanocrystals Electrostatically Bound by Calcium Ions," *J. Phys. Chem. C*, **112**, 14589 (2008).
- [112] B. O'Reagen and M. Grätzel, "A low-cost, high-efficiency solar cell based on dye-sensitized colloidal TiO₂ films," *Nature*, **353**, 737-740 (1991).
- [113] S. L. Li, K. J. Jiang, K. F. Shao, and L. M. Yang, "Novel organic dyes for efficient dye-sensitized solar cells," *Chem. Comm.*, **26**, 2792-2794 (2006).
- [114] E. Mutlugun, S. Nizamoglu, and H. V. Demir, "Highly efficient nonradiative energy transfer using charged CdSe/ZnS nanocrystals for light-harvesting in solution," *Appl. Phys. Lett.*, **95**, 033106 (2009).
- [115] W. W. Yu, E. Chang, R. Drezek, and V. L. Colvin, "Water-soluble quantum dots for biomedical applications," *Biochem. and Biophys. Res. Comm.*, **348**, 781-786 (2006).
- [116] T. Förster, "Zwischenmolekulare Energiewanderung und Fluoreszenz," *Ann. der Phys.*, **2**, 55 (1948).
- [117] D. M. Willard and A. V. Orden, "Resonant energy-transfer sensor," *Nature Mater.*, **2**, 575-576 (2003).
- [118] I. L. Medintz, A. R. Clapp, F. M. Brunel, T. Tiefenbrunn, H. T. Uyeda, E. L. Chang, J. R. Deschamps, P. E. Dawson, and H. Mattoussi, "Proteolytic activity monitored by fluorescence resonance energy transfer through quantum-dot-peptide conjugates," *Nature Mater.*, **5**, 581-589 (2006).

- [119] J. Li, F. Mei, W. Y. Li, X. W. He, and Y. K. Zhang, "Study on the fluorescence resonance energy transfer between CdTe QDs and butyl-rhodamine B in the presence of CTMAB and its application on the detection of Hg(II)," *Spectrochimica Acta*, **70A**, 811-817 (2008).
- [120] V. K. Komarala, A. L. Bradley, Y. P. Rakovich, S. J. Byrne, Y. K. Gun'ko, and A. L. Rogach, "Surface plasmon enhanced Förster resonance energy transfer between the CdTe quantum dots," *Appl. Phys. Lett.*, **93**, 123102 (2008).
- [121] S. Chanyawadee, R. T. Harley, M. Henini, D. V. Talapin, and P. G. Lagoudakis, "Photocurrent Enhancement in Hybrid Nanocrystal Quantum-Dot p-i-n Photovoltaic Devices," *Phys. Rev. Lett.*, **102**, 077402 (2009).
- [122] E. Jang, S. Jun, H. Jang, J. Lim, B. Kim, and Y. Kim, "White-light-emitting diodes with quantum dot color converters for display backlights," *Adv. Mater.* **22**, 3076-3080 (2010).
- [123] T. Erdem and H. V. Demir, "Semiconductor nanocrystals as rare earth alternatives," *Nature Photonics*, **5**, 126 (2011).
- [124] G. Konstantatos, I. Howard, A. Fischer, S. Hoogland, J. Clifford, E. Klem, L. Levina, and E. H. Sargent, "Ultrasensitive solution-cast quantum dot photodetectors," *Nature*, **442**, 180 (2006).
- [125] J. Lee, V. C. Sundar, J. R. Heine, M. G. Bawendi, and K. F. Jensen, "Full Color Emission from II-VI Semiconductor Quantum Dot-Polymer Composites," *Adv. Mater.*, **12**, 1102-1110 (2000).

- [126] H. Zhang, C. Wang, M. Li, J. Zhang, G. Lu, Yang, and B. Yang, "Fluorescent Nanocrystal-Polymer Complexes with Flexible Processability," *Adv. Mater.*, **17**, 853-857 (2005).
- [127] M. C. Neves, M. A. Martins, P. C. R. Soares-Santos, P. Rauwel, R. A. S. Ferreira, T. Monteiro, L. D. Carlos, T. Trindade, "Photoluminescent, transparent and flexible di-ureasil hybrids containing CdSe/ZnS quantum dots," *Nanotechnology*, **19**, 155601 (2008).
- [128] H. M. Xiong, Z. D. Wang, D. P. Liu, J. S. Chen, Y. G. Wang, and Y. Y. Xia, "Bonding Polyether onto ZnO Nanoparticles: An Efficient Method for Preparing Polymer Nanocomposites with Tunable Luminescence and Stable Conductivity," *Adv. Func. Mater.*, **15**, 1751-1756 (2005).
- [129] J. A. Rogers, Z. Bao, K. Baldwin, A. Dodabalapur, B. Crone, V. R. Raju, V. Kuck, H. Katz, K. Amundson, J. Ewing, and P. Drzaic, "Paper-like electronic displays: Large-area rubberstamped plastic sheets of electronics and microencapsulated electrophoretic inks," *P. N. A. S.*, **98**, 4835-4840 (2001).
- [130] H. Tetsuka, T. Ebina, F. Mizukami, "Highly Luminescent Flexible Quantum Dot-Clay Films," *Adv. Mater.*, **20**, 3039-3043 (2008).
- [131] Y. A. Yang, H. Wu, K. R. Williams, Y. C. Cao, "Synthesis of CdSe and CdTe Nanocrystals without Precursor Injection," *Angew. Chem Int. Edt.*, **117**, 6870-6873 (2005).
- [132] A. Z. Peng and X. Peng, "Formation of High-Quality CdTe, CdSe, and CdS Nanocrystals Using CdO as Precursor," *J. A. C. S.*, **123**, 183-184 (2001).

- [133] N. Gaponik, D. V. Talapin, A. L. Rogach, K. Hoppe, E. V. Shevchenko, A. Kornowski, A. Eychmüller, and H. Weller, "Thiol-Capping of CdTe Nanocrystals: An Alternative to Organometallic Synthetic Routes," *J. Phys. Chem. B*, **106**, 7177-7185 (2002).
- [134] B. O. Dabbousi, J. R. Viejo, F. V. Mikulec, J. R. Heine, H. Mattoussi, R. Ober, K. F. Jensen, and M. G. Bawendi, "(CdSe)ZnS Core-Shell Quantum Dots: Synthesis and Characterization of a Size Series of Highly Luminescent Nanocrystallites," *J. Phys. Chem. B*, **101**, 9463-9475 (1997).
- [135] E. Ryu, S. Kim, E. Jang, S. Jun, H. Jang, B. Kim, and S. W. Kim, "Step-Wise Synthesis of InP/ZnS Core-Shell Quantum Dots and the Role of Zinc Acetate," *Chem. Mat.*, **21**, 2425-2427 (2009).
- [136] R. Xie, D. Battaglia, and X. Peng, "Colloidal InP Nanocrystals as Efficient Emitters Covering Blue to Near-Infrared," *J. A. C. S.*, **129**, 15432-15433 (2007).
- [137] U. T. D. Thuy, P. T. Thuy, N. Q. Liem, L. Li, and P. Reiss, "Comparative photoluminescence study of close-packed and colloidal InP/ZnS quantum dots," *Appl. Phys. Lett.*, **96**, 073102 (2010).
- [138] T. T. Pham, T. K. C. Tran, and Q. L. Nguyen, "Temperature-dependent photoluminescence study of InP/ZnS quantum dots," *Adv. Nat. Sci.: Nanosci. and Nanotech.*, **2**, 025001 (2011).
- [139] U. T. D. Thuy, P. Reiss, and N. Q. Liem, "Luminescence properties of In(Zn)P alloy core/ZnS shell quantum dots," *Appl. Phys. Lett.*, **97**, 193104 (2010).

- [140] S. Gao, C. Zhang, Y. Liu, H. Su, L. Wei, T. Huang, N. Dellas, S. Shang, S. E. Mohny, J. Wang, and J. Xu, "Lasing from colloidal InP/ZnS quantum dots," *Opt. Exp.* **19**, 5528-35 (2011).
- [141] K. T. Yong, H. Ding, I. Roy, W. C. Law, E. J. Bergey, A. Maitra, and P. N. Prasad, "Imaging Pancreatic Cancer Using Bioconjugated InP Quantum Dots," *ACS Nano*, **3**, 502-10 (2009).
- [142] S. W. Rosencrance, W. K. Way, N. Winograd, and D. A. Shirley, "Polymethylmethacrylate by XPS," *Surf. Sci. Spectra*, **2**, 71 (2008).
- [143] W. Y. Chen, A. V. Ghule, J. Y. Chang, B.Y. Chen, J. Y. Liu, S. H. Tzing, and Y.C. Ling, "Synthesis, characterization, photo and physicochemical properties of 11-mercaptoundecanoic acid and tetraaniline capped CdS quantum dots," *Mater. Chem. and Phys.*, **123**, 742 (2010).
- [144] E. Mutlugun, O. Samarskaya, T. Ozel, N. Cicek, N. Gaponik, A. Eychmüller, and H. V. Demir, "Highly efficient nonradiative energy transfer mediated light harvesting in water using aqueous CdTe quantum dot antennas," *Opt. Exp.*, **18**, 10720-30 (2010).
- [145] K. Boeneman, B. C. Mei, A. M. Dennis, G. Bao, J. R. Deschamps, H. Mattoussi, and I. L. Medintz, "Sensing Caspase 3 Activity with Quantum Dot-Fluorescent Protein Assemblies," *J. A. C. S.*, **131**, 3828-3829 (2009).
- [146] R. Freeman, T. Finder, R. Gill, and I. Willner, "Probing Protein Kinase (CK2) and Alkaline Phosphatase with CdSe/ZnS Quantum Dots," *Nano Lett.*, **10**, 2192-6 (2010).

- [147] C. Higgins, M. Lunz, A. L. Bradley, V. Gerard, S. Byrne, Y. K. Gunko, V. Lesnyak, and N. Gaponik, "Energy transfer in colloidal CdTe quantum dot nanoclusters," *Opt. Exp.* **18**, 24486-94 (2010).
- [148] T. Franzl, D. S. Koktysh, T. A. Klar, A. L. Rogach, J. Feldmann, and N. Gaponik, "Fast energy transfer in layer-by-layer assembled CdTe nanocrystal bilayers," *Appl. Phys. Lett.*, **84**, 2904 (2004).
- [149] J. Lee, A. O. Govorov, and N. A. Kotov, "Bioconjugated Superstructures of CdTe Nanowires and Nanoparticles: Multistep Cascade Forster Resonance Energy Transfer and Energy Channeling," *Nano Lett.*, **5**, 2063 (2005).
- [150] R. Wargnier, A. V. Baranov, V. G. Maslov, V. Stsiapura, M. Artemyev, M. Pluot, A. Sukhanova, and I. Nabiev, "Energy Transfer in Aqueous Solutions of Oppositely Charged CdSe/ZnS Core/Shell Quantum Dots and in Quantum Dot-Nanogold Assemblies," *Nano Lett.*, **4**, 451-457 (2004).
- [151] T. Erdem, S. Nizamoglu, X. W. Sun, and H. V. Demir, "A photometric investigation of ultra-efficient LEDs with high color rendering index and high luminous efficacy employing nanocrystal quantum dot luminophores," *Optics Exp.*, **18**, 340 (2010).
- [152] J. D. Jackson, "Classical Electrodynamics," Wiley (1998).
- [153] X. F. Wang, B. Herman, "Fluorescence Imaging Spectroscopy and Microscopy," John-Wiley Sons (1996).
- [154] H. Kuhn, "Classical Aspects of Energy Transfer in Molecular Systems," *J. Chem. Phys.*, **53**, 101 (1970).

Appendix A

Derivation of FRET based dipole-dipole interaction

In this derivation, our aim is to find the electric field of the oscillating dipole with a dipole moment to obtain the r^{-6} dependence of the Förster-type energy transfer. Starting with the vector potential [152],

$$\vec{A}(x) = \frac{-i\mu_0\omega}{4\pi} \vec{p} \frac{e^{ikr}}{r} \quad \text{A.1}$$

$$\vec{H} = \frac{1}{\mu_0} \nabla \times \vec{A} \quad \text{A.2}$$

$$\vec{H} = \frac{-i\omega}{4\pi} \frac{\partial}{\partial r} \left(\hat{r} \times \vec{p} \frac{e^{ikr}}{r} \right) \quad \text{A.3}$$

Since the unit vector and dipole moment are independent of r , Eqn. A.3 can be written as

$$\vec{H} = \frac{-i\omega}{4\pi} \hat{r} \times \vec{p} \frac{\partial}{\partial r} \left[\frac{e^{ikr}}{r} \right] \quad \text{A.4}$$

And finally given as

$$\vec{H} = \frac{-i\omega}{4\pi} \hat{r} \times \vec{p} \frac{e^{ikr}}{r} \left[ik - \frac{1}{r} \right] \quad \text{A.5}$$

Now, we consider the electric field given as

$$\vec{E} = \frac{iZ_0}{k} (\nabla \times \vec{H}) \quad \text{A.6}$$

where

$$Z_0 = \sqrt{\frac{\mu_0}{\epsilon_0}} \quad \text{A.7}$$

Substituting Eqn. A.5 into Eqn. A.6, we obtain Eqn. A.8 and A.9 as

$$\vec{E} = \frac{i}{k} \sqrt{\frac{\mu_0}{\epsilon_0}} \vec{\nabla} \times \left[\frac{-i\omega}{4\pi} (\hat{r} \times \vec{p}) \frac{e^{ikr}}{r} \left(ik - \frac{1}{r} \right) \right] \quad \text{A.8}$$

$$= \frac{1}{4\pi\epsilon_0 n^2} \left[ik \nabla \times \left(\frac{e^{ikr}}{r} (\hat{r} \times \vec{p}) \right) - \nabla \times \left(\frac{e^{ikr}}{r^2} (\hat{r} \times \vec{p}) \right) \right] \quad \text{A.9}$$

The 1st RHS term of Eqn. A.9 is Eqn. A.10

$$ik \nabla \times \left(\frac{e^{ikr}}{r} (\hat{r} \times \vec{p}) \right) \quad \text{A.10}$$

Using the identity

$$\nabla \times (\vec{A} \times \vec{B}) = (\vec{B} \cdot \nabla) \vec{A} - (\vec{A} \cdot \nabla) \vec{B} + \vec{A} (\nabla \cdot \vec{B}) - \vec{B} (\nabla \cdot \vec{A}) \quad \text{A.11}$$

Eqn. A.10 can be rewritten as Eqn. A.12

$$\nabla \times \left(\frac{e^{ikr}}{r} (\hat{r} \times \vec{p}) \right) = (\vec{p} \cdot \nabla) \frac{e^{ikr}}{r} \hat{r} - \left(\frac{e^{ikr}}{r} \hat{r} \cdot \nabla \right) \vec{p} + \frac{e^{ikr}}{r} \hat{r} (\nabla \cdot \vec{p}) - \vec{p} \left(\nabla \cdot \frac{e^{ikr}}{r} \hat{r} \right) \quad \text{A.12}$$

Since dipole moment is not a vector field, the 2nd and 3rd terms in Eqn. A.12 vanish, and we arrive at Eqn. A.13

$$\nabla \times \left(\frac{e^{ikr}}{r} (\hat{r} \times \vec{p}) \right) = \left(\vec{p} \cdot \nabla \right) \frac{e^{ikr}}{r} \hat{r} - \vec{p} \left(\nabla \cdot \frac{e^{ikr}}{r} \hat{r} \right) \quad \text{A.13}$$

The 1st term in the RHS of Eqn. A.13 can be written as Eqn. A.14

$$\left(\vec{p} \cdot \nabla \right) \frac{e^{ikr}}{r} \hat{r} = \left(p_x \frac{\partial}{\partial x} + p_y \frac{\partial}{\partial y} + p_z \frac{\partial}{\partial z} \right) \frac{e^{ikr}}{r^2} \vec{r} \quad \text{A.14}$$

Using the chain rule

$$\left(\vec{p} \cdot \nabla \right) \frac{e^{ikr}}{r} \hat{r} = \frac{e^{ikr}}{r^2} \left(p_x \frac{\partial}{\partial x} x \hat{i} + p_y \frac{\partial}{\partial y} y \hat{j} + p_z \frac{\partial}{\partial z} z \hat{k} \right) + \vec{r} \left(p_x \frac{\partial}{\partial x} + p_y \frac{\partial}{\partial y} + p_z \frac{\partial}{\partial z} \right) \frac{e^{ikr}}{r^2} \quad \text{A.15}$$

The 1st term in the 2nd RHS term of Eqn. A.15 is Eqn. A.16 as

$$p_x \frac{\partial}{\partial x} \frac{e^{ikr}}{r^2} = p_x \left[\frac{ike^{ikr}}{r^2} \frac{\partial r}{\partial x} + e^{ikr} \frac{\partial}{\partial x} \frac{1}{r^2} \right] \quad \text{A.16}$$

$$= p_x \frac{e^{ikr}}{r^2} \left[ik \frac{\partial r}{\partial x} - \frac{2}{r} \frac{\partial r}{\partial x} \right] \quad \text{A.17}$$

$$p_x \frac{\partial}{\partial x} \frac{e^{ikr}}{r^2} = p_x \frac{e^{ikr}}{r^2} \left[ik \frac{x}{r} - \frac{2}{r} \frac{x}{r} \right] \quad \text{A.18}$$

The 2nd term in the RHS of Eqn. A.15 is written as Eqn. A.19

$$\vec{r} \left(p_x \frac{\partial}{\partial x} + p_y \frac{\partial}{\partial y} + p_z \frac{\partial}{\partial z} \right) \frac{e^{ikr}}{r^2} \quad \text{A.19}$$

$$= \vec{r} \frac{e^{ikr}}{r^2} \left[ik - \frac{2}{r} \right] \left[p_x \frac{x}{r} + p_y \frac{y}{r} + p_z \frac{z}{r} \right] \quad \text{A.20}$$

$$\vec{r} \left(p_x \frac{\partial}{\partial x} + p_y \frac{\partial}{\partial y} + p_z \frac{\partial}{\partial z} \right) \frac{e^{ikr}}{r^2} = \vec{r} \frac{e^{ikr}}{r^2} \left[ik - \frac{2}{r} \right] \frac{\vec{p} \cdot \vec{r}}{r} \quad \text{A.21}$$

$$= \frac{e^{ikr}}{r^2} [ikr - 2] (\vec{p} \cdot \hat{r}) \hat{r} \quad \text{A.22}$$

Then the final expression for Eqn. A.14 is Eqn. A.23 as

$$\Rightarrow \vec{p} \cdot \nabla \frac{e^{ikr}}{r} \hat{r} = \frac{e^{ikr}}{r^2} [ikr - 2] (\vec{p} \cdot \hat{r}) \hat{r} \quad \text{A.23}$$

Working on the 2nd RHS term of Eqn. A.13 we obtain Eqn. A.24 as

$$\vec{p} \left(\nabla \cdot \frac{e^{ikr}}{r} \hat{r} \right) = \frac{1}{r^2} \frac{\partial}{\partial r} (e^{ikr} r) \quad \text{A.24}$$

$$\vec{p} \left(\nabla \cdot \frac{e^{ikr}}{r} \hat{r} \right) = \frac{e^{ikr}}{r^2} [ikr + 1] \quad \text{A.25}$$

Thus Eqn. A.10 is turned into Eqn. A.26

$$\Rightarrow \nabla \times \left(\frac{e^{ikr}}{r} \hat{r} \times \vec{p} \right) = \frac{e^{ikr}}{r^2} \left[\vec{p} + (ikr - 2)(\vec{p} \cdot \hat{r}) \hat{r} - (ikr + 1) \vec{p} \right] \quad \text{A.26}$$

$$\nabla \times \left(\frac{e^{ikr}}{r} \hat{r} \times \vec{p} \right) = \frac{e^{ikr}}{r^2} \left[ikr (\vec{p} \cdot \hat{r}) \hat{r} - 2(\vec{p} \cdot \hat{r}) \hat{r} \right] \quad \text{A.27}$$

Now we switch to the 2nd RHS term of Eqn. A.9, which is given by Eqn. A.28

as

$$\nabla \times \left(\frac{e^{ikr}}{r^2} (\hat{r} \times \vec{p}) \right) \quad \text{A.28}$$

Again using the vector identity Eqn. A.11 and vanishing the terms with derivative of the dipole moment we obtain Eqn. A.28, which is equal to Eqn. A.29

$$(\vec{p} \cdot \nabla) \frac{e^{ikr}}{r^2} \hat{r} - \vec{p} \left(\nabla \cdot \frac{e^{ikr}}{r^2} \hat{r} \right) \quad \text{A.29}$$

The 2nd term of Eqn. A.29 is written as Eqn. A.30

$$\vec{p} \left(\nabla \cdot \frac{e^{ikr}}{r^2} \hat{r} \right) = \vec{p} \frac{e^{ikr}}{r^2} ikr \quad \text{A.30}$$

The 1st term of Eqn. A.29 is given by Eqn. A.31

$$(\vec{p} \cdot \nabla) \frac{e^{ikr}}{r^2} \hat{r} \quad \text{A.31}$$

Using the chain rule, we arrive at Eqn. A.32 as

$$= \frac{e^{ikr}}{r^3} \left[p_x \frac{\partial}{\partial x} + p_y \frac{\partial}{\partial y} + p_z \frac{\partial}{\partial z} \right] \vec{r} + \vec{r} \left[p_x \frac{\partial}{\partial x} + p_y \frac{\partial}{\partial y} + p_z \frac{\partial}{\partial z} \right] \frac{e^{ikr}}{r^3} \quad \text{A.32}$$

The first term of Eqn. A.32 is given by Eqn. A.33

$$\frac{e^{ikr}}{r^3} \left[p_x \frac{\partial}{\partial x} + p_y \frac{\partial}{\partial y} + p_z \frac{\partial}{\partial z} \right] \vec{r} \quad \text{A.33}$$

$$= \frac{e^{ikr}}{r^3} \vec{p} \quad \text{A.34}$$

The 2nd term of Eqn. A.32 is given by Eqn. A.35

$$\vec{r} \left[p_x \frac{\partial}{\partial x} + p_y \frac{\partial}{\partial y} + p_z \frac{\partial}{\partial z} \right] \frac{e^{ikr}}{r^3} \quad \text{A.35}$$

Taking the x derivative only with

$$p_x \frac{\partial}{\partial x} \frac{e^{ikr}}{r^3} \quad \text{A.36}$$

$$= p_x \left[\frac{1}{r^3} ike^{ikr} \frac{\partial r}{\partial x} + e^{ikr} \left(\frac{-3}{r^4} \right) \frac{\partial r}{\partial x} \right] \quad \text{A.37}$$

$$\Rightarrow p_x \frac{\partial}{\partial x} \frac{e^{ikr}}{r^3} = \frac{e^{ikr}}{r^3} (ikr - 3) (\vec{p} \cdot \hat{r}) \hat{r} \quad \text{A.38}$$

Thus,

$$\nabla \times \left(\frac{e^{ikr}}{r^2} (\hat{r} \times \vec{p}) \right) = \frac{e^{ikr}}{r^3} [(ikr - 3) (\vec{p} \cdot \hat{r}) \hat{r} + \vec{p} - ikr\vec{p}] \quad \text{A.39}$$

$$= \frac{e^{ikr}}{r^3} [(1 - ikr) \vec{p} + (ikr - 3) (\vec{p} \cdot \hat{r}) \hat{r}] \quad \text{A.40}$$

Now we go back to Eqn. A.27 and rewrite it as Eqn. A.41

$$\nabla \times \left(\frac{e^{ikr}}{r} (\hat{r} \times \vec{p}) \right) = \frac{e^{ikr}}{r^3} [(1-ikr) \vec{p} + (ikr-3)(\vec{p} \cdot \hat{r}) \hat{r}] \quad \text{A.41}$$

Thus Eqn. A.9 is given as Eqn. A.42

$$\vec{E} = \frac{1}{4\pi\epsilon_0 n^2} \left\{ ik \left[\frac{e^{ikr}}{r^2} (ikr [(\vec{p} \cdot \hat{r}) \hat{r} - \vec{p}] - 2(\vec{p} \cdot \hat{r}) \hat{r}) \right] - \frac{e^{ikr}}{r^3} [(1-ikr) \vec{p} + (ikr-3)(\vec{p} \cdot \hat{r}) \hat{r}] \right\} \quad \text{A.42}$$

In order to separate the radial and the angular components,

since

$$\vec{p} = (\vec{p} \cdot \hat{r}) \hat{r} + (\vec{p} \cdot \hat{\theta}) \hat{\theta} = p \cos \theta \hat{r} - p \sin \theta \hat{\theta} \quad \text{A.43}$$

using

$$3(\vec{p} \cdot \hat{r}) \hat{r} - \vec{p} = 2p \cos \theta \hat{r} + p \sin \theta \hat{\theta} \quad \text{A.44}$$

and

$$\vec{p} - (\vec{p} \cdot \hat{r}) \hat{r} = -p \sin \theta \hat{\theta} \quad \text{A.45}$$

we have

$$\vec{E} = \frac{1}{4\pi\epsilon_0 n^2} \left\{ \frac{e^{ikr}}{r} k^2 (-p \sin \theta \hat{\theta}) - \frac{e^{ikr}}{r^2} (2p \cos \theta \hat{r} + p \sin \theta \hat{\theta}) \left(ik - \frac{1}{r} \right) \right\} \quad \text{A.46}$$

Since

$$\vec{E} = E_r \hat{r} + E_\theta \hat{\theta} \quad \text{A.47}$$

we obtain

$$E_{\theta} = \frac{1}{4\pi\epsilon_0 n^2} e^{ikr} \left[\left(\frac{-k^2}{r} - \frac{ik}{r^2} + \frac{1}{r^3} \right) p \sin \theta \right] \quad \text{A.48}$$

$$E_r = \frac{1}{4\pi\epsilon_0 n^2} e^{ikr} \left[\left(\frac{-2ik}{r^2} + \frac{2}{r^3} \right) p \cos \theta \right] \quad \text{A.49}$$

Using the long wavelength approximation $kr \ll 1$,

we arrive at

$$E_{\theta} = \frac{1}{n^2} \left[\frac{1}{r^3} p \sin \theta \right] \quad \text{A.50}$$

$$E_r = \frac{2}{n^2} \left[\frac{1}{r^3} p \cos \theta \right] \quad \text{A.51}$$

$$\vec{E} = \frac{1}{n^2} \left[2 \cos \theta \hat{r} + \sin \theta \hat{\theta} \right] \frac{1}{r^3} p \quad \text{A.52}$$

This is the electric field of the oscillating dipole.

In the case, where the acceptor molecule is in the zone of the donor, the effective electric field felt by the acceptor is [153]

$$\vec{E}_{A,D} = \vec{p}_A \cdot \vec{E}_D \quad \text{A.53}$$

The donor electric field is given already in Eqn. A.52.

Inserting Eqn. A.52 into Eqn. A.53, the term

$$2 \cos \theta \hat{r} \cdot \vec{p}_A + \sin \theta \hat{\theta} \cdot \vec{p}_A \quad \text{A.54}$$

is called the orientation factor, κ , of the interacting dipole moments of the donor and the acceptor. For a random orientation of the dipole moments of the donor and acceptor, κ^2 gives 2/3.

The expression for determining the energy absorption of the effective electric field $\vec{E}_{A,D}$ is given by

$$w^A = \alpha |E_{A,D}|^2 \quad \text{A.55}$$

Here, α is the constant related to the acceptor optical properties [154].

Finally, it is clearly seen that, the $\frac{1}{r^6}$ dependence of the energy transfer actually results from Eqn. A.55.

Rearranging the terms and taking into account the spectral bandwidths of the emission spectra of the donor and the absorption spectra of the acceptor, together with the quantum yield of the donor, we also finally arrive at Eqn. 3.2.2, which is given previously as

$$R_0 = 0.211(\kappa^2 n^{-4} Q_D J(\lambda))^{1/6} \quad \text{A.56}$$